



Skolkovo Institute of Science and Technology

Skolkovo Institute of Science and Technology

THE NUMERICAL MODELING OF NANOPHOTONIC STRUCTURES BY
MEANS OF WELL-CONDITIONED VOLUME INTEGRAL EQUATION
METHODS

Doctoral Thesis

by

ALEXANDRA ALEKSANDROVNA TAMBOVA

DOCTORAL PROGRAM IN COMPUTATIONAL DATA-SCIENCE AND ENGINEERING

Supervisor:

Prof. Maxim Fedorov

Co-supervisor:

Athanasios G. Polimeridis

Moscow - 2019

©Alexandra Tambova 2019

Abstract

Volume integral equation (VIE) methods seem to be promising approaches for simulating 3-D nanophotonic devices, since they are dispersion free by construction, can efficiently handle inhomogeneous materials, restrict the computational domain solely to the volume of the scatterer, and in the case of finite scatterers, do not necessitate any boundary conditions while truncating the computational domain. However, many devices of interest, such as optical couplers, ring resonators, etc., include input and output channels that cannot be terminated without generating reflections. Generating absorbers for these channels is a new problem for VIE methods, as the methods were initially developed for exterior scattering problems.

In this thesis, we describe the implementation and performance of adiabatic absorbing layers in a current-based volume integral equation (VIE) method for simulating infinite or semi-infinite nanophotonic channels within a finite computational domain. In order to minimize reflections from the channel's truncations at the borders of the domain, we place artificial absorbing regions at the truncation sites, in which the conductivity is increased gradually. In the continuous setting, such *adiabatic absorbers* have been shown to produce reflections that diminish at a rate related to the smoothness of the absorption profile function. The VIE formulation we employ relies on uniform discretizations of the geometry over which the unknown

currents and material properties are represented by piecewise constant functions. Since nanophotonic devices are man-made structures, they consist of homogeneous or piecewise homogeneous regions. Thereby the only regions where continuously varying material properties may take place are the artificial adiabatic absorbers. We demonstrate via numerical experiments, that the asymptotic estimates of the reflections from the continuous absorption profiles hold for the reflections from discontinuous ones. Hence, the piecewise constant functions, firstly, fairly represent the materials inside the real structures of interest, and secondly, do not bother the wave attenuation in artificial absorbers. Such a discretization enables the acceleration of the method via the fast Fourier transform (FFT), resulting in $\mathcal{O}(N \log N)$ complexity of the iterative solution of the linear system. Furthermore, the introduction of varying absorption can be performed in a straightforward manner without compromising this speedup. Moreover, the employed formulation enables reduction from the original volume-volume integrals, arising in the calculation of Galerkin inner products, associated with the integral operators, to the series of surface-surface integrals over the faces of mesh elements. We present the novel numerical method for evaluation of singular integrals over quadrilateral patches, which take place when the elements coincide or share a face or a vertex.

We demonstrate the performance of the proposed algorithms via numerical experiments on different photonic devices: a rectangular waveguide channel, a waveguide with periodic width corrugations (a Bragg grating), and a Y-brunch splitter. The numerical results show that, in spite of the crude discrete approximation to the smooth absorption profiles, our approach recovers the asymptotic estimates for the reflection behavior of adiabatic absorbers with a continuous profile. Overall, we observe that the proposed adiabatic absorber performs extremely well in the VIE setting when truncating uniform guiding structures, and show the difficulties arising when truncat-

ing periodic ones. In addition, we presented some results pertaining to the iterative solution of the VIE's discrete system, and show that using a circulant preconditioner is extremely effective and renders the number of iterations small and independent of the structure's length. We thereby show that the FFT-accelerated VIE method presented herein is an effective and fast tool for nanophotonics simulations, although there is still great room for improvement and optimization.

List of publications

- A. Tambova, G. Guryev, and A. G. Polimeridis, "On the Fully Numerical Evaluation of Singular Integrals Over Coincident Quadrilateral Patches," *2017 11th European Conference on Antennas and Propagation (EuCap)*, Paris, 2017. DOI: 10.23919/EuCAP.2017.7928154
- Alexandra Tambova, Mikhail Litsarev, Georgy Guryev, and Athanasios G. Polimeridis, "On the Generalization of DIRECTFN for Singular Integrals Over Quadrilateral Patches", *IEEE Transaction on Antennas and Propagation*, Volume: 66, Issue: 1, Jan. 2018, pp. 304-314. DOI: 10.1109/TAP.2017.2776341
- A. Tambova, S. P. Groth, J. K. White and A. G. Polimeridis, "Adiabatic Absorbers in Photonics Simulations with the Volume Integral Equation Method," *Journal of Lightwave Technology*, vol. 36, no. 17, pp. 3765-3777, 1 Sept.1, 2018. DOI: 10.1109/JLT.2018.2842054
- Samuel P. Groth, Athanasios G. Polimeridis, Alexandra Tambova, and Jacob K. White, "Circulant preconditioning in the volume integral equation method for silicon photonics", *Journal of the Optical Society of America A*, vol. 36, No. 6, 2019. DOI: 10.1364/JOSAA.36.001079

Acknowledgements

I would like to take this chance to thank all the people who made this thesis possible.

First of all, I wish to express my great appreciation to my co-supervisor, Athanasios G. Polimeridis. He gave me an opportunity to join Skoltech, provided an unreserved encouragement and pertinent guidance throughout my PhD program, and most importantly, did a lot to bring me closer to an independent researcher.

I spent a term as a visiting student at Massachusetts Institute of Technology and would like to express a great thank to my supervisor there, Prof. Jacob K. White, whose passion in research encourages everyone working with him. He generously shared his ideas through our discussions, which helped to shape the final direction of my research.

I am very deeply thankful to Samuel P. Groth for sharing his knowledge and experience, as well as his extraordinary help and patience. This led to fruitful collaboration, which made this thesis possible to be created.

I would also like to thank my Individual Doctoral Committee members, Ivan Oseledets and Aleksander Shapeev, and my supervisor Prof. Maxim Fedorov, for their extremely helpful comments and substantive suggestions.

My heartfelt thanks to present and past members of the Computational Prototyping Group: Efim Boeru, Georgy Guryev, Ilias Giannakopoulos, and Mikhail Litsarev.

Because of these wonderful colleagues, I really enjoyed these years at SkolTech. Special thanks to Ioannis Georgakis, whose help and support was constantly with me over our whole journey as PhD students.

Finally, I wish to express my very profound gratitude to my family and friends, who have been an endless source of strength and inspiration during the last years. My heartfelt thanks to Alexandra Tolstikova, Ksenia Shults, Olesia Minakovskaia, Diana Mingazova and Denis Davydov for their moral support and making me believe in myself.

Last, but not least, actually the most important, my great thanks to my parents for bringing me to this world, bringing me up, and educating me, with all their love. I am proud of you two, and I have done and will do my best to let you be proud of me.

Contents

1	Introduction	25
1.1	Silicon Photonics Applications	25
1.2	Terminating Waveguide Channels with Integral Equation Methods	26
1.3	Volume Integral Equation Method	31
1.4	Novelty	35
1.5	Thesis Outline	35
2	Numerical Simulation Method	38
2.1	Problem Statement	39
2.2	JM-VIE formulation	40
2.3	Galerkin Discretization	43
2.4	Reduction to surface-surface integrals	47
2.5	Evaluation of Singular Integrals	51
2.5.1	Rectangular Parametric Space	52
2.5.2	Coincident Integration	54
2.5.3	Edge Adjacent Integration	61
2.5.4	Vertex Adjacent Integration	71
2.5.5	Numerical tests	73

2.6	FFT-based solver	75
2.7	Preconditioning	78
2.8	Fields Computation	82
2.9	Summary of the Numerical Method	82
2.10	Numerical Results and Error Analysis	85
3	Absorbers and Reflections	91
3.1	Adiabatic absorbers in the EM setting	92
3.2	Round-trip reflection and transition reflection	94
4	Numerical Results of Absorbers	100
4.1	Dielectric strip waveguide	103
4.1.1	Field Decay Rate	108
4.1.2	Transition reflection length dependency	110
4.1.3	Electric and magnetic conductivities	112
4.1.4	Comparison with COMSOL Multiphysics [®]	116
4.2	Bragg grating	119
4.3	Y-branch splitter	127
4.4	Signal-to-Noise ratio	131
5	Discussion	134
6	Conclusions	137
A	Numerical Tests of DIRECTFN-quad	142
A.1	Sensitivity to the quality factor of the elements	142
A.2	Weakly and strongly singular integrals with vector basis functions	144
A.3	Singular integrals over quadratic curvilinear quadrilaterals	146

List of Figures

1-1	A 2D-slice comparison of use of absorbing layers/PMLs in differential equation methods and integral equation methods.	30
2-1	Geometry of parametric transformation of the original quadrilateral to a square.	52
2-2	Orientation of the quadrilateral elements in space: (a) edge adjacent case; (b) vertex adjacent case.	54
2-3	Geometry of the parametric transformations for the coincident case: (a) $\{u', v'\} \rightarrow \{\rho, \theta\}$; (b) $\{t, v\} \rightarrow \{\Lambda, \Psi\}$	54
2-4	Geometry of the parametric space $\{u, \Psi\}$: (a) $0 \leq \Psi \leq \Psi_1$ and $\Psi_1 \leq \Psi \leq \Psi_2$; (b) $\Psi_2 \leq \Psi \leq \pi$	58
2-5	Edge adjacent integration: (a) polar coordinate transformation $\{u', v'\} \rightarrow \{\rho, \theta\}$; (b) the $\{u, \theta\}$ domain for the second shift of the integral, $\Theta_1 \leq \theta \leq \Theta_2$	61
2-6	Polar coordinate transformations employed in the edge adjacent integration: the domain for interchanging the integrals $\{u, \Psi\}$, for a fixed value of θ ($0 \leq \theta \leq \Theta_1$): (a) $u_1(\theta) = 1$ ($0 \leq \theta \leq \pi/4$); (b) $u_1(\theta) < 1$ ($\pi/4 < \theta \leq \pi/2$).	66

2-7	Polar coordinate transformations employed in the edge adjacent integration: (a) the $\{u, \theta\}$ domain for the third shift of the integral, $\Theta_2 \leq \theta \leq \pi$; (b) the domain for interchanging the integrals $\{u, \Psi\}$, for a fixed value of θ and $u_2(\theta) = -1$ ($\pi/2 \leq \theta \leq 3\pi/4$); and (c) the domain for interchanging the integrals $\{u, \Psi\}$, for a fixed value of θ and $u_2(\theta) > -1$ ($3\pi/4 < \theta \leq \pi$).	69
2-8	Polar coordinate transformations employed in vertex adjacent integration: $\{u, v\} \rightarrow \{\rho_p, \theta_p\}$, $\{u', v'\} \rightarrow \{\rho_q, \theta_q\}$	71
2-9	Relative error in computing the singular integrals (2.123) as a function of the order of the 1-D Gaussian quadrature rules, DIRECTFN-quad comparison with DIRECTFN-tri.	75
2-10	Relative CPU times of the proposed scheme with respect to the original DIRECTFN as a function of the order of the 1-D Gaussian quadrature rules.	76
2-11	Convergence history of GMRES (tol = 10^{-8}) without restarts for a straight waveguide of lengths $10\lambda_i$ and $30\lambda_i$. Observe how, with no preconditioner, the iteration count grows with the waveguide length. The circulant preconditioner, on the other hand, leads to an iteration count independent of the waveguide length.	79
2-12	(a) A Mie sphere illuminated by a plane wave; (b) a discretized Mie sphere.	86
2-13	The components of interior electric field inside the Mie sphere, $\sigma_E = 0$ S/m.	87
2-14	The components of interior electric field inside the Mie sphere, $\sigma_E = 100$ S/m.	88

2-15	The components of interior electric field inside the Mie sphere, $\sigma_E = 1000 \text{ S/m}$	89
2-16	Relative error of interior electric fields observed along the x-axis with respect to resolution.	90
3-1	The waveguide with the absorber attached. The waveguide begins at the origin and extends to $x = X$ before the absorbing region begins, and this region terminates at $x = X + L$	93
3-2	Types of the reflections produced by the absorber.	95
4-1	Problem setup for a Gaussian beam source within a silicon strip waveguide with one absorber attached. Only one absorber is necessary for this problem since the source has directionality and we anticipate no reflections propagating in the $-x$ -direction. The cladding medium is silicon dioxide.	103
4-2	The absolute value of y-component of the electric field along the \hat{x} - axis.	104
4-3	The absolute value of y-component of the electric field along the \hat{y} - axis.	105
4-4	The absolute value of y-component of the electric field along the \hat{z} - axis.	106
4-5	The complex magnitude of the electric field inside a waveguide and absorber. The dashed line indicates the position of the waveguide-absorber interface.	107
4-6	The complex magnitude of the electric field along the \hat{x} -axis inside the absorber with uniform conductivity.	108

4-7	The rate of field exponential decay along the propagation direction versus electric conductivity.	109
4-8	Reflection coefficient versus absorber length L for first three monomial absorption profiles when $R_{rt} = 10^{-25}$. The lines labeled e correspond to the case where only the electric field is solved for. The lines labeled e&m correspond to the case where both the electric and magnetic fields are solved for, with the impedance matched. Note that this impedance matching reduces the reflection coefficient by approximately a factor of 100. We observe that each of the first three monomials achieves the asymptotic convergence rate of $\mathcal{O}(L^{-2(d+1)})$	111
4-9	Reflection coefficient versus absorber length L for cubic absorption profiles when $R_{rt} = 10^{-25}$. The blue squares correspond to the case where only the electric field is solved for. The red circles correspond to the case where both the electric and magnetic fields are solved for, with the impedance matched. Observe that the convergence is faster than the predicted asymptotic rate, implying the asymptotic range is not achieved for these absorber lengths. In fact, for cubic and higher order profiles, the asymptotic range is not achieved for any of the practical examples considered in this thesis.	112
4-10	Reflection coefficient versus absorber length L for first three monomial absorption profiles for two different round-trip reflections: $R_{rt} = 10^{-25}$ (blue crosses) and $R_{rt} = 10^{-10}$ (red diamonds). An order of magnitude reduction in the reflection coefficient is achieved by decreasing the imposed round-trip reflection in this way.	115

4-11	Reflection coefficient versus absorber length L for first three monomial profiles for two different round-trip reflections: $R_{rt} = 10^{-10}$ (blue crosses) and $R_{rt} = C_{opt}L^{-2(d+1)}$ (red diamonds). The second case is equivalent to balancing the round-trip reflection with the transition reflection. Observe the improvement achieved; this gain diminishes as the polynomial degree increases.	116
4-12	TE (first) mode profile of a $500\text{ nm} \times 220\text{ nm}$ strip waveguide at 1550 nm wavelength obtained with COMSOL. The three field components in the x, y, z directions are shown.	117
4-13	JVIE solution, obtained for $500\text{ nm} \times 220\text{ nm} \times 22\text{ }\mu\text{m}$ waveguide with quadratic absorber of length $4.4\text{ }\mu\text{m}$ at 1500 nm wavelength. The components of electric field in yz -plane, obtained at $x = 15.84\text{ }\mu\text{m}$ (0.72 of waveguide length) from the left end of the waveguide, are shown. Observe the qualitative agreement with the TE-mode obtained with COMSOL.	118
4-14	The relative difference between interpolated COMSOL and JVIE solutions. The fields are scaled by their maximum values.	119
4-15	x -component of the electric field along the z -axis: (a) absolute difference between COMSOL and JVIE solutions; (b) COMSOL and JVIE solutions.	120
4-16	Top view of the layout for Bragg grating with period Λ , width W , corrugation depth ΔW , and length $N \times \Lambda$, where N is an integer. Since the waves propagate in both directions due to reflections from the corrugations, absorbers are required on both ends for simulations. To generate the 3D structure, this layout is extruded a distance D in the z -direction (out of the page).	121

4-17	Transmission through the Bragg grating of length 100 periods. The Bragg wavelength is 1545 nm and the band gap is approximately 20 nm wide.	122
4-18	Reflection coefficient versus absorber length L for monomial profiles with the round-trip reflection set to $R_{rt} = 10^{-10}$. The Bragg grating is excited at 1520 nm free-space wavelength. The asymptotic convergence rates are eventually achieved for the first three monomials. . . .	123
4-19	Reflection coefficient versus absorber length L for monomial profiles with the round-trip reflection set to $R_{rt} = 10^{-10}$. The Bragg grating is excited at 1538 nm free-space wavelength.	125
4-20	The reflection coefficient versus free-space wavelength for an absorber inside the “infinite” Bragg grating. The adiabatic absorber has a quadratic profile and length 50 periods ($36\lambda_i/15\lambda_e$). Comparing to Fig. 4-17, observe that the reflection from the absorber is large in and close to the band gap, with the peaks corresponding to the band gap edges where the group velocity changes sign.	127
4-21	Top view of the layout of a Y-branch splitter with adiabatic absorbers appended to the waveguide-branch ends. This structure is excited by a Gaussian beam injected just to the right of the left absorber. A right-propagating mode is established, is split in half at the junction, and each half propagates along its respective curved branch.	128
4-22	$ \mathbf{E} ^2$ for a silicon Y-branch splitter with SiO_2 cladding at 1550 nm. . .	129
4-23	Relative difference in solution ($ \mathbf{E} ^2$) obtained using absorbers of length 5λ and 20λ . This difference can be attributed to the reflection from the 5λ -length absorbers.	130
4-24	SNR dependence on σ_0 for a given profile and fixed absorber length. .	132

4-25	SNR dependence on resolution.	133
A-1	Relative error in computing the weakly singular integrals (2.123) over coincident elongated quadrilaterals as a function of the order of the 1-D Gaussian quadrature.	143
A-2	Relative error in computing the weakly singular integrals (A.2) over coincident squares as a function of the order of the 1-D Gaussian quadrature.	145
A-3	Relative error in computing the strongly singular integrals (A.3) over edge-adjacent squares as a function of the order of the 1-D Gaussian quadrature.	146
A-4	Relative error in computing the strongly singular integrals (A.3) over vertex-adjacent squares as a function of the order of the 1-D Gaussian quadrature.	147
A-5	Relative error in computing the weakly and strongly singular integrals over quadratic curvilinear elements as a function of the order of the 1-D Gaussian quadrature	148

List of Tables

2.1	Performance of block-circulant preconditioner for the strip waveguide with $L = 30\lambda_i$, terminated by the absorbers with different lengths. . .	80
2.2	Performance of block-circulant preconditioner for strip waveguide with different lengths, terminated by the absorber of the length $L_{abs} = 10\lambda_i$.	80
4.1	The standing wave ratio (SWR) and field reflection versus the conductivity distribution of the absorber, whose length is $\sim 10\lambda_i$	107
4.2	Absorber length (in units of number of exterior wavelengths) required to obtain $R = 10^{-8}$. We choose such a value for R since it is sufficiently small for practical purposes. Some of the values for $d = 0, 1$ have been extrapolated from Fig. 4-8 and Fig. 4-10.	113

List of Abbreviations

2D	two-dimensional
3D	three-dimensional
4D	four-dimensional
6D	six-dimensional
AIM	adaptive integral method
BTTB	block-Toeplitz with Toeplitz blocks
BCCB	block-circulant with circulant blocks
CG-FFT	conjugate gradient fast Fourier transform
CMT	coupled-mode theory
DB	flux densities-based formulation
DE	differential equation
EA	edge adjacent
EM	electromagnetic(s)
EH	field-based formulation

FFT	fast Fourier transform
FDTD	finite difference time domain
FE	finite elements
FG-FFT	fitting Green function fast Fourier transform
GMRES	generalized minimal residual method
IE	integral equation
IE-FFT	integral equation fast Fourier transform
J-VIE	current-based VIE with electric currents
JM-VIE	current-based VIE with electric and magnetic currents
MLFMA	multilevel fast multipole algorithm
MoM	Method of Moments
MVP	matrix-vector product
p-FFT	precorrected-FFT method
PML	perfectly matched layer
SNR	signal-to-noise ratio
SWR	standing wave ratio
SIE	surface integral equation
ST	self-term
TE	transverse electric

VA	vertex adjacent
VIE	volume integral equation
VSIE	volume-surface integral equation

List of Symbols

ω	angular frequency
j	imaginary unit
\mathbb{R}^3	3D Euclidian space
\mathbf{r}	point in 3D Euclidian space
Ω	the domain in \mathbb{R}^3 occupied by the scatterer
ϵ	electric permittivity
ϵ_0	free-space permittivity
ϵ_r	relative electric permittivity
ϵ'_r	real part of relative electric permittivity
ϵ''_r	imaginary part of relative electric permittivity
μ	magnetic permeability
μ_r	relative magnetic permeability
μ'_r	real part of relative magnetic permeability
μ''_r	imaginary part of relative magnetic permeability

μ_0	free-space permeability
c_e	$j\omega\epsilon_0$
c_m	$j\omega\mu_0$
\mathbf{e}	electric field
\mathbf{h}	magnetic field
$\mathbf{e}_{\text{inc}}(\mathbf{h}_{\text{inc}})$	incident electric (magnetic) field
$\mathbf{e}_{\text{sca}}(\mathbf{h}_{\text{sca}})$	scattered electric (magnetic) field
\mathbf{j}_{inc}	primary current source
\mathbf{j}	polarization (electric) current
\mathbf{m}	magnetization (magnetic) current
\mathcal{N}/\mathbf{N}	continious/discrete operator
$\mathcal{S}(f)$	volume vector potential of f
G	free-space scalar Green function
k_0	free-space wavenumber
\mathcal{I}	identity operator
\mathcal{M}	multiplication operator
\mathbf{p}_i^α	pieese-wise constant basis function associated with $\hat{\alpha}$ -direction ($\alpha = \{x, y, z\}$) and the support voxel i
$\omega_{e_i}^\alpha$	weight of the basis function \mathbf{p}_i^α in the expansion of the uncknown electric current

$\omega_{m_i}^\alpha$	weight of the basis function \mathbf{p}_i^α in the expansion of the unknown magnetic current
w_e	vector consisting of the unknown weights $w_{e_i}^\alpha$
w_m	vector consisting of the unknown weights $w_{m_i}^\alpha$
$\langle \cdot, \cdot \rangle$	standard L^2 inner product
$\delta_{\alpha\beta ij}$	generalized Kronecker delta
\mathcal{C}	(multilevel) circulant matrix
$\text{fftn}\{\cdot\}$	multidimensional Fast Fourier Transform
$\text{ifftn}\{\cdot\}$	multidimensional inverse Fast Fourier Transform
λ_i	the wavelength inside the material (interior wavelength)
L	absorber length
$\sigma_E(\sigma_M)$	electric (magnetic) conductivity
$s(u)$	absorption profile
u	coordinate scaled by the absorber length
d	index of power of the monomial absorption profile
Z_i	intrinsic impedance of the non-conductive waveguide
Z_{abs}	impedance of the conductive absorber region
n	complex refractive index of the medium
R_{rt}	round-trip reflection coefficient
c_r	amplitude of the reflected mode

M	coupling coefficient between the incident and reflected modes
β_i	propagation constant of the incident mode
β_r	propagation constant of the reflected mode
$\Delta\beta$	difference between propagation constants of the incident and reflected modes
R_t	transition reflection coefficient
v_g	group velocity
Λ	period of the periodic structure
λ_e	the free-space wavelength (exterior wavelength)
\mathcal{L}^2	function space of square integrable functions

Chapter 1

Introduction

1.1 Silicon Photonics Applications

Silicon photonics [1, 2, 3] is poised to be a disruptive technology in several fields, from high-speed data communications such as long-haul optical transmissions [4], short-reach communications in datacenters and supercomputers, and intra- and inter- chip connections [5, 6, 7], to healthcare [8] and environmental monitoring [9]. Moreover, silicon photonic devices can be made exploiting the current equipment and methods already available for electronic chips, which brings optical communications into the fabrication space of the semiconductor industry, enabling low-cost, high-volume assembly. Another potential advantage is the possibility to create integrated optoelectronic devices [10, 2].

Among the other photonic structures, silicon waveguides are of particular interest. Being a part of a great diversity of more complex photonic devices, and also acting as a self-sufficient optical functions, waveguides can be used for communications [2], interconnect [7], biosensors [11, 12], as well as supporting the exotic nonlinear phe-

nomena such as soliton propagation [13, 14, 15]. Moreover, by introducing a periodic modulation into an optical waveguide channel, one can obtain plenty of additional effects useful for photonic applications: periodicity creates the band gaps that can be used for light confinement [16], and decreasing group velocity of light near the band edge can increase the light-matter interaction for non-linear devices [17, 18, 19]. Furthermore, controlling the group velocity can be used for tunable time delays [20] and dispersion compensation [21, 22, 23, 24, 25].

1.2 Terminating Waveguide Channels with Integral Equation Methods

The emerging field of computational science is playing a crucial role in designing new generations of silicon photonic systems and devices [26, 27]. Fast and reliable electromagnetics (EM) solvers facilitate studying the light behavior and light-matter interaction and are used to cheaply prototype new components such as ring resonators [12] and Mach-Zehnder interferometers, and to test their resilience to manufacturing defects such as surface wall roughness [28]. However, a truncation difficulty arises with modeling of very long waveguide channels, which are, as mentioned above, very common in photonics. In this thesis, we consider the application of volume integral equation method (VIE) [29, 30] to study devices incorporating guiding structures with uniform or periodic cross-section. In order to eliminate reflections fuelled by the unavoidable truncation of the computational domain, we append the region with gradually increasing absorption at the truncation places.

The most popular EM solvers in silicon photonics are, at present, those based on approximating Maxwell's equations directly via finite element [31] or finite differ-

ence [32] methods. We shall refer to such approaches as differential equation (DE) methods since they discretize the differential operator directly. One of the most prominent advantages of DE methods is their high versatility and ease of adaptation to couple the Maxwell equations with other differential equations so that a multiphysics problem can be solved [33]. Moreover, the DE-based methods are very generic and can be applied to almost any geometry. Although there are subtleties to be concerned about, The DE methods can be implemented in a straightforward manner resulting in a shorter development cycle, which makes them propitious for commercialization. For example, the finite difference time domain (FDTD) method is used in Lumerical [34] and FullWAVETM [35], the finite elements (FE) method is exploited in COMSOL Multiphysics[®], etc. However, there are also some disadvantages.

When applied to a scattering problem on a finite obstacle, a DE method would have to truncate the infinite domain at some distance from the obstacle. First, special care should be taken to avoid numerical reflections from the boundaries. Indeed, the boundary of a finite computational domain should reproduce as accurately as possible a homogeneous nonlossy infinite medium, i.e. all the non-physical reflections must be minimized. It is conventionally achieved by introducing a perfectly matched layer (PML) [36] or absorbing boundary conditions [32, 31]. Second, the whole computational domain should be discretized. In cases when the high-resolution is required, e.g., to capture the sub-wavelength phenomena, this would inevitably lead to the need for large computational resources and, consequently, in many cases to an unfeasible computation. Another problem is the numerical dispersion, which may potentially lead to large phase errors when considering the structures spanning many wavelengths.

An alternative approach is to reformulate Maxwell's equations in an integral form

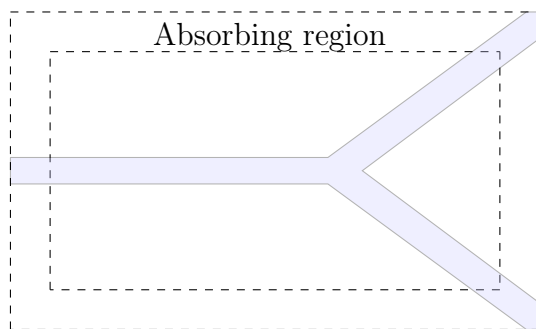
to solve for the EM field over the structure of interest. First of all, integral equations (IE) satisfy the radiation condition at infinity by construction, hence a computation over the infinite scattering domain can be restricted to one solely over the surface or volume of the finite obstacle, which promises a more efficient computation than the DE-based methods. Further, IE methods have the distinct advantage that they are dispersion free owing to the fact that the Green function is an exact propagator of the field [37]. This dispersion-free property is especially desirable in the nanophotonics setting where the structures of interest may span hundreds or thousands of wavelengths.

Unfortunately, the subsequent discretization of IEs using the method of moments (MoM) algorithm [38] gives rise to a dense matrix system in contrast to the sparse matrices of DE methods. The solution of this matrix system by a Krylov-space iterative solver requires $\mathcal{O}(N^2)$ memory and $\mathcal{O}(pN^2)$ computation time, where N is the number of unknowns and p is the number of iterations to achieve the desired accuracy. However, fast solvers reaching $\mathcal{O}(pN \log N)$ complexity for IE methods, such as multilevel fast multiple algorithm (MLFMA) [39, 40, 41, 42, 43, 44], the conjugate gradient fast Fourier transform (CG-FFT) method [45, 46, 47], the integral equation FFT (IE-FFT) method [48, 49, 50], the adaptive integral method (AIM) [51, 52, 53], the precorrected-FFT (p-FFT) method [54, 55, 56, 57], and the fitting Green function FFT (FG-FFT) method [58, 59, 60] have been developed, thus allowing them to be competitive with DE methods.

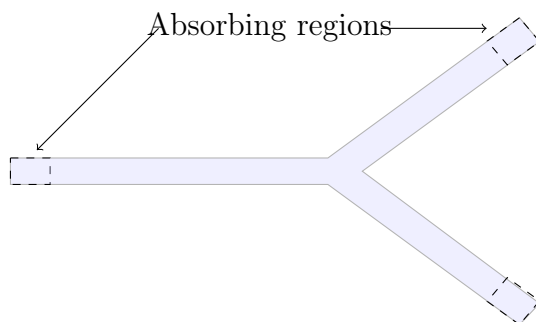
Traditionally, IE approaches found their applications in the exterior scattering problem, where a wave impinges on a finite obstacle. When applied to unbounded obstacles such as waveguides, IEs can be applied with a modified Green's function constructed especially to take into account the unbounded nature of the particular geometry. However, this is an involved approach and so far has been applied suc-

cessfully only for 2D waveguide-type problems, e.g., in [61, 62, 63]. A more straightforward approach is to introduce absorbing regions, as is done in DE methods. One advantage of an IE approach over DE is that the deployment of absorbing regions can be more flexible and, further, they are required over a much smaller region. Consider Fig. 1-1 in which we compare the use of absorbing regions in DE and IE methods for a simple waveguide splitter taken from [64]. In DE methods, one must artificially truncate the entire computational domain, whereas in IE methods it is only necessary to truncate the portions of the obstacle which extend away in an unbounded fashion; here it is the waveguide branches or ports. The remainder of the domain is truncated analytically via the IE formulation, leading to a considerably reduced computation domain. Further note that the diagram in Fig. 1-1 is of a 2D slice. In DE methods there must also be absorbing layers above and below the waveguide whereas the IE method truncates in these directions analytically by construction. We further note that since in the IE setting the absorbing regions geometrically continue the waveguides, the evanescent waves propagating outside the waveguides do not impinge on an absorbing region, as is the case for domain truncation in DE methods. Therefore, we can side-step the additional modifications that are needed to account for the reflections of evanescent waves [65, 66, 67].

For domain truncation, PMLs have previously been used in IE settings [68], however, it is known that for certain scenarios, PMLs fail, even in the limit of high resolution [64]. In particular, when the material properties are not analytic functions in the direction perpendicular to the PML boundary. We consider one such example (a Bragg grating) in detail in Section 4.2. It is shown in [64] (albeit there in the context of finite-difference methods) that a more robust approach to domain truncation is to use adiabatic absorbers rather than PMLs. Adiabatic absorbers are regions in which the conductivity (absorption) of the medium is gradually increased



(a) Differential equation methods



(b) Integral equation methods

Figure 1-1: A 2D-slice comparison of use of absorbing layers/PMLs in differential equation methods and integral equation methods.

to minimize reflections. The key feature of PMLs is that they match the impedance between the waveguide and the absorbing region, and this feature can be retained in adiabatic absorbers as we demonstrate in Section 3.1 and Section 4.1.3. Indeed, it was shown in [64] that such an impedance matching absorbing region performs almost as well as a PML in situations when PMLs do not fail, and outperforms PMLs in the remaining scenarios.

In [69], adiabatic absorbers were implemented in the surface integral equation (SIE) setting and shown to be effective there. In this thesis, we introduce the first implementation of adiabatic absorbers in the *volume* integral equation method (VIE).

1.3 Volume Integral Equation Method

The majority of IE-based methods used in nanophotonics applications can be split into two groups. The first ones are the surface integral equation (SIE) methods [70, 71, 72, 73, 43, 44, 74], which reduce the computation of EM scattering problem to the surface boundaries of materials, therefore work best for homogeneous or piecewise-homogeneous medium. In these cases, the surface-only discretization scheme turns a 3D-geometry into a 2D-surface, which significantly reduces the computational costs. For inhomogeneous medium, the efficiency of the SIE decreases as the number of the subdomains increases, since boundary conditions must be enforced on the surface of each homogeneous subdomain, and the Green function in different homogeneous media must be used in the formulation. Hence, in the case of inhomogeneous scatterers, the volume integral equation (VIE) methods [75, 30, 76, 47, 52, 53, 49, 50, 56, 57, 60] are a more popular choice. They transform Maxwell's equations in an integral form to solve for the electromagnetic field on a reduced volume and require only the Green function of the background medium, thus can be applied for complex inhomogeneous materials more easily than the SIE methods. For the composite objects containing both dielectric and conductive regions, the hybrid volume-surface integral equation (VSIE) formulation is sometimes also used [77, 78, 79].

Conventionally, the combination of fields-based (EH) or flux densities-based (DB) VIE formulations with a set of div-conforming basis functions were used [80, 81, 82]. However, it was shown in [83, 84], that due to improper incorporation of finite energy conditions in the above mentioned numerical schemes, the uniqueness and thereby the stability of numerical approximation may be lost. Moreover, even when the finite-energy conditions are imposed via the testing functions and employed bilinear form or inner product, these schemes create a gap between the intended solution

space and the actual solution space [83]. In addition, the DB formulation requires the inverse of the permittivity and permeability dyadics, hence it breaks down when the material contrast approaches zero. In contrast, the EH formulation leads to an unstable system when the material contrast goes to infinity [76]. The authors of [83, 84] proposed an alternative approach of using Galerkin VIE formulation based on equivalent volumetric current densities. The convergence properties of such current-based VIE formulations including the cases of the scattering from highly inhomogeneous isotropic, anisotropic and bi-anisotropic materials were further demonstrated in [85, 76]. Another possible choice is the potential VIE formulation [86, 87], which allows the use of fully continuous basis functions even for highly inhomogeneous media, since the unknown scalar and vector electric potentials are continuous across the material interfaces. This discretization with fully continuous basis functions results in a better-conditioned system matrix compared to those of other formulations with the fully or partially discontinuous basis function [88, 89]. However, it was shown in [90] that using either of two conventional testing schemes, namely, Galerkin and collocation methods, optimal convergence may not be achieved, and moreover, the spurious solutions may arise, especially for objects with negative permittivities and sharp corners. This is because the testing functions do not span the proper function space, that is, the dual space of the range space of the operator. Therefore, further studies are required to find the proper set of testing functions.

In this thesis, we use the modified current-based VIE formulation proposed in [29], which leads to the integral operators having the form *identity plus diagonal multiplier times compact*, which are the *second kind* integral operators, well behaved in terms of accuracy and convergence. We exploit uniform space discretization and approximate the unknown currents as well as the material properties, with piecewise constant functions. It should be noted that most of nanophotonic devices consist of

homogeneous or piecewise homogeneous regions since they are man-made structures. Hence, in the context of this thesis, the only regions where continuously varying material properties may take place are the artificial adiabatic absorbers, which we introduce to minimize the spurious reflections from the domain boundaries. However, we will demonstrate via numerical experiments, that the asymptotic estimates of the reflections from the continuous absorption profiles hold for the reflections from discontinuous ones. We can conclude, that the piecewise constant functions, firstly, fairly represent the materials inside the real structures of interest, and secondly, do not bother the wave attenuation in artificial absorbers.

Following the Galerkin method of moments, the approximation is then tested with the same basis functions. Besides the obvious ease of implementation, using the square-integrable functions, which piecewise constant functions belong to, guarantee the convergence of the solution in norm [83, 84]. Moreover, the employed uniform discretization makes the governing integral kernels translationally invariant, hence the resulting system matrix has the block-Toeplitz structure and the associated matrix-vector products can be accelerated with the help of fast Fourier transform (FFT) [91, 46, 92, 47, 93]. Furthermore, the introduction of varying absorption can be performed in a straightforward manner without compromising this speedup.

In addition, recently developed method [94] allows reducing the 6D volume-volume integrals, arising in the evaluation of Galerkin inner products, to the series of surface-surface integrals over the faces of support elements. In most of the cases, these integrals can be easily evaluated by readily available standard quadratures. However, the singularity arises in the integral kernels, when the source and observation points coincide, namely, when the faces of the support elements coincide or share a common edge or a common vertex. To tackle this problem, we have developed a novel fully numerical method of evaluating the 4D surface-surface singular integrals

over quadrilateral patches.

Unlike standard singularity subtraction [95, 96, 97, 98, 99] and singularity cancellation [100, 101, 102, 103, 104] methods, which are focused on the regularization of the inner 2D integrals of the original 4D Galerkin inner products, the proposed method consider the complete 4D integrals. As it was demonstrated recently, such an approach has certain advantages, especially in the case of strongly singular kernels or when high accuracy is needed [105, 106, 107, 108, 109, 110, 111, 112]. Exploiting the series of coordinate transformations together with the integration re-orderings, the algorithm yields the sufficiently smooth integrals that can be easily computed via simple Gaussian integration.

Arguably, the vast majority of the numerical methods mentioned above were developed for evaluating singular integrals over triangles, mainly due to the profound impact of the celebrated paper by Rao, Wilton, and Glisson [113] on the computational electromagnetics community, and the flexibility the triangular tessellations offer in modeling arbitrary geometries. However, modern computer-aided design software enables the analysis of complex geometries in terms of flat or curvilinear quadrilateral patches, which can describe just as accurately the geometry with far fewer degrees of freedom [114, 115, 116, 117, 118]. To the best of our knowledge, there are only a handful of papers in the literature dedicated to the evaluation of singular integrals over flat and curvilinear quadrilateral patches [117, 119, 99, 120, 121, 122], and it is quite clear that they haven't reached the performance levels of those for triangular patches.

The method presented herein is an extension of original DIRECTFN method [123], devoted to triangular patches. As we demonstrate further, the proposed scheme requires a series of complicated algebraic manipulations, therefore this extension from triangular to quadrilateral domains is by no means trivial. It's worth mentioning that

there is always a less sophisticated approach to handling these integrals by splitting the quadrilateral patches into triangular ones and applying the original DIRECTFN to their combinations. However, the computation of several integrals instead of one is likely to require more computation time for the same accuracy.

1.4 Novelty

The novel contributions of this thesis can be summarized as follows:

- The concept of *adiabatic absorbers* is applied in the volume integral equation setting. Specifically, we employ a current-based VIE formulation that allows these absorbers to be introduced in a simple and straightforward manner which does not affect the acceleration of the method via Fast Fourier Transform (FFT), thereby enabling rapid nanophotonics simulations.
- The new fully numerical method for evaluation of the singular integrals over quadrilateral elements was developed. These integrals arise in the calculation of Galerkin inner products, after the reduction of original volume-volume integrals to surface-surface ones. Besides being applied to planar square elements, which are the case in this thesis, the proposed method can be applied without modification to the planar and bilinear quadrilaterals of arbitrary shape, as well as for curvilinear elements.

1.5 Thesis Outline

This thesis is organized as follows. In Chapter 2 we establish the general scattering problem to solve, without the specification of any particular nanophotonic device.

Next, we introduce a current-based volume integral equation formulation (JM-VIE) and define the discretization of the resulting VIE system. Further, we briefly describe the reduction of the dimensionality of volume-volume integrals, arising in the evaluation of Galerkin inner products associated with the integral operators, and present the novel fully numerical method of evaluation of singular integrals over quadrilateral patches. Moreover, we provide numerical examples, demonstrating the effectiveness and accuracy of the developed algorithms. Finally, we briefly explain how the iterative solution is accelerated with FFT, and propose the preconditioning method. In addition, we provide some additional information regarding the memory requirements, iteration count, operator assembly and computational time. At the end of the chapter, we summarize all the stages of the proposed algorithm and its numerical implementation. Finally, we perform the simulation of scattering from a homogeneous sphere and compare the results with analytical solutions, obtained with the Mie series.

Chapter 3 provides details of the adiabatic absorbers and contains the evaluation of the reflection coefficients.

In Chapter 4 we examine the performance of adiabatic absorbers in three examples: a straight dielectric strip waveguide, a Bragg grating, and a Y-branch splitter. We observe that the adiabatic absorber performs extremely well in the VIE setting when terminating uniform structures, and show the difficulties arising when terminating periodic ones. Nonetheless, In both cases, the numerical experiments reproduce the asymptotic results from the literature. Moreover, in the case of strip waveguide, we managed to compare the solution with the guided TE mode, obtained for the same waveguide by using the COMSOL Multiphysics[®] software.

Next, in Chapter 5 we discuss the advantages and disadvantages of the proposed method and propose the possible alternatives and improvements that could help in

diminishing the drawbacks and can be considered as the directions of future research.

Finally, in Chapter 6 we provide the concluding remarks and discuss again possible directions of future work.

In Appendix A we present the additional numerical examples related to the applications of DIRECTFN-quad that go beyond its use in the described JM-VIE solver, including the usage of higher-order basis functions, and integration over non-squared elongated and curvilinear elements.

Chapter 2

Numerical Simulation Method

In this chapter, we describe all the stages of the numerical simulation method we use for electromagnetic analysis of nanophotonic structures. First of all, we establish the general scattering problem to solve, without the specification of any particular nanophotonic device. Next, we briefly introduce the volume integral equation formulation based on equivalent currents. We proceed with defining the discretization of the volume integral equations using the Galerkin method of moments, and provide the final linear system. Next, we describe the reduction from volume-volume integrals, arising in the evaluation of the Galerkin inner products, to the series of surface-surface integrals over the faces of voxels. We further provide the novel fully numerical method of fast and accurate evaluation of singular integrals over quadrilateral patches and demonstrate its effectiveness via numerical experiments. Finally, we briefly explain how the iterative solution is accelerated with FFT, and provide some additional information regarding the memory requirements, iteration count and preconditioning. At the end of the chapter, we summarize all the stages of the proposed method and its numerical implementation. To validate our solver, we consider

the scattering on the Mie sphere and compare the numerical solution obtained with the VIE method presented herein, to the analytical one.

2.1 Problem Statement

The general problem we aimed to solve in this thesis can be formulated as follows. Consider the inhomogeneous isotropic dielectric object in a homogeneous background, occupying domain Ω in 3D space \mathbb{R}^3 . The domain can be either bounded (e.g. a sphere) or unbounded (infinite or semi-infinite waveguide). The object is illuminated by a time-harmonic electromagnetic wave with angular frequency $\omega \in \mathbb{R}$, assuming the time-dependence is $e^{j\omega t}$ with $j = \sqrt{-1}$. The incident fields ($\mathbf{e}_{\text{inc}}, \mathbf{h}_{\text{inc}}$) satisfy Maxwell's equations in the absence of the dielectric object and are produced by primary sources. The object and the background are characterized by their electric and magnetic permittivity and permeability:

$$\begin{aligned} \epsilon &= \epsilon_0, \quad \mu = \mu_0 \quad \text{in } \mathbb{R}^3 \setminus \Omega, \\ \epsilon &= \epsilon_r(\mathbf{r})\epsilon_0, \quad \mu = \mu_r(\mathbf{r})\mu_0 \quad \text{in } \Omega. \end{aligned} \tag{2.1}$$

Here, the free-space permittivity ϵ_0 and permeability μ_0 are real positive values, whereas the relative permittivity $\epsilon_r(\mathbf{r})$ and permeability $\mu_r(\mathbf{r})$ read

$$\begin{aligned} \epsilon_r(\mathbf{r}) &= \epsilon'_r(\mathbf{r}) - j\epsilon''_r(\mathbf{r}), \\ \mu_r(\mathbf{r}) &= \mu'_r(\mathbf{r}) - j\mu''_r(\mathbf{r}), \end{aligned} \tag{2.2}$$

with $\epsilon'_r, \mu'_r \in (0, \infty)$ and $\epsilon''_r, \mu''_r \in [0, \infty)$. The non-zero imaginary part of the relative permittivity (permeability) implies that the material possesses an electric (magnetic) conductivity at that particular point.

To summarize, the scattering problem to solve can be formulated as follows: Given the incident fields $(\mathbf{e}_{\text{inc}}(\mathbf{r}), \mathbf{h}_{\text{inc}}(\mathbf{r}))$ (or, equivalently, the primary sources $\mathbf{j}_{\text{inc}}(\mathbf{r})$), and the dielectric object (2.1), characterized by its material properties (2.2), determine the total fields $(\mathbf{e}(\mathbf{r}), \mathbf{h}(\mathbf{r}))$.

2.2 JM-VIE formulation

In this section, we describe the volume integral equation formulation based on equivalent currents (JM-VIE) [29, 30] we use in this thesis.

Consider the scattering problem posed above. The total electric and magnetic fields (\mathbf{e}, \mathbf{h}) in the presence of isotropic inhomogeneous object are composed of incident and scattered fields

$$\begin{pmatrix} \mathbf{e} \\ \mathbf{h} \end{pmatrix} = \begin{pmatrix} \mathbf{e}_{\text{inc}} \\ \mathbf{h}_{\text{inc}} \end{pmatrix} + \begin{pmatrix} \mathbf{e}_{\text{sca}} \\ \mathbf{h}_{\text{sca}} \end{pmatrix}, \quad (2.3)$$

where the incident fields $(\mathbf{e}_{\text{inc}}, \mathbf{h}_{\text{inc}})$ are generated by primary sources in the absence of the scatterer. The scattered fields can be expressed in terms of equivalent polarization and magnetization currents (\mathbf{j}, \mathbf{m}) as

$$\begin{pmatrix} \mathbf{e}_{\text{sca}} \\ \mathbf{h}_{\text{sca}} \end{pmatrix} = \begin{pmatrix} \frac{1}{c_e}(\mathcal{N} - \mathcal{I}) & -\mathcal{K} \\ \mathcal{K} & \frac{1}{c_m}(\mathcal{N} - \mathcal{I}) \end{pmatrix} \begin{pmatrix} \mathbf{j} \\ \mathbf{m} \end{pmatrix}, \quad (2.4)$$

where $c_e := j\omega\epsilon_0$, $c_m := j\omega\mu_0$, and \mathcal{I} is the identity operator. The integro-differential

operators are defined as

$$\mathcal{K}f := \nabla \times \mathcal{S}(f), \quad (2.5)$$

$$\mathcal{N}f := \nabla \times \nabla \times \mathcal{S}(f), \quad (2.6)$$

where

$$\mathcal{S}(f) := \int_{\Omega} G(\mathbf{r} - \mathbf{r}') f(\mathbf{r}') d\mathbf{r}' \quad (2.7)$$

is the volume vector potential, G is the free-space scalar Green function

$$G(\mathbf{r}) := \frac{e^{-jk_0|\mathbf{r}-\mathbf{r}'|}}{4\pi|\mathbf{r}-\mathbf{r}'|}, \quad (2.8)$$

and $k_0 = \omega\sqrt{\epsilon_0\mu_0}$ is the free-space wavenumber. The equivalent current densities are given in terms of the fields as

$$\begin{aligned} \mathbf{j}(\mathbf{r}) &= c_e(\epsilon_r(\mathbf{r}) - 1)\mathbf{e}(\mathbf{r}), \\ \mathbf{m}(\mathbf{r}) &= c_m(\mu(\mathbf{r}) - 1)\mathbf{h}(\mathbf{r}). \end{aligned} \quad (2.9)$$

The JM-VIE formulation can be derived by combining (2.3), (2.4) and (2.9) to obtain (see [29, 85] for more details):

$$\boxed{(\mathcal{I} - \mathcal{M}\mathcal{T}) \begin{pmatrix} \mathbf{j} \\ \mathbf{m} \end{pmatrix} = \mathcal{C}\mathcal{M} \begin{pmatrix} \mathbf{e}_{\text{inc}} \\ \mathbf{h}_{\text{inc}} \end{pmatrix}}, \quad (2.10)$$

where

$$\mathcal{T} = \begin{pmatrix} \mathcal{N} & -c_e\mathcal{K} \\ c_m\mathcal{K} & \mathcal{N} \end{pmatrix}, \quad (2.11)$$

and

$$\mathcal{M} = \begin{pmatrix} \mathcal{M}_\epsilon & 0 \\ 0 & \mathcal{M}_\mu \end{pmatrix}, \quad \mathbf{c} = \begin{pmatrix} c_e \mathcal{I} & 0 \\ 0 & c_m \mathcal{I} \end{pmatrix}. \quad (2.12)$$

Here \mathcal{M}_ϵ and \mathcal{M}_μ are multiplication operators that multiply by the respective local functions $(\epsilon_r(\mathbf{r}) - 1)/\epsilon_r(\mathbf{r})$ and $(\mu_r(\mathbf{r}) - 1)/\mu_r(\mathbf{r})$.

The full JM-VIE formulation (2.10) is not necessary for the photonics applications of interest here since magnetic currents are not present. However, we include this formulation since we will later consider the effect on absorber quality of introducing magnetic conductivity alongside electric conductivity in order to match impedances. For the majority of this thesis we shall instead use the J-VIE formulation which is simply obtained from (2.10) by setting the magnetic current densities, \mathbf{m} , to zero, giving

$$\boxed{(\mathcal{I} - \mathcal{M}_\epsilon \mathcal{N}) \mathbf{j} = c_e \mathcal{M}_\epsilon \mathbf{e}_{\text{inc}}}. \quad (2.13)$$

Observe that the integral operators in the formulations (2.10) and (2.13) are both of the form *identity plus diagonal multiplier times compact*. Such operators are desirable in our setting for two main reasons: firstly, they are *second kind* integral operators which are well behaved in terms of accuracy and convergence; secondly, the influence of the material properties is confined to the diagonal multiplier \mathcal{M} . This second point means that the implementation of absorbing regions is particularly simple in this VIE setting since all we have to do is alter the entries in the multiplier \mathcal{M} in order to introduce absorption, with the rest of the machinery remaining unchanged. Furthermore, as we discuss in the next section, after the Galerkin testing procedure, the discrete forms of \mathcal{N} and \mathcal{K} both have block-Toeplitz structure when uniform meshing is employed, which enables the FFT-acceleration of the matrix-vector products associated with the iterative solver. This desirable structure is unaffected by

perturbing \mathcal{M} , hence the fast nature of the method remains.

2.3 Galerkin Discretization

There are numerous discretization techniques available for numerically solving the JM-VIE (2.10). Here we employ the Galerkin method over a uniform (“voxelized”) discretization of the domain. We embed the inhomogeneous dielectric object in a rectangular box of side lengths L_x , L_y and L_z and discretize it into voxels with side length Δ . That is, the constructed voxel grid consists of $N = X_x \times N_y \times N_z = L_x/\Delta \times L_y/\Delta \times L_z/\Delta$ elements. Next, the unknown equivalent currents should be expanded in terms of suitable basis functions. The equivalent currents are unlikely to satisfy any continuity conditions across the material interfaces, therefore $[\mathcal{L}^2(\mathbb{R}^3)]^3$ is their natural function space, where \mathcal{L}^2 is a function space of square integrable functions. In order to guarantee the convergence in norm of the solution, testing functions should span the \mathcal{L}^2 dual of the range space of the associated operator [83, 84]. The mapping properties of the JM-VIE formulation (2.10) read as

$$[\mathcal{L}^2(\mathbb{R}^3)]^3 \rightarrow [\mathcal{L}^2(\mathbb{R}^3)]^3 \quad (2.14)$$

and \mathcal{L}^2 is dual to itself, therefore when the Galerkin method with the identical basis and testing functions from $[\mathcal{L}^2(\mathbb{R}^3)]^3$ is applied, the convergence in norm of the solution is guaranteed. Therefore, we can approximate the unknown currents as

piecewise constant functions on the voxelized grid:

$$\begin{aligned}\mathbf{j} &\approx \sum_{i=1}^{N_x} w_{e_i}^x \mathbf{p}_i^x + \sum_{i=1}^{N_y} w_{e_i}^y \mathbf{p}_i^y + \sum_{i=1}^{N_z} w_{e_i}^z \mathbf{p}_i^z, \\ \mathbf{m} &\approx \sum_{i=1}^{N_x} w_{m_i}^x \mathbf{p}_i^x + \sum_{i=1}^{N_y} w_{m_i}^y \mathbf{p}_i^y + \sum_{i=1}^{N_z} w_{m_i}^z \mathbf{p}_i^z,\end{aligned}\tag{2.15}$$

where the weights $w_{e_i}^\alpha, w_{m_i}^\alpha$, $\alpha = x, y, z$ are to be determined, and

$$\mathbf{p}_i^\alpha(\mathbf{r}) = \begin{cases} \frac{\hat{\alpha}}{\sqrt{V}}, & \mathbf{r} \in V_i, \\ 0, & \mathbf{r} \notin V_i, \end{cases}\tag{2.16}$$

where V_i is the support voxel. The scaling by the square root of the voxel volume V is included so that

$$\langle \mathbf{p}_i^\alpha, \mathbf{p}_j^\beta \rangle = \delta_{\alpha\beta ij},\tag{2.17}$$

where $\langle \cdot, \cdot \rangle$ is the standard L^2 inner product and $\delta_{\alpha\beta ij}$ is the generalized Kronecker delta. Applying the Galerkin method to the JM-VIE (2.10) with the same testing functions \mathbf{p}_i gives rise to the linear system of $6N$ equations:

$$(\mathbf{I} - \mathbf{A}) \begin{pmatrix} \mathbf{w}_e \\ \mathbf{w}_m \end{pmatrix} = \mathbf{C} \begin{pmatrix} \mathbf{b}_e \\ \mathbf{b}_h \end{pmatrix},\tag{2.18}$$

where \mathbf{I} is the identity matrix; $\mathbf{w}_e = (\mathbf{w}_e^x, \mathbf{w}_e^y, \mathbf{w}_e^z)^T$ and $\mathbf{w}_m = (\mathbf{w}_m^x, \mathbf{w}_m^y, \mathbf{w}_m^z)^T$ are the vectors consisting of the unknown weights $w_{e_i}^\alpha$ and $w_{m_i}^\alpha$, respectively, and \mathbf{A} is

the discrete form of the integro-differential operator \mathcal{MT} (2.10):

$$\mathbf{A} = \begin{pmatrix} \mathbf{A}_{11} & -c_e \mathbf{A}_{12} \\ c_m \mathbf{A}_{21} & \mathbf{A}_{22} \end{pmatrix}, \quad (2.19)$$

where

$$(\mathbf{A}_{11})_{ij}^{\alpha\beta} = \langle \mathcal{M}_e \mathcal{N} \mathbf{p}_j^\beta, \mathbf{p}_i^\alpha \rangle, \quad (\mathbf{A}_{12})_{ij}^{\alpha\beta} = \langle \mathcal{M}_e \mathcal{K} \mathbf{p}_j^\beta, \mathbf{p}_i^\alpha \rangle, \quad (2.20)$$

$$(\mathbf{A}_{21})_{ij}^{\alpha\beta} = \langle \mathcal{M}_\mu \mathcal{K} \mathbf{p}_j^\beta, \mathbf{p}_i^\alpha \rangle, \quad (\mathbf{A}_{22})_{ij}^{\alpha\beta} = \langle \mathcal{M}_\mu \mathcal{N} \mathbf{p}_j^\beta, \mathbf{p}_i^\alpha \rangle; \quad (2.21)$$

and the right-hand side is

$$(\mathbf{b}_e)_i^\alpha = \langle \mathcal{M}_e \mathbf{e}_{\text{inc}}, \mathbf{p}_i^\alpha \rangle, \quad (\mathbf{b}_h)_i^\alpha = \langle \mathcal{M}_\mu \mathbf{h}_{\text{inc}}, \mathbf{p}_i^\alpha \rangle. \quad (2.22)$$

In this thesis, we represent the material properties, encapsulated in \mathcal{M}_e and \mathcal{M}_μ , as piecewise constant functions across the voxel grid. That is, we assume that \mathcal{M}_e and \mathcal{M}_μ are constant on each voxel with values defined at the voxel centers. This enables \mathcal{M}_e and \mathcal{M}_μ to be removed outside the inner products above, thereby allowing (2.18) to be written in the following simplified form:

$$\boxed{(\mathbf{I} - \mathbf{MT}) \begin{pmatrix} \mathbf{w}_e \\ \mathbf{w}_m \end{pmatrix} = \mathbf{CM} \begin{pmatrix} \mathbf{e}_{\text{inc}} \\ \mathbf{h}_{\text{inc}} \end{pmatrix}}, \quad (2.23)$$

where the diagonal material properties multipliers are

$$\mathbf{M} = \begin{pmatrix} \mathbf{M}_e & 0 \\ 0 & \mathbf{M}_\mu \end{pmatrix}, \quad \mathbf{C} = \begin{pmatrix} c_e \mathbf{I} & 0 \\ 0 & c_m \mathbf{I} \end{pmatrix}. \quad (2.24)$$

Here \mathbf{M}_ϵ and \mathbf{M}_μ are the diagonal matrices, corresponding to \mathcal{M}_ϵ and \mathcal{M}_μ , evaluated at voxel centers, respectively. The discrete form of the integral operator \mathcal{T} (2.11) is

$$\mathbf{T} = \begin{pmatrix} \mathbf{N} & -c_e \mathbf{K} \\ c_m \mathbf{K} & \mathbf{N} \end{pmatrix}, \quad (2.25)$$

where

$$\mathbf{N}_{ij}^{\alpha\beta} = \langle \mathcal{N} \mathbf{p}_j^\alpha, \mathbf{p}_i^\beta \rangle, \quad \mathbf{K}_{ij}^{\alpha\beta} = \langle \mathcal{K} \mathbf{p}_j^\alpha, \mathbf{p}_i^\beta \rangle; \quad (2.26)$$

and the right-hand side is

$$(\mathbf{e}_{\text{inc}})_i^\alpha = \langle \mathbf{e}_{\text{inc}}, \mathbf{p}_i^\alpha \rangle, \quad (\mathbf{h}_{\text{inc}})_i^\alpha = \langle \mathbf{h}_{\text{inc}}, \mathbf{p}_i^\alpha \rangle, \quad (2.27)$$

where $\alpha, \beta = x, y, z$.

In the case when magnetic currents are not present, (2.23) reduces to

$$\boxed{(\mathbf{I} - \mathbf{M}_\epsilon \mathbf{N}) \mathbf{w}_e = c_e \mathbf{M}_\epsilon \mathbf{e}_{\text{inc}}} \quad (2.28)$$

The uniform discretization we use is desirable because, as we will show in the next section, it results in the matrices \mathbf{N} and \mathbf{K} being block-Toeplitz, hence matrix-vector products using \mathbf{N} and \mathbf{K} can be performed in $\mathcal{O}(N \log N)$ operations with the use of the FFT, where N is the number of voxels. Further, the piecewise constant representation of the material properties means that introducing varying conductivity in an absorbing region does not interfere with the Toeplitz structure of \mathbf{N} and \mathbf{K} . It only affects the diagonal entries in the multiplier \mathbf{M} . This makes the implementation of absorbing regions in the VIE method particularly straightforward and does not compromise the speed-up. We will further provide the description of FFT-based acceleration in more detail in Section 2.6. Moreover, we will show in Chapter 4,

that even with this crude piecewise constant representation for higher-order polynomial conductivity profiles, our approach still recovers the asymptotic behavior of the reflection.

2.4 Reduction to surface-surface integrals

To assemble the matrices associated with the integro-differential operators, we need to evaluate the following integrals:

$$\mathbf{N}_{ij}^{\alpha\beta} = \int_{V_i} \mathbf{p}_i^\alpha \cdot \nabla \times \nabla \times \int_{V_j} G(\mathbf{r} - \mathbf{r}') \mathbf{p}_j^\beta dV' dV, \quad (2.29)$$

and

$$\mathbf{K}_{ij}^{\alpha\beta} = \int_{V_i} \mathbf{p}_i^\alpha \cdot \nabla \times \int_{V_j} G(\mathbf{r} - \mathbf{r}') \mathbf{p}_j^\beta dV' dV, \quad (2.30)$$

where $\alpha, \beta = x, y, z$ and V_i, V_j are the volumes of testing and basis voxels, respectively. The evaluation of these 6D (volume-volume) integrals can be rather involved, especially in the case when the support voxels of the basis and testing functions coincide or are adjacent. To avoid these complications, we use the dimensionality reduction method, proposed in [94] for the piece-wise constant basis and testing functions.

Moving the outer derivative in (2.29) to the testing function and using the diver-

gence theorem, we get

$$\begin{aligned}
\mathbf{N}_{ij}^{\alpha\beta} &= - \oint_{S_i} (\hat{\mathbf{n}} \times \mathbf{p}_i^\alpha) \cdot \int_{V_j} \nabla G(\mathbf{r} - \mathbf{r}') \times \mathbf{p}_j^\beta dV' dS \\
&= - \frac{1}{V} \oint_{S_i} (\hat{\mathbf{n}} \times \hat{\boldsymbol{\alpha}}) \cdot \int_{V_j} \nabla G(\mathbf{r} - \mathbf{r}') \times \hat{\boldsymbol{\beta}} dV' dS,
\end{aligned} \tag{2.31}$$

where $\hat{\boldsymbol{\alpha}}, \hat{\boldsymbol{\beta}} = \hat{\mathbf{x}}, \hat{\mathbf{y}}, \hat{\mathbf{z}}$, S_i is the surface of the testing voxel and $\hat{\mathbf{n}}$ is the outer normal vector to the surface S_i .

The basis and testing functions are obviously shift invariant from voxel to voxel, hence the integrals could be written as

$$\mathbf{N}_{ij}^{\alpha\beta} = - \frac{1}{V} \oint_{S_0} (\hat{\mathbf{n}} \times \hat{\boldsymbol{\alpha}}) \cdot \int_{V_0} \nabla G(\mathbf{r} - \mathbf{r}' + \mathbf{r}_i - \mathbf{r}'_j) \times \hat{\boldsymbol{\beta}} dV' dS, \tag{2.32}$$

where the support is fixed to one element (e.g. the 0th or reference element), and $\mathbf{r}_i, \mathbf{r}'_j$ denotes the centers of voxels i and j , respectively. Next, the constant vector $\hat{\boldsymbol{\beta}}$ can be moved outside the inner integral, therefore, with the help of the vector form of the divergence theorem and using the fact that $\nabla G = -\nabla G'$,

$$\mathbf{N}_{ij}^{\alpha\beta} = - \frac{1}{V} \oint_{S_0} (\hat{\mathbf{n}} \times \hat{\boldsymbol{\alpha}}) \cdot \hat{\boldsymbol{\beta}} \times \oint_{S'_0} G(\mathbf{r} - \mathbf{r}' + \mathbf{r}_i - \mathbf{r}'_j) \hat{\mathbf{n}}' dS' dS \tag{2.33}$$

and the original volume–volume integral is given by a series of surface–surface integrals over the faces of the voxels

$$\mathbf{N}_{ij}^{\alpha\beta} = - \frac{1}{V} \sum_k \int_{S_k} (\hat{\mathbf{n}}_k \times \hat{\boldsymbol{\alpha}}) \cdot \hat{\boldsymbol{\beta}} \times \sum_l \int_{S'_l} G(\mathbf{r} - \mathbf{r}' + \mathbf{r}_i - \mathbf{r}'_j) \hat{\mathbf{n}}'_l dS' dS, \tag{2.34}$$

where $k, l = -x, +x, -y, +y, -z, +z$ and $\hat{\mathbf{n}}_k, \hat{\mathbf{n}}_l'$ are the associated normal vectors.

Finally, the discrete operator \mathbf{N} reads

$$\mathbf{N}_{ij} = \begin{bmatrix} \mathbf{N}_{ij}^{xx} & \mathbf{N}_{ij}^{xy} & \mathbf{N}_{ij}^{xz} \\ \mathbf{N}_{ij}^{yx} & \mathbf{N}_{ij}^{yy} & \mathbf{N}_{ij}^{yz} \\ \mathbf{N}_{ij}^{zx} & \mathbf{N}_{ij}^{zy} & \mathbf{N}_{ij}^{zz} \end{bmatrix} \quad (2.35)$$

where

$$\mathbf{N}_{ij}^{\alpha\beta} = \frac{1}{V} \sum_k \sum_l (\hat{\mathbf{n}}_k \times \hat{\boldsymbol{\alpha}}) \cdot (\hat{\mathbf{n}}_l' \times \hat{\boldsymbol{\beta}}) N_{ij}^{kl} \quad (2.36)$$

and

$$N_{ij}^{kl} = \int_{S_k} \int_{S_l} G(\mathbf{r} - \mathbf{r}' + \mathbf{r}_i - \mathbf{r}_j') dS' dS. \quad (2.37)$$

Due to the convolutional nature of the discrete kernels in (2.37), i.e.,

$$N_{ij}^{kl} = N_{i-j}^{kl} \Rightarrow \mathbf{N}_{ij}^{\alpha\beta} = \mathbf{N}_{i-j}^{\alpha\beta} \Rightarrow \mathbf{N}_{ij} = \mathbf{N}_{i-j}, \quad (2.38)$$

the generated matrix is three-level block-Toeplitz Toeplitz-block, since we are dealing with the 3D case. As a result, the \mathbf{N} operator can be constructed by simply fixing the basis function (e.g. for the first voxel $j = 1$) and sweeping the testing function over all voxels of the solution domain.

The integral (2.30) can also be simplified in the case of piece-wise constant basis and testing functions:

$$\mathbf{K}_{ij}^{\alpha\beta} = -(\mathbf{p}_i \times \mathbf{p}_j) \cdot \int_{V_i} \int_{V_j} \nabla G dV' dV = -\frac{1}{V} (\hat{\boldsymbol{\alpha}} \times \hat{\boldsymbol{\beta}}) \cdot \int_{V_i} \int_{V_j} \nabla G dV' dV. \quad (2.39)$$

Next, using the divergence theorem for the inner integral, we obtain

$$\mathbf{K}_{ij}^{\alpha\beta} = \frac{1}{V}(\hat{\boldsymbol{\alpha}} \times \hat{\boldsymbol{\beta}}) \cdot \int_{V_i} \oint_{S_j} G \hat{\mathbf{n}}' dS' dV = \frac{1}{V}(\hat{\boldsymbol{\alpha}} \times \hat{\boldsymbol{\beta}}) \cdot \oint_{S_j} \hat{\mathbf{n}}' \int_{V_i} G dV dS'. \quad (2.40)$$

The remaining volume integral

$$\int_{V_i} G(\mathbf{R}) dV \quad (2.41)$$

can be handled with the technique proposed by Knockaert [124]:

$$\int_{V_i} G(\mathbf{R}) dV = \int_{V_i} \nabla \mathbf{F}(\mathbf{R}) dV = \oint_{S_i} \hat{\mathbf{n}} \cdot \mathbf{F}(\mathbf{R}) dS, \quad (2.42)$$

where

$$\mathbf{F}(\mathbf{R}) = \frac{1}{(jk)^2} \nabla \{G(\mathbf{R}) - G_0(\mathbf{R})\} \quad (2.43)$$

with $G_0(\mathbf{R}) = 1/4\pi R$ being the "static" Green function. Finally, the original volume-volume integral is represented as a following surface-surface integral:

$$\mathbf{K}_{ij}^{\alpha\beta} = (\hat{\boldsymbol{\alpha}} \times \hat{\boldsymbol{\beta}}) \cdot \oint_{S_j} \hat{\mathbf{n}}' \oint_{S_i} \hat{\mathbf{n}} \cdot \mathbf{F}(\mathbf{R}) dS dS'. \quad (2.44)$$

The next logic is the same as for \mathbf{N} operator. Note that the contribution from coincident surfaces to \mathbf{K} operator is identically zero, since $\hat{\mathbf{n}} \cdot \mathbf{F}(\mathbf{R}) = 0$ when $S_i \equiv S_j$.

We have reduced the original 6D volume-volume integrals into the series of 4D surface-surface integrals over the faces of the basis and testing voxels. It should be noted that the resulting surface-to-surface integrals have less singular kernels than the original volume-volume ones when the support of the basis and testing function coincide or are adjacent. The method of the integration of such kernels is described

in the next section.

2.5 Evaluation of Singular Integrals

We have demonstrated, that the original 6D volume-volume integrals required to the computation of the Galerkin inner products associated with the integral operators \mathcal{N} and \mathcal{K} , can be represented as a series of 4D surface-surface integrals over the faces of basis and testing voxels. In most of the cases, these integrals can be easily evaluated, e.g., using standard Gaussian quadratures. However, when the two faces of basis and testing voxels coincide, share an edge or share a vertex, the kernels of that integrals become singular when the observation point coincides with the source point. To evaluate these weakly and strongly singular integrals over the faces of voxels, we have developed the new fully numerical method for quadrilateral elements, which is an extension of DIRECTFN [123], previously developed for triangular ones.

In the following, we consider the general case of 4-D integrals,

$$I = \int_{E_P} \int_{E_Q} K(\mathbf{r}, \mathbf{r}') dA_Q dA_P, \quad (2.45)$$

where the two quadrilateral elements E_P and E_Q may coincide (self-term (ST) integration), share a common edge (edge adjacent (EA) integration), or share a common vertex (vertex adjacent (VA) integration). The scalar kernel $K(\mathbf{r}, \mathbf{r}')$ is typically singular when the observation points \mathbf{r} coincide with the source points \mathbf{r}' , i.e., $K(\mathbf{r}, \mathbf{r}') \sim |\mathbf{r} - \mathbf{r}'|^{-p}$ where $p = 1$ in weakly singular case and $p = 2$ in strongly singular case. By the various numerical tests presented further in this section, we demonstrate that the proposed algorithm is able to provide results with very high accuracy. We also show that the overall efficiency can be further enhanced by a

judicious choice of the integration order for each of the four dimensions. Finally, the complete set of codes is available as free, open-source software [125].

2.5.1 Rectangular Parametric Space

As a first step, we introduce a parametric space $\{u, v\}$, where

$$-1 \leq u \leq 1, \quad -1 \leq v \leq 1,$$

to transform the original arbitrary quadrilateral to a square (See Fig. 2-1):

$$\mathbf{r}(u, v) = \left[\begin{array}{l} (1-u)(1-v)\mathbf{r}_1 + (1+u)(1-v)\mathbf{r}_2 \\ +(1+u)(1+v)\mathbf{r}_3 + (1-u)(1+v)\mathbf{r}_4 \end{array} \right] / 4. \quad (2.46)$$

For simplicity, we derive all the formulas in this section for planar quadrilaterals,

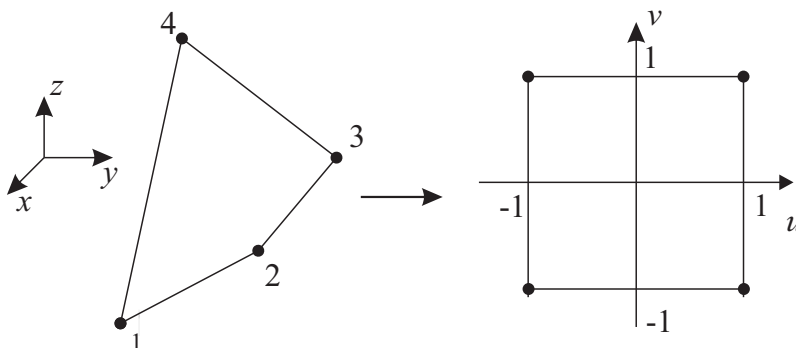


Figure 2-1: Geometry of parametric transformation of the original quadrilateral to a square.

since the extension to curvilinear elements is trivial. The remaining part of the algorithm, described in the next subsections, is completely the same for both cases. We have to note that this parametrization and all the successive formulas are not

only valid for planar elements, but they can also be applied without any changes for bilinear surfaces [114].

The area of the element dS can be expressed as

$$dS = |\mathbf{r}_u \times \mathbf{r}_v| du dv, \quad (2.47)$$

hence, the associated Jacobian reads

$$J(u, v) = |\mathbf{r}_u \times \mathbf{r}_v|, \quad (2.48)$$

where

$$\mathbf{r}_u \equiv \frac{\partial \mathbf{r}}{\partial u} = \frac{-\mathbf{r}_1 + \mathbf{r}_2 + \mathbf{r}_3 - \mathbf{r}_4 + v(\mathbf{r}_1 - \mathbf{r}_2 + \mathbf{r}_3 - \mathbf{r}_4)}{4}, \quad (2.49)$$

$$\mathbf{r}_v \equiv \frac{\partial \mathbf{r}}{\partial v} = \frac{-\mathbf{r}_1 - \mathbf{r}_2 + \mathbf{r}_3 + \mathbf{r}_4 + u(\mathbf{r}_1 - \mathbf{r}_2 + \mathbf{r}_3 - \mathbf{r}_4)}{4}. \quad (2.50)$$

In the new parametric space the original integral (2.45) takes the following form:

$$I = \int_{-1}^1 du \int_{-1}^1 J_P dv \int_{-1}^1 du' \int_{-1}^1 J_Q K(\mathbf{r}, \mathbf{r}') dv'. \quad (2.51)$$

For simplicity, in all successive derivations we will omit the integrands, when no confusion exists. The orientation of the quadrilaterals of the edge adjacent and vertex adjacent cases before the transformation to square space is shown in Fig. 2-2.

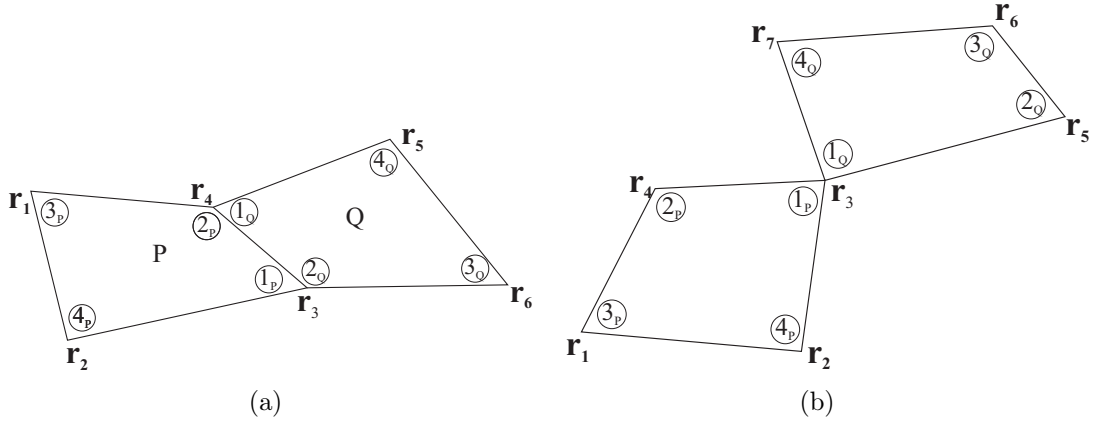


Figure 2-2: Orientation of the quadrilateral elements in space: (a) edge adjacent case; (b) vertex adjacent case.

2.5.2 Coincident Integration

First Step

We begin our derivation with introducing a polar coordinate system $\{\rho, \theta\}$ centered at the point (u, v) (depicted schematically in Fig. 2-3(a)),

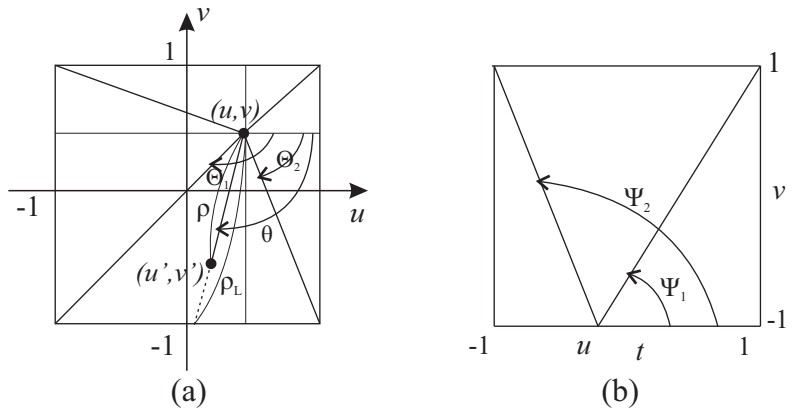


Figure 2-3: Geometry of the parametric transformations for the coincident case: (a) $\{u', v'\} \rightarrow \{\rho, \theta\}$; (b) $\{t, v\} \rightarrow \{\Lambda, \Psi\}$.

$$u' = u + \rho \cos(\theta), \quad v' = v + \rho \sin(\theta). \quad (2.52)$$

Since the upper limit of ρ , denoted as ρ_L , is different as θ traverses each edge, the (ρ, θ) integration must be split in four subtriangles. Here we present only the calculation for the lower subtriangle; the remaining three subtriangles can be handled by rotating the elements accordingly and using the formulas for the lower one, as shown in the following. For the lower subtriangle, the integration limits are

$$0 \leq \rho \leq \rho_L, \quad \Theta_1 \leq \theta \leq \Theta_2, \quad (2.53)$$

where

$$\rho_L = \frac{v+1}{\cos\left(\frac{\pi}{2} + \theta\right)}, \quad \Theta_1 = -\frac{\pi}{2} - \tan^{-1}\left(\frac{u+1}{v+1}\right), \quad \Theta_2 = -\frac{\pi}{2} + \tan^{-1}\left(\frac{1-u}{v+1}\right). \quad (2.54)$$

Note that here and below the counter-clockwise angle direction is taken as positive. Hence, the integral for the lower subtriangle is given by

$$I^{\text{sub}_1} = \int_{-1}^1 du \int_{-1}^1 dv \int_{\Theta_1}^{\Theta_2} d\theta \int_0^{\rho_L} \rho d\rho. \quad (2.55)$$

Second Step

We proceed by introducing the variable t , $-1 \leq t \leq 1$, via

$$\begin{aligned} \theta &= -\frac{\pi}{2} + \tan^{-1}\left(\frac{t-u}{1+v}\right), \\ \frac{d\theta}{dt} &= \frac{1+v}{(1+v)^2 + (t-u)^2} = F(u, v, t), \end{aligned} \quad (2.56)$$

which results in

$$\rho_L = \sqrt{(1+v)^2 + (t-u)^2}. \quad (2.57)$$

Interchanging the order of integration, (2.55) becomes

$$I^{\text{sub}_1} = \int_{-1}^1 du \int_{-1}^1 dt \int_{-1}^1 F(u, v, t) dv \int_0^{\rho_L} \rho d\rho. \quad (2.58)$$

Next, we replace $\{t, v\}$ with a new polar coordinate system $\{\Lambda, \Psi\}$:

$$t = u + \Lambda \cos(\Psi), \quad v = -1 + \Lambda \sin(\Psi), \quad (2.59)$$

with the Jacobian of this new transformation being $J = \Lambda$. With the two changes of variables, $\theta \rightarrow t$ and $\{t, v\} \rightarrow \{\Lambda, \Psi\}$, we obtain the following:

$$\begin{aligned} \cos(\theta) &\rightarrow \cos(\Psi), & \sin(\theta) &\rightarrow -\sin(\Psi), \\ \rho_L &\rightarrow \Lambda, & F &\rightarrow \frac{\sin(\Psi)}{\Lambda}. \end{aligned} \quad (2.60)$$

We have to notice that the $\{t, v\}$ domain is a rectangle (Fig. 2-3 (b)), and integrating over $\{\Lambda, \Psi\}$ will require a decomposition into three subdomains:

$$\Psi_0 \leq \Psi \leq \Psi_1, \quad \Psi_1 \leq \Psi \leq \Psi_2, \quad \Psi_2 \leq \Psi \leq \Psi_3,$$

where

$$\begin{aligned} \Psi_0 &= 0, & \Psi_1 &= \frac{\pi}{2} - \tan^{-1} \left(\frac{1-u}{2} \right), & \Psi_2 &= \frac{\pi}{2} + \tan^{-1} \left(\frac{1+u}{2} \right), \\ \Psi_3 &= \pi, \end{aligned} \quad (2.61)$$

and (2.58) is written as

$$I^{\text{sub}_1} = \sum_{m=0}^2 \int_{-1}^1 du \int_{\Psi_m}^{\Psi_{m+1}} \mathcal{F}(\Psi; \Lambda_L) d\Psi, \quad (2.62)$$

where

$$\mathcal{F}(\Psi; \Lambda_L) = \sin \Psi \int_0^{\Lambda_L} d\Lambda \int_0^{\Lambda} \rho d\rho \quad (2.63)$$

is the kernel that is omitted in the following derivations. The limit Λ_L for integration over Λ depends upon the subdomain ($m = 0,1,2$) being considered, as shown below.

Third step

We have reduced the singular integral (2.51) to an integration over $\{u, \Psi\}$ with the Ψ integral decomposed into three subintegrals. The final objective is to regularize further the integral with respect to u by placing it in front of the Ψ integral, so each subintegral has to be considered individually. The partition of the integral with respect to Ψ and the limits of integration with respect to Λ read

$$\begin{aligned} 0 \leq \Psi \leq \Psi_1, \quad \Lambda_L &= \frac{1-u}{\cos(\Psi)}, \\ \Psi_1 \leq \Psi \leq \Psi_2, \quad \Lambda_L &= \frac{2}{\sin \Psi}, \\ \Psi_2 \leq \Psi \leq \Psi_3, \quad \Lambda_L &= \frac{1+u}{-\cos \Psi}. \end{aligned} \quad (2.64)$$

Integration over region $0 \leq \Psi \leq \Psi_1$ The domain of integration is depicted schematically in Fig. 2-4(a), below the curve $\Psi_1(u)$. After interchanging the u and

Ψ integration, we get

$$\int_{-1}^1 du \int_0^{\Psi_1} d\Psi = \int_0^{\frac{\pi}{4}} d\Psi \int_{-1}^1 du + \int_{\frac{\pi}{4}}^{\frac{\pi}{2}} d\Psi \int_{u_{1\psi}}^1 du, \quad (2.65)$$

where

$$u_{1\psi} = 2 \tan\left(\Psi - \frac{\pi}{2}\right) + 1. \quad (2.66)$$

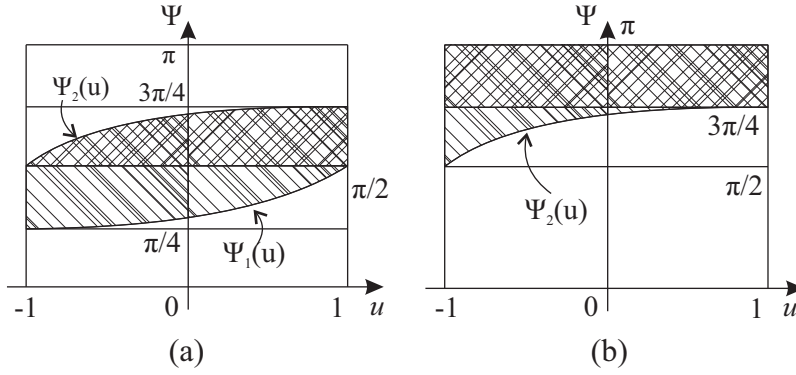


Figure 2-4: Geometry of the parametric space $\{u, \Psi\}$: (a) $0 \leq \Psi \leq \Psi_1$ and $\Psi_1 \leq \Psi \leq \Psi_2$; (b) $\Psi_2 \leq \Psi \leq \pi$.

Integration over region $\Psi_1 \leq \Psi \leq \Psi_2$ The domain of integration is shown as the shaded area in Fig. 2-4(a). After re-ordering the integration, we end up the following two integrals:

$$\int_{-1}^1 du \int_{\Psi_1}^{\Psi_2} d\Psi = \int_{\frac{\pi}{4}}^{\frac{\pi}{2}} d\Psi \int_{-1}^{u_{1\psi}} du + \int_{\frac{\pi}{2}}^{\frac{3\pi}{4}} d\Psi \int_{u_{2\psi}}^1 du, \quad (2.67)$$

where

$$u_{1\psi} = 2 \tan\left(\Psi - \frac{\pi}{2}\right) + 1, \quad u_{2\psi} = 2 \tan\left(\Psi - \frac{\pi}{2}\right) - 1. \quad (2.68)$$

Integration over region $\Psi_2 \leq \Psi \leq \pi$ The domain of integration in this case is depicted in Fig. 2-4(b). After re-ordering the integration, we obtain

$$\int_{-1}^1 du \int_{\Psi_2}^{\pi} d\Psi = \int_{\frac{\pi}{2}}^{\frac{3\pi}{4}} d\Psi \int_{-1}^{u_{2\psi}} du + \int_{\frac{3\pi}{4}}^{\pi} d\Psi \int_{-1}^1 du, \quad (2.69)$$

where

$$u_{2\psi} = 2 \tan\left(\Psi - \frac{\pi}{2}\right) - 1. \quad (2.70)$$

Final Formulas

Finally, the singular integral (2.51) for the lower subtriangle has been reduced to the following 6 sufficiently smooth integrals:

$$\begin{aligned} I^{\text{sub}_1} = & \int_0^{\frac{\pi}{4}} d\Psi \int_{-1}^1 du + \int_{\frac{\pi}{4}}^{\frac{\pi}{2}} d\Psi \int_{u_{1\psi}}^1 du + \int_{\frac{\pi}{2}}^{\frac{\pi}{2}} d\Psi \int_{-1}^{u_{1\psi}} du \\ & + \int_{\frac{\pi}{2}}^{\frac{3\pi}{4}} d\Psi \int_{u_{2\psi}}^1 du + \int_{\frac{\pi}{2}}^{\frac{3\pi}{4}} d\Psi \int_{-1}^{u_{2\psi}} du + \int_{\frac{3\pi}{4}}^{\pi} d\Psi \int_{-1}^1 du, \end{aligned} \quad (2.71)$$

where

$$u_{1\psi} = 2 \tan\left(\Psi - \frac{\pi}{2}\right) + 1, \quad u_{2\psi} = 2 \tan\left(\Psi - \frac{\pi}{2}\right) - 1. \quad (2.72)$$

The overall Jacobian after all parametric transformations is given by

$$\mathcal{J}^{\text{ST}} = (J_P J_Q) \rho \sin \Psi, \quad (2.73)$$

while the original variables take the following form:

$$\begin{aligned} u &\rightarrow u, v \rightarrow \Lambda \sin(\Psi) - 1, \\ u' &\rightarrow u + \rho \cos(\Psi), v' = -\rho \sin(\Psi) + \Lambda \sin(\Psi) - 1. \end{aligned} \tag{2.74}$$

Exploiting the symmetry of the rectangular parameter space, we can derive the formulas for the other three subtriangles by simply rotating them accordingly and employing the formulas for the lower one. Hence, the final formula for the original singular integral (2.51) is given by

$$I = I^{\text{sub}_1} + I^{\text{sub}_2} + I^{\text{sub}_3} + I^{\text{sub}_4}, \tag{2.75}$$

where

$$I^{\text{sub}_2} = I^{\text{sub}_1} \left| \begin{array}{c} u \\ v \end{array} \right| \rightarrow \begin{bmatrix} 0 & -1 \\ 1 & 0 \end{bmatrix} \begin{bmatrix} u \\ v \end{bmatrix}, \quad I^{\text{sub}_3} = I^{\text{sub}_1} \left| \begin{array}{c} u \\ v \end{array} \right| \rightarrow \begin{bmatrix} 0 & -1 \\ -1 & 0 \end{bmatrix} \begin{bmatrix} u \\ v \end{bmatrix} \tag{2.76}$$

and

$$I^{\text{sub}_4} = I^{\text{sub}_1} \left| \begin{array}{c} u \\ v \end{array} \right| \rightarrow \begin{bmatrix} 0 & 1 \\ -1 & 0 \end{bmatrix} \begin{bmatrix} u \\ v \end{bmatrix}. \tag{2.77}$$

2.5.3 Edge Adjacent Integration

First Step

Based upon the coincident integration scheme, we employ a polar coordinate transformation for the inner integration to cancel the line of singularity defined by

$$\begin{aligned} v = v' = -1, \quad u = -u', \\ u' = \rho \cos(\theta) - u, \quad v' = \rho \sin(\theta) - 1. \end{aligned} \tag{2.78}$$

The integration with respect to θ should be split into three terms, as illustrated in

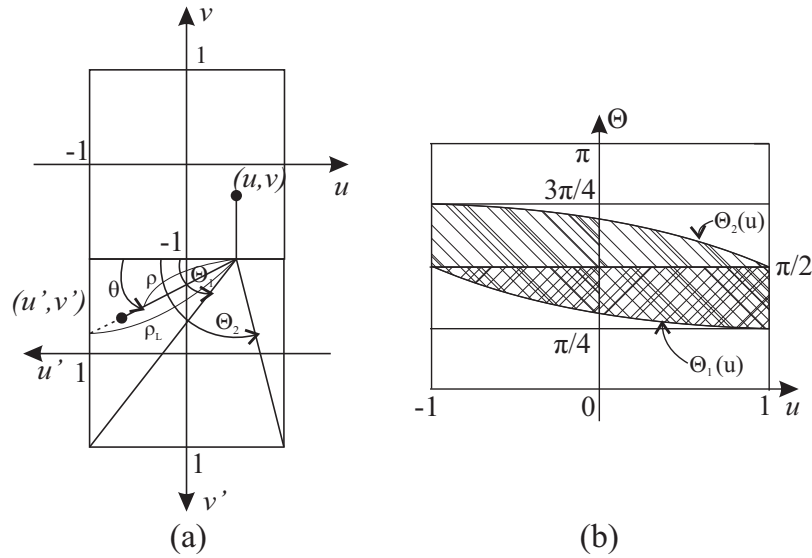


Figure 2-5: Edge adjacent integration: (a) polar coordinate transformation $\{u', v'\} \rightarrow \{\rho, \theta\}$; (b) the $\{u, \theta\}$ domain for the second shift of the integral, $\Theta_1 \leq \theta \leq \Theta_2$.

Fig. 2-5(a):

$$I = I_{\text{sub}_1} + I_{\text{sub}_2} + I_{\text{sub}_3}, \tag{2.79}$$

where

$$\begin{aligned}
I_{\text{sub}_1} &= \int_{-1}^1 du \int_{-1}^1 dv \int_0^{\Theta_1(u)} d\theta \int_0^{L_1} \rho d\rho, \\
I_{\text{sub}_2} &= \int_{-1}^1 du \int_{-1}^1 dv \int_{\Theta_1(u)}^{\Theta_2(u)} d\theta \int_0^{L_2} \rho d\rho, \\
I_{\text{sub}_3} &= \int_{-1}^1 du \int_{-1}^1 dv \int_{\Theta_2(u)}^{\pi} d\theta \int_0^{L_3} \rho d\rho
\end{aligned} \tag{2.80}$$

and

$$\begin{aligned}
\Theta_1(u) &= \frac{\pi}{2} - \tan^{-1} \left(\frac{1+u}{2} \right), \\
\Theta_2(u) &= \frac{\pi}{2} + \tan^{-1} \left(\frac{1-u}{2} \right),
\end{aligned} \tag{2.81}$$

$$L_1 = \frac{1+u}{\cos(\theta)}, \quad L_2 = \frac{2}{\sin(\theta)}, \quad L_3 = \frac{u-1}{\cos(\theta)}. \tag{2.82}$$

Since the break-points in θ are only functions of u , the integration can be rearranged as follows:

$$\begin{aligned}
I_{\text{sub}_1} &= \int_{-1}^1 du \int_0^{\Theta_1(u)} d\theta \int_{-1}^1 dv \int_0^{L_1} \rho d\rho, \\
I_{\text{sub}_2} &= \int_{-1}^1 du \int_{\Theta_1(u)}^{\Theta_2(u)} d\theta \int_{-1}^1 dv \int_0^{L_2} \rho d\rho, \\
I_{\text{sub}_3} &= \int_{-1}^1 du \int_{\Theta_2(u)}^{\pi} d\theta \int_{-1}^1 dv \int_0^{L_3} \rho d\rho.
\end{aligned} \tag{2.83}$$

Now the singularity occurs when $v = -1$ and $\rho = 0$, therefore we proceed by introducing a second polar coordinate transformation,

$$\rho = \Lambda \cos(\Psi), \quad v = -1 + \Lambda \sin(\Psi), \quad J_2 = \Lambda. \tag{2.84}$$

The original integral can be represented as a sum:

$$I = \sum_{l=0}^2 \sum_{m=0}^1 \int_{-1}^1 du \int_{\Theta_l}^{\Theta_{l+1}} d\theta \int_{\Psi_m}^{\Psi_{m+1}} \mathcal{G}(\Psi; \Lambda_L) d\Psi, \quad (2.85)$$

where

$$\mathcal{G}(\Psi; \Lambda_L) = \cos \Psi \int_0^{\Lambda_L} \Lambda^2 d\Lambda \quad (2.86)$$

can be evaluated numerically and is omitted in the following derivations. The integration limits in (2.85) are given by

$$\begin{aligned} \Theta_0 &= 0, & \Theta_1 &= \frac{\pi}{2} - \tan^{-1} \frac{1+u}{2}, \\ \Theta_2 &= \frac{\pi}{2} + \tan^{-1} \frac{1-u}{2}, & \Theta_3 &= \pi, \end{aligned} \quad (2.87)$$

and

$$\Psi_0 = 0, \quad \Psi_1 = \tan^{-1} \left(\frac{2}{L(u, \theta)} \right), \quad \Psi_2 = \frac{\pi}{2}, \quad (2.88)$$

while the integration limits with respect to Λ are given below.

Second Step

Integration over region $\Theta_1 \leq \theta \leq \Theta_2$ In this case, the splitting of Ψ integrals is independent of u and the integral is given by

$$I^{\theta_{12}} = \int_{-1}^1 du \int_{\Theta_1}^{\Theta_2} d\theta \int_0^{\Psi_1^{12}} d\Psi + \int_{-1}^1 du \int_{\Theta_1}^{\Theta_2} d\theta \int_{\Psi_1^{12}}^{\frac{\pi}{2}} d\Psi, \quad (2.89)$$

where the upper limit of Λ in (2.86) is different in the two terms:

$$\Lambda_L = \begin{cases} \frac{L_2}{\cos(\Psi)} = \frac{2}{\sin(\theta)\cos(\Psi)}, & 0 < \Psi < \Psi_1^{12}, \\ \frac{2}{\sin\Psi}, & \Psi_1^{12} < \Psi < \frac{\pi}{2}. \end{cases} \quad (2.90)$$

Moreover,

$$\theta_{1u} \equiv \Theta_1 = \frac{\pi}{2} - \tan^{-1}\left(\frac{1+u}{2}\right), \quad (2.91)$$

$$\theta_{2u} \equiv \Theta_2 = \frac{\pi}{2} + \tan^{-1}\left(\frac{1-u}{2}\right), \quad (2.92)$$

and the integral with respect to Ψ is split at

$$\Psi_1^{12} = \tan^{-1}\left(\frac{2}{L_2}\right) = \tan^{-1}(\sin\theta). \quad (2.93)$$

Hence, once u and θ are interchanged, the u can be moved immediately past the Ψ integral. Noting that

$$\theta_{1u}(-1) = \frac{\pi}{2}, \quad \theta_{1u}(1) = \frac{\pi}{4}, \quad \theta_{2u}(-1) = \frac{3\pi}{4}, \quad \theta_{2u}(1) = \frac{\pi}{2}, \quad (2.94)$$

the geometry for interchanging u and θ is shown in Fig. 2-5(b). Inverting the relationships between u and θ yields

$$u_{1\theta} = 2 \tan\left(\frac{\pi}{2} - \theta\right) - 1, \quad u_{2\theta} = 2 \tan\left(\frac{\pi}{2} - \theta\right) + 1, \quad (2.95)$$

while switching the integrals results in

$$\begin{aligned}
I^{\theta_{12}} = & \underbrace{\int_{\frac{\pi}{4}}^{\frac{\pi}{2}} d\theta \int_0^{\Psi_1^{12}} d\Psi \int_{u_{1\theta}}^1 du + \int_{\frac{\pi}{2}}^{\frac{3\pi}{4}} d\theta \int_0^{\Psi_1^{12}} d\Psi \int_{-1}^{u_{2\theta}} du}_{I^{\theta_{12}, \Psi^-}} \\
& + \underbrace{\int_{\frac{\pi}{4}}^{\frac{\pi}{2}} d\theta \int_{\Psi_1^{12}}^{\frac{\pi}{2}} d\Psi \int_{u_{1\theta}}^1 du + \int_{\frac{\pi}{2}}^{\frac{3\pi}{4}} d\theta \int_{\Psi_1^{12}}^{\frac{\pi}{2}} d\Psi \int_{-1}^{u_{2\theta}} du}_{I^{\theta_{12}, \Psi^+}}. \quad (2.96)
\end{aligned}$$

Integration over region $0 < \theta \leq \Theta_1$ In this case, the breakpoint in Ψ is a function of θ and u both, and re-ordering of integrations will produce eight integrals.

The two first integrals are given by

$$I^{\theta_1} = \int_{-1}^1 du \int_0^{\Theta_1} d\theta \int_0^{\Psi_1^1} d\Psi + \int_{-1}^1 du \int_0^{\Theta_1} d\theta \int_{\Psi_1^1}^{\frac{\pi}{2}} d\Psi, \quad (2.97)$$

where

$$\Lambda_L = \begin{cases} \frac{L_1}{\cos(\Psi)} = \frac{1+u}{\cos(\theta) \cos(\Psi)}, & 0 < \Psi < \Psi_1^1, \\ \frac{2}{\sin(\Psi)}, & \Psi_1^1 < \Psi < \frac{\pi}{2}, \end{cases} \quad (2.98)$$

and

$$\Psi_1^1 = \frac{\pi}{2} - \tan^{-1} \left(\frac{1+u}{2 \cos(\theta)} \right). \quad (2.99)$$

Again, the θ and u integrals are easily interchanged. The domain of integration is depicted schematically at Fig. 2-5(b), below the curve $\Theta_1(u)$. We end up with the

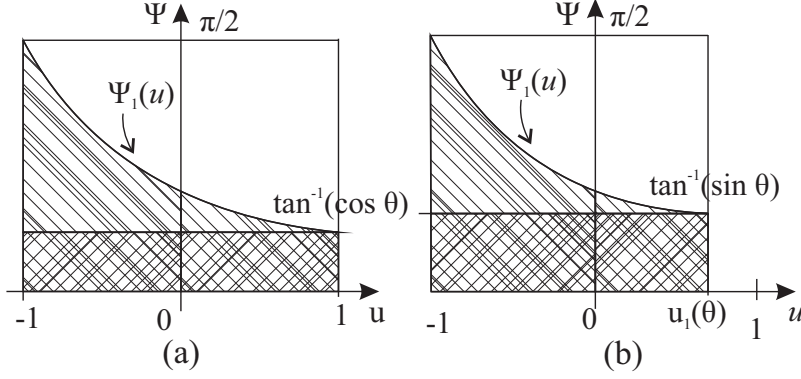


Figure 2-6: Polar coordinate transformations employed in the edge adjacent integration: the domain for interchanging the integrals $\{u, \Psi\}$, for a fixed value of θ ($0 \leq \theta \leq \Theta_1$): (a) $u_1(\theta) = 1$ ($0 \leq \theta \leq \pi/4$); (b) $u_1(\theta) < 1$ ($\pi/4 < \theta \leq \pi/2$).

following four integrals:

$$\begin{aligned}
 I^{\theta_1} = & \underbrace{\int_0^{\pi/4} d\theta \int_{-1}^1 du \int_0^{\Psi_1^1} d\Psi + \int_{\pi/4}^{\pi/2} d\theta \int_{-1}^{u_{1\theta}} du \int_0^{\Psi_1^1} d\Psi}_{I^{\theta_1, \Psi^-}} \\
 & + \underbrace{\int_0^{\pi/4} d\theta \int_{-1}^1 du \int_{\Psi_1^1}^{\pi/2} d\Psi + \int_{\pi/4}^{\pi/2} d\theta \int_{-1}^{u_{1\theta}} du \int_{\Psi_1^1}^{\pi/2} d\Psi}_{I^{\theta_1, \Psi^+}}, \quad (2.100)
 \end{aligned}$$

where the expression for $u_{1\theta}$ is given in (2.95). The next step is to regularize further the integral by interchanging of u and Ψ .

Integration over region $0 < \Psi \leq \Psi_1^1$ The domain under consideration is shown in Figs. 2-6(a-b), below the curve $\Psi_1(u)$. Moving the u integral to the front in the first two integrals in (2.100), corresponding to the case of $0 < \Psi \leq \Psi_1^1$, results

in

$$\begin{aligned}
I^{\theta_1, \Psi^-} = & \int_0^{\frac{\pi}{4}} d\theta \int_0^{\Psi_\theta^1} d\Psi \int_{-1}^1 du + \int_0^{\frac{\pi}{4}} d\theta \int_{\Psi_\theta^1}^{\frac{\pi}{2}} d\Psi \int_{-1}^{u_{1\psi}} du \\
& + \int_{\frac{\pi}{4}}^{\frac{\pi}{2}} d\theta \int_0^{\Psi_\theta^2} d\Psi \int_{-1}^{u_{1\theta}} du + \int_{\frac{\pi}{4}}^{\frac{\pi}{2}} d\theta \int_{\Psi_\theta^2}^{\frac{\pi}{2}} d\Psi \int_{-1}^{u_{1\psi}} du, \quad (2.101)
\end{aligned}$$

where

$$\begin{aligned}
u_{1\psi} &= 2 \cos(\theta) \cdot \tan\left(\frac{\pi}{2} - \Psi\right) - 1, \\
u_{1\theta} &= 2 \tan\left(\frac{\pi}{2} - \theta\right) - 1, \\
\Psi_\theta^1 &= \Psi_1^1|_{u=1} = \tan^{-1}(\cos(\theta)), \\
\Psi_\theta^2 &= \Psi_1^1|_{u=u_{1\theta}} = \tan^{-1}(\sin(\theta)).
\end{aligned} \quad (2.102)$$

Integration over region $\Psi_1^1 < \Psi \leq \pi/2$ After interchanging u and Ψ the last two integrals in (2.100), corresponding to $\Psi_1^1 < \Psi \leq \pi/2$ (the region depicted in Figs. 2-6(a-b) under the curve $\Psi_1(u)$), become

$$I^{\theta_1, \Psi^+} = \int_0^{\frac{\pi}{4}} d\theta \int_{\Psi_\theta^1}^{\frac{\pi}{2}} d\Psi \int_{u_{1\psi}}^1 du + \int_{\frac{\pi}{4}}^{\frac{\pi}{2}} d\theta \int_{\Psi_\theta^2}^{\frac{\pi}{2}} d\Psi \int_{u_{1\psi}}^{u_{1\theta}} du. \quad (2.103)$$

Integration over region $\Theta_2 < \theta \leq \pi$ This case is similar to the previous one.

The two first integrals are given by

$$I^{\theta_2} = \int_{-1}^1 du \int_{\Theta_2}^{\pi} d\theta \int_0^{\Psi_1^2} d\Psi + \int_{-1}^1 du \int_{\Theta_2}^{\pi} d\theta \int_{\Psi_1^2}^{\frac{\pi}{2}} d\Psi, \quad (2.104)$$

where the upper limit of Λ is

$$\Lambda_L = \begin{cases} \frac{L_3}{\cos(\Psi)} = \frac{u-1}{\cos(\theta)\cos(\Psi)}, & 0 < \Psi < \Psi_1^2, \\ \frac{2}{\sin(\Psi)}, & \Psi_1^2 < \Psi < \frac{\pi}{2}, \end{cases} \quad (2.105)$$

and

$$\Psi_1^2 = \frac{\pi}{2} - \tan^{-1} \left(\frac{u-1}{2\cos(\theta)} \right). \quad (2.106)$$

The θ and u integrals can be interchanged, and the domain is depicted in Fig. 2-7(a) under the curve $\Theta_2(u)$. After the interchanging we obtain

$$I^{\theta_2} = \underbrace{\int_{\frac{\pi}{2}}^{\frac{3\pi}{4}} d\theta \int_{u_{2\theta}}^1 du \int_0^{\Psi_1^2} d\Psi + \int_{\frac{3\pi}{4}}^{\pi} d\theta \int_{-1}^1 du \int_0^{\Psi_1^2} d\Psi}_{I^{\theta_2, \Psi^-}} + \underbrace{\int_{\frac{\pi}{2}}^{\frac{3\pi}{4}} d\theta \int_{u_{2\theta}}^1 du \int_{\Psi_1^2}^{\frac{\pi}{2}} d\Psi + \int_{\frac{3\pi}{4}}^{\pi} d\theta \int_{-1}^1 du \int_{\Psi_1^2}^{\frac{\pi}{2}} d\Psi}_{I^{\theta_2, \Psi^+}}, \quad (2.107)$$

where $u_{2\theta}$ is given in (2.95). The final step is the interchanging of u and Ψ , and the associated geometry is shown in Figs. 2-7(b-c).

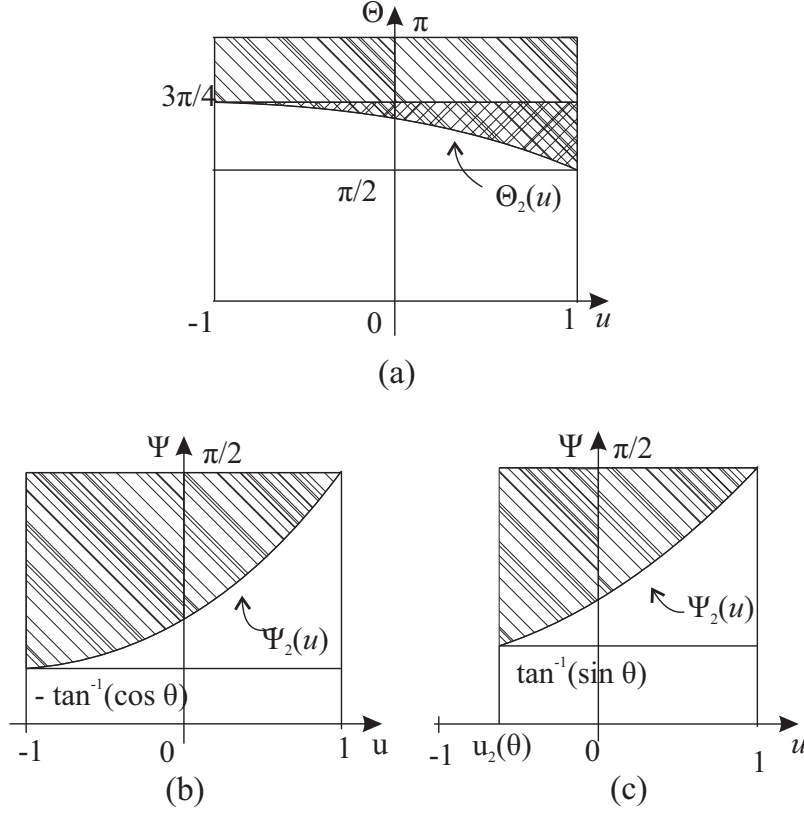


Figure 2-7: Polar coordinate transformations employed in the edge adjacent integration: (a) the $\{u, \theta\}$ domain for the third shift of the integral, $\Theta_2 \leq \theta \leq \pi$; (b) the domain for interchanging the integrals $\{u, \Psi\}$, for a fixed value of θ and $u_2(\theta) = -1$ ($\pi/2 \leq \theta \leq 3\pi/4$); and (c) the domain for interchanging the integrals $\{u, \Psi\}$, for a fixed value of θ and $u_2(\theta) > -1$ ($3\pi/4 < \theta \leq \pi$).

Integration over region $0 < \Psi \leq \Psi_1^2$ After moving the u integral to the front, the first two integrals in (2.107) read

$$\begin{aligned}
 I^{\theta_2, \Psi^-} = & \int_{\frac{\pi}{2}}^{\frac{3\pi}{4}} d\theta \int_0^{\Psi_\theta^2} d\Psi \int_{u_{2\theta}}^1 du + \int_{\frac{\pi}{2}}^{\frac{3\pi}{4}} d\theta \int_{\Psi_\theta^2}^{\frac{\pi}{2}} d\Psi \int_{u_{2\psi}}^1 du \\
 & + \int_{\frac{3\pi}{4}}^{\pi} d\theta \int_0^{-\Psi_\theta^1} d\Psi \int_{-1}^1 du + \int_{\frac{3\pi}{4}}^{\pi} d\theta \int_{-\Psi_\theta^1}^{\frac{\pi}{2}} d\Psi \int_{u_{2\psi}}^1 du, \quad (2.108)
 \end{aligned}$$

where

$$\begin{aligned}
u_{2\psi} &= 2 \cos(\theta) \cdot \tan\left(\frac{\pi}{2} - \Psi\right) + 1, \\
u_{2\theta} &= 2 \tan\left(\frac{\pi}{2} - \theta\right) + 1, \\
-\Psi_\theta^1 &= \Psi_1^2|_{u=-1} = -\tan^{-1}(\cos(\theta)), \\
\Psi_\theta^2 &= \Psi_1^2|_{u=u_{2\theta}} = \tan^{-1}(\sin(\theta)).
\end{aligned} \tag{2.109}$$

Integration over region $\Psi_1^2 < \Psi \leq \pi/2$ The last two integrals in (2.107), corresponding to the case of $\Psi_1^2 < \Psi \leq \pi/2$, become

$$I^{\theta_2, \Psi^+} = \int_{\frac{\pi}{2}}^{\frac{3\pi}{4}} d\theta \int_{\Psi_\theta^2}^{\frac{\pi}{2}} d\Psi \int_{u_{2\theta}}^{u_{2\psi}} du + \int_{\frac{3\pi}{4}}^{\pi} d\theta \int_{-\Psi_\theta^1}^{\frac{\pi}{2}} d\Psi \int_{-1}^{u_{2\psi}} du. \tag{2.110}$$

According to (2.85), the initial integral for edge adjacent case will read

$$I = I^{\theta_1, \Psi^-} + I^{\theta_1, \Psi^+} + I^{\theta_{12}, \Psi^-} + I^{\theta_{12}, \Psi^+} + I^{\theta_2, \Psi^-} + I^{\theta_2, \Psi^+}. \tag{2.111}$$

The resulting Jacobian (including the part of the rectangular parameter space) is given with the help of (2.86) and reads

$$\mathcal{I}^{\text{EA}} = (J_P J_Q) \Lambda^2 \cos \Psi \tag{2.112}$$

and the original variables can be written as

$$\begin{aligned}
u &\rightarrow u, & v &\rightarrow -1 + \Lambda \sin \Psi, \\
u' &\rightarrow \Lambda \cos \Psi \cos \theta - u, & v' &\rightarrow \Lambda \cos \Psi \sin \theta - 1.
\end{aligned} \tag{2.113}$$

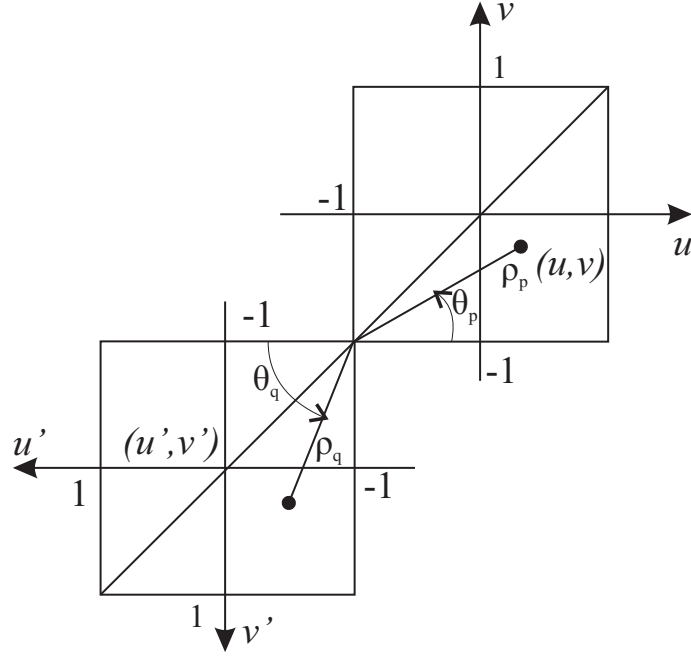


Figure 2-8: Polar coordinate transformations employed in vertex adjacent integration: $\{u, v\} \rightarrow \{\rho_p, \theta_p\}$, $\{u', v'\} \rightarrow \{\rho_q, \theta_q\}$.

2.5.4 Vertex Adjacent Integration

In the case where the source and observation quadrilaterals share only a single vertex, we begin by orienting the elements so that the singular point is at $u = u' = -1$, $v = v' = -1$. Next, we introduce a separate coordinate system for each element, as shown at Fig. 2-8:

$$\begin{aligned}
 u &= -1 + \rho_p \cos(\theta_p), & v &= -1 + \rho_p \sin(\theta_p), \\
 u' &= -1 + \rho_q \cos(\theta_q), & v' &= -1 + \rho_q \sin(\theta_q).
 \end{aligned}
 \tag{2.114}$$

This results in four integrals:

$$\begin{aligned}
I = & \int_0^{\frac{\pi}{4}} d\theta_p \int_0^{L_p^1} \rho_p d\rho_p \int_0^{\frac{\pi}{4}} d\theta_q \int_0^{L_q^1} \rho_q d\rho_q + \int_0^{\frac{\pi}{4}} d\theta_p \int_0^{L_p^1} \rho_p d\rho_p \int_{\frac{\pi}{4}}^{\frac{\pi}{2}} d\theta_q \int_0^{L_q^2} \rho_q d\rho_q \\
& + \int_{\frac{\pi}{4}}^{\frac{\pi}{2}} d\theta_p \int_0^{L_p^2} \rho_p d\rho_p \int_0^{\frac{\pi}{4}} d\theta_q \int_0^{L_q^1} \rho_q d\rho_q + \int_{\frac{\pi}{4}}^{\frac{\pi}{2}} d\theta_p \int_0^{L_p^2} \rho_p d\rho_p \int_{\frac{\pi}{4}}^{\frac{\pi}{2}} d\theta_q \int_0^{L_q^2} \rho_q d\rho_q,
\end{aligned} \tag{2.115}$$

where

$$\begin{aligned}
L_p^1 &= \frac{2}{\cos(\theta_p)}, & L_p^2 &= \frac{2}{\sin(\theta_p)}, \\
L_q^1 &= \frac{2}{\cos(\theta_q)}, & L_q^2 &= \frac{2}{\sin(\theta_q)}.
\end{aligned} \tag{2.116}$$

The singularity is at the common vertex $\rho_p = \rho_q = 0$, so it's reasonable to use a polar coordinate transformation,

$$\rho_p = \Lambda \cos(\Psi), \quad \rho_q = \Lambda \sin(\Psi). \tag{2.117}$$

Since the $\{\rho_p, \rho_q\}$ domain is rectangular, the Ψ integration must be split into two pieces, which leads to the final eight integrals,

$$\begin{aligned}
I = & \sum_{m=1}^2 \sum_{n=1}^2 \int_{\Theta_{m-1}}^{\Theta_m} d\theta_p \int_{\Theta_{n-1}}^{\Theta_n} d\theta_q \\
& \times \left[\int_0^{\Psi_1^{m,n}} \mathcal{H}(\Psi; L_1^{m,n}) d\Psi + \int_{\Psi_1^{m,n}}^{\frac{\pi}{2}} \mathcal{H}(\Psi; L_2^{m,n}) d\Psi \right], \tag{2.118}
\end{aligned}$$

where

$$\mathcal{H}(\Psi; L_i^{m,n}) = \cos \Psi \sin \Psi \int_0^{L_i^{m,n}(\Psi)} \Lambda^3 d\Lambda, \quad i = 1, 2, \tag{2.119}$$

and the integration limits are given by

$$\begin{aligned}\Theta_0 &= 0, & \Theta_1 &= \frac{\pi}{4}, & \Theta_2 &= \frac{\pi}{2}, \\ L_1^{m,n}(\Psi) &= \frac{L_p^m(\theta_p)}{\cos(\Psi)}, & L_2^{m,n}(\Psi) &= \frac{L_q^n(\theta_q)}{\sin(\Psi)}, \\ \Psi_1^{m,n} &= \tan^{-1}\left(\frac{L_q^n}{L_p^m}\right).\end{aligned}\tag{2.120}$$

The final Jacobian takes the form

$$\mathcal{J}^{\text{VA}} = (J_P J_Q) \Lambda^3 \cos \Psi \sin \Psi\tag{2.121}$$

and the original variables are given by

$$\begin{aligned}u &\rightarrow -1 + \Lambda \cos \Psi \cos \theta_p, & v &\rightarrow -1 + \Lambda \cos \Psi \sin \theta_p, \\ u' &\rightarrow -1 + \Lambda \sin \Psi \cos \theta_q, & v' &\rightarrow -1 + \Lambda \sin \Psi \sin \theta_q.\end{aligned}\tag{2.122}$$

2.5.5 Numerical tests

Here we demonstrate the effectiveness of the proposed algorithm in terms of convergence rate and the computational efficiency for singular surface-surface integrals over coincident (ST), edge adjacent (EA), and vertex adjacent (VA) quadrilaterals.

More specifically, we compute the following weakly singular integral:

$$I^{\text{WS}} = \int_{E_P} \int_{E_Q} G(\mathbf{r}, \mathbf{r}') dS' dS.\tag{2.123}$$

Here $G(\mathbf{r}, \mathbf{r}') = \frac{e^{-ik|\mathbf{r}-\mathbf{r}'|}}{4\pi|\mathbf{r}-\mathbf{r}'|}$ is the free-space Green function and E_P and E_Q are observation and source quadrilateral elements. As reference, we use the results obtained

by the method presented herein (dubbed DIRECTFN-quad) with a high order of Gaussian quadrature for all four one-dimensional integrations, i.e., $N_1 = N_2 = N_3 = N_4 = 25$. We compare the convergence of the novel algorithms with the original DIRECTFN method (dubbed DIRECTFN-tri) [125], applied to the combination of coincident, edge-adjacent or vertex-adjacent triangles obtained by splitting accordingly the quadrilaterals E_P and E_Q . The singular integral (2.123) is computed for all possible configurations, i.e. $E_P \equiv Q_1$ and $E_Q \equiv Q_1, Q_2, Q_3$ for ST, EA and VA elements, respectively (See the inset at Fig. 2-9). All the squares Q_i have the sides with the length $d = 0.1\lambda$, where λ is the wavelength associated to the operating frequency. The relative errors, defined as

$$\varepsilon = \left\| \frac{\|I - I_{\text{ref}}\|_2}{\|I_{\text{ref}}\|_2} + \epsilon \right\|_2, \quad (2.124)$$

(with $\|\cdot\|_2$ being the 2-norm and ϵ the machine epsilon) are presented in Fig. 2-9, from which the exponential convergence with respect to the integration order can be clearly observed. This behavior suggests that the proposed series of transformations and the reordering of the integrations lead to sufficiently smooth kernels. Moreover, the presented algorithm appears to converge substantially faster in the coincident and edge-adjacent cases. Next, we compare the computational efficiency of the proposed scheme with the original DIRECTFN method for the same example. As evinced by the results depicted in Fig. 2-10, the proposed algorithm is significantly more efficient for the most challenging case, i.e. the coincident elements.

The example with strongly singular integrals can be found in the Appendix A. In addition, we would like to note that the proposed scheme is not restricted to the case of piecewise constant basis functions and flat square elements, which are the case in the VIE method exploited in this thesis. Hence, the additional numerical

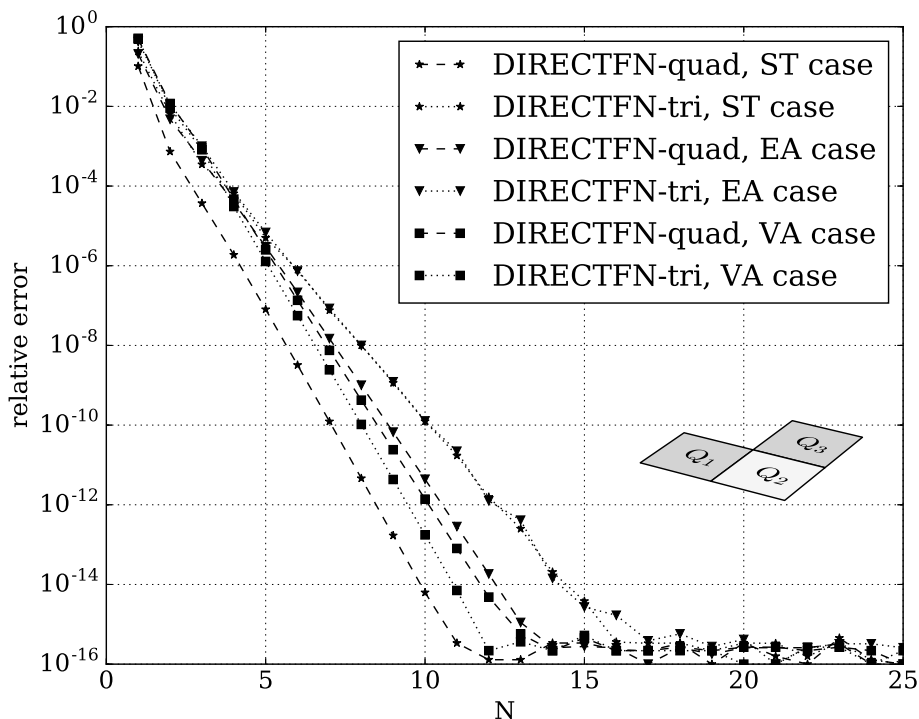


Figure 2-9: Relative error in computing the singular integrals (2.123) as a function of the order of the 1-D Gaussian quadrature rules, DIRECTFN-quad comparison with DIRECTFN-tri.

examples with first-order vector basis functions [126, 117], non-squared elongated quadrilaterals, and curvilinear elements are also presented in the Appendix A..

2.6 FFT-based solver

The direct solution of linear systems, arising in VIE formulations, involves the inversion of huge matrices. Hence, using iterative solvers is the natural choice to tackle realistic problems. In this thesis, we use the generalized minimum residual (GMRES)

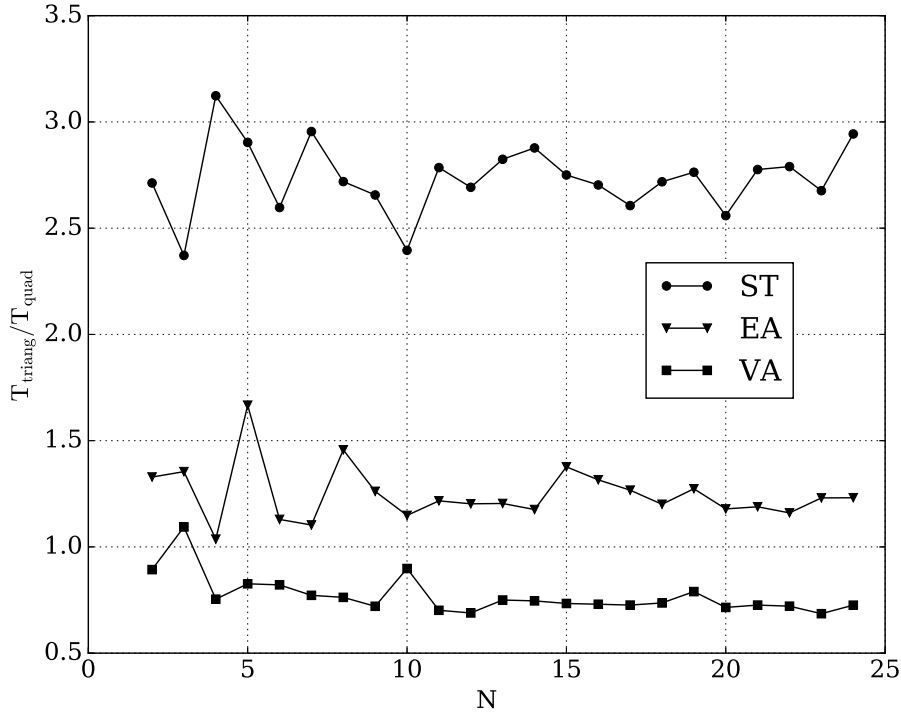


Figure 2-10: Relative CPU times of the proposed scheme with respect to the original DIRECTFN as a function of the order of the 1-D Gaussian quadrature rules.

method for the dense non-symmetrical linear systems (2.23) or (2.28) in the case of non-magnetic material. The bottleneck of any iterative solver is the matrix-vector product that needs to be computed at each iteration and takes $\mathcal{O}(N^2)$ time in a naive implementation, where N is the total number of unknowns. Moreover, the explicit storage of the system matrix is expensive, requiring $\mathcal{O}(N^2)$ memory. However, let us note again, that the discretized version of the full JM-VIE formulation (2.10), we

exploit in this thesis, looks as follows:

$$\left(\mathbf{I} - \begin{pmatrix} \mathbf{M}_\epsilon \mathbf{N} & -c_\epsilon \mathbf{M}_\epsilon \mathbf{K} \\ c_m \mathbf{M}_\mu \mathbf{K} & \mathbf{M}_\mu \mathbf{N} \end{pmatrix} \right) \cdot \begin{pmatrix} \mathbf{w}_e \\ \mathbf{w}_m \end{pmatrix} = \begin{pmatrix} c_e \mathbf{M}_\epsilon \mathbf{e}_{\text{inc}} \\ c_m \mathbf{M}_\mu \mathbf{h}_{\text{inc}} \end{pmatrix}. \quad (2.125)$$

For simplicity, consider the reduced form of (2.125), corresponding to the absence of magnetic conductivity:

$$(\mathbf{I} - \mathbf{M}_\epsilon \mathbf{N}) \mathbf{w}_e = c_e \mathbf{M}_\epsilon \mathbf{e}_{\text{inc}}. \quad (2.126)$$

Without losing the generality, all the successive explanations are valid for the full system as well. Note that we have assumed that both the material properties and incident field piecewise constant functions on the voxel grid. The discrete system (2.126) has the following form:

$$\left[\mathbf{I} - \begin{pmatrix} \mathbf{M}^x & & \\ & \mathbf{M}^y & \\ & & \mathbf{M}^z \end{pmatrix} \begin{pmatrix} \mathbf{N}^{xx} & \mathbf{N}^{xy} & \mathbf{N}^{xz} \\ \mathbf{N}^{xy} & \mathbf{N}^{yy} & \mathbf{N}^{yz} \\ \mathbf{N}^{xz} & \mathbf{N}^{yz} & \mathbf{N}^{zz} \end{pmatrix} \right] \begin{pmatrix} \mathbf{w}^x \\ \mathbf{w}^y \\ \mathbf{w}^z \end{pmatrix} = j\omega\epsilon_0 \begin{pmatrix} \mathbf{M}^x \mathbf{e}_{\text{inc}}^x \\ \mathbf{M}^y \mathbf{e}_{\text{inc}}^y \\ \mathbf{M}^z \mathbf{e}_{\text{inc}}^z \end{pmatrix}. \quad (2.127)$$

Here the blocks \mathbf{M}^x , \mathbf{M}^y , \mathbf{M}^z are diagonal. Since we are using piece-wise constant basis functions on a voxelized grid, the translation invariance of Green function leads to the fact that each of the blocks $\mathbf{N}^{\alpha\beta}$ has block-Toeplitz Toeplitz-block (BTTB)

structure on three levels, corresponding to the three physical dimensions of the problem. (See [29] for more details). Note the symmetry in these blocks, i.e., only six of them are unique. Further, each of these blocks is either symmetric or anti-symmetric. This combined with their BTTB structure allows them each to be defined by a single row. Hence the storage cost for the dense operator matrix \mathbf{N} is only $\mathcal{O}(6N)$, where N is the number of voxels (The same holds for \mathbf{K} matrix). Every $N_x \times N_y \times N_z$ BTTB block $\mathbf{N}^{\alpha\beta}$, $\alpha, \beta = x, y, z$, can be embedded into $2N_x \times 2N_y \times 2N_z$ block-circulant with circulant blocks (BCCB) matrix $\mathcal{C}^{\alpha\beta}$, then its multiplication with a column vector \mathbf{J} can be produced via well-known procedure [127]:

$$\mathcal{C} \cdot \mathbf{J} = \text{ifftn}\{\text{fftn}(\mathcal{C}_1) .* \text{fftn}(\mathbf{J})\}, \quad (2.128)$$

where \mathcal{C} is BCCB matrix, \mathcal{C}_1 corresponds to the elements of the first block of \mathcal{C} , $.*$ is element-wise multiplication, $\text{fftn}\{\cdot\}$ and $\text{ifftn}\{\cdot\}$ mean multidimensional fast Fourier transform and inverse fast Fourier transform, respectively. We further note that the FFT of $\mathcal{C}^{\alpha\beta}$ needs to be computed only once before the iteration process starts. Therefore, the MVP of \mathbf{N} with a vector can be computed in $\mathcal{O}(N \log N)$ with the use of the FFT. Then, since \mathbf{M}_ϵ is diagonal, the total cost of the MVP with $\mathbf{I} - \mathbf{M}_\epsilon \mathbf{N}$ is also $\mathcal{O}(N \log N)$. Therefore the linear system (2.126) can be solved via an iterative method such as GMRES with $\mathcal{O}(pN \log N)$ cost, where p is the number of iterations required to achieve the desired accuracy.

2.7 Preconditioning

A single MVP is fast owing to extremely efficient implementations of the FFT, e.g., [128]. However, if the matrix system (2.126) is ill-conditioned or the eigenvalues

of $(\mathbf{I} - \mathbf{M}_\epsilon \mathbf{N})$ are not clustered near 1, then potentially hundreds or thousands of GMRES iterations, and hence MVPs, are required to solve the system. Thereby creating a huge constant in the aforementioned $\mathcal{O}(N \log N)$ cost. Thus keeping this iteration count small is crucial for the efficiency of the VIE method.

For low-frequency problems with the permittivity values considered here (for Si and SiO₂), only a handful of GMRES iterations are required to solve the integral equation, and so the VIE method employed without a preconditioner is extremely fast. However, as the number of wavelengths fitting across the domain of our problem increases, so does the iteration count.

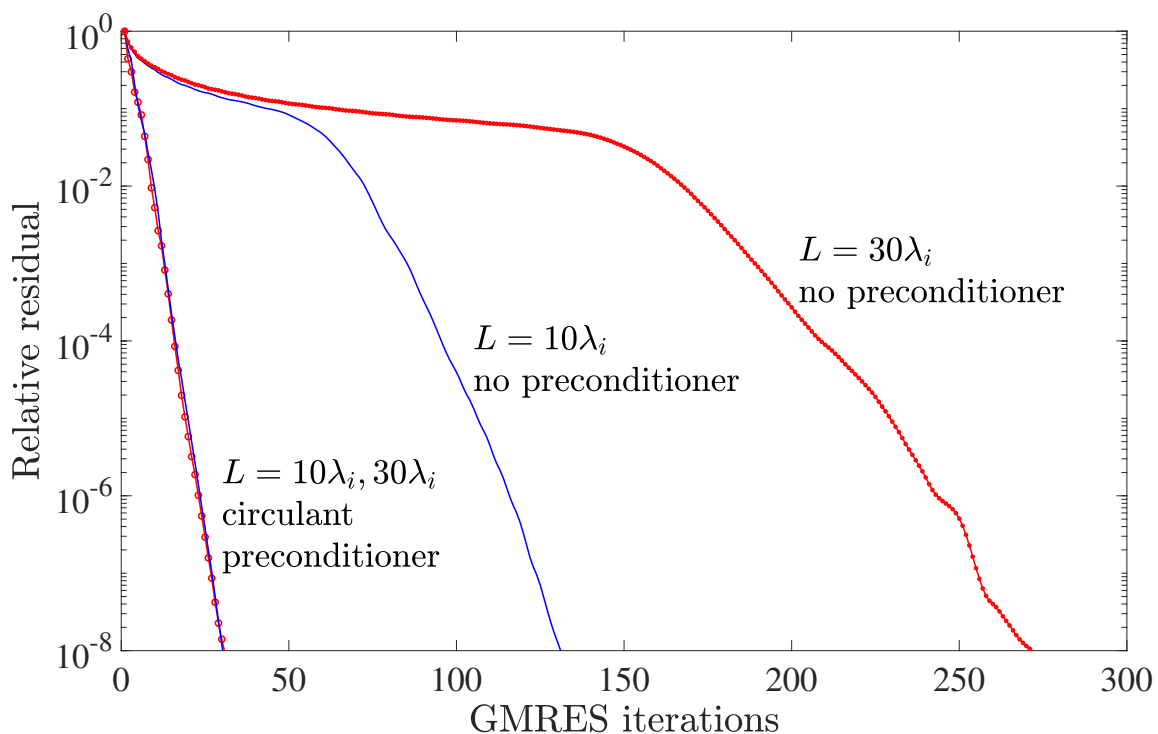


Figure 2-11: Convergence history of GMRES ($\text{tol} = 10^{-8}$) without restarts for a straight waveguide of lengths $10\lambda_i$ and $30\lambda_i$. Observe how, with no preconditioner, the iteration count grows with the waveguide length. The circulant preconditioner, on the other hand, leads to an iteration count independent of the waveguide length.

L_{abs} (λ_{int})	Operator assembly(s)	No prec.		Blocked-circulant prec.			E field calculation(s)	#voxels
		Its.	Solve(s)	Its.	Build(s)	Solve(s)		
10	33	294	339	28	38	45	0.48	388800
15	34	327	495	27	42	48	0.46	437400
20	36	358	651	25	47	53	0.47	486000
25	38	390	774	27	51	59	0.57	534600
30	39	426	894	26	56	64	0.68	583200

Table 2.1: Performance of block-circulant preconditioner for the strip waveguide with $L = 30\lambda_i$, terminated by the absorbers with different lengths.

L (λ_{int})	Operator assembly(s)	No prec.		Blocked-circulant prec.			E field calculation(s)	#voxels
		Its.	Solve(s)	Its.	Build(s)	Solve(s)		
10	25	160	64	28	19	23	0.19	194400
15	27	192	106	27	24	29	0.23	243000
20	28	229	171	28	28	35	0.3	291600
25	30	262	246	27	32	38	0.35	340200
30	33	294	339	28	38	45	0.48	388800

Table 2.2: Performance of block-circulant preconditioner for strip waveguide with different lengths, terminated by the absorber of the length $L_{abs} = 10\lambda_i$.

The problems arising in photonics involve light being channeled by waveguides such as that in Fig. 4-1, with typical dimensions

$$(X, Y, Z) \approx (20\lambda_i \rightarrow 2000\lambda_i, \lambda_i, \lambda_i/2), \quad (2.129)$$

where λ_i is the wavelength within the silicon. That is, the geometry is small in the y - and z -dimensions, but potentially very long (and hence high-frequency) in the x -dimension. For such high-frequency problems, the iteration count of GMRES is not small. In Fig. 2-11 we see the performance of GMRES with tolerance 10^{-8} and without preconditioner for the waveguide in Fig. 4-1 of lengths $10\lambda_i$ and $30\lambda_i$, and with a $10\lambda_i$ absorber. The details of this simulation setup are given in Section 4.1.

Observe the stagnation of GMRES at a relative residual of around 0.1 before it rapidly converges; this is characteristic of high-frequency wave problems. It can be shown [129] that this stagnation period, and hence the iteration count, increases approximately linearly with the waveguide length. This growth quickly leads to infeasibly large iteration counts. Therefore, one must seek to precondition the system (2.126).

A popular preconditioning strategy for Toeplitz systems is to approximate the discrete operator by a circulant matrix. We employed such a strategy for all the computations in Section 4.1 and Section 4.2. Here we give a brief overview of this strategy, which detailed description is provided in [129]. We implemented a modified version of the technique proposed in [130] to create a block-circulant matrix \mathbf{W} which is closest to $(\mathbf{I} - \mathbf{M}_\epsilon \mathbf{N})$ in the Frobenius norm. Circulant matrices are diagonalized by the FFT, hence cheaply inverted. Moreover, the cost of applying the preconditioner is about 2 times of the MVP cost of the unpreconditioned system matrix. (See [129] for details). After constructing and inverting the circulant preconditioner, the following preconditioned system is solved via GMRES:

$$\mathbf{W}^{-1}(\mathbf{I} - \mathbf{M}_\epsilon \mathbf{N})\mathbf{w}_e = \mathbf{W}^{-1}c_e \mathbf{M}_\epsilon \mathbf{w}_e. \quad (2.130)$$

The preconditioned system has a matrix with eigenvalues well-clustered near unity and hence, as can be seen in Fig. 2-11, the convergence of GMRES is greatly improved. To further illustrate the performance of the proposed preconditioning strategy, we present the computation times and iteration counts with and without the preconditioner for the simulation of strip waveguide (See Section 4.1 for the details of the setup). Table 2.2 contains the results of the simulations of the waveguide with increasing length and the fixed length of the absorber $L_{abs} = 10\lambda_i$. We observe

that the preconditioned iteration count is small and does not grow at all with the length of the system. However, assembling and inverting the preconditioner takes about the same amount of time as the iterative solution of the preconditioned system. Nonetheless, the total time remains to be several times less than it takes to solve the non-preconditioned system. Therefore, the VIE method with a block-circulant preconditioner is an extremely effective simulation tool for long nanophotonics structures.

2.8 Fields Computation

The solution of the linear system (2.126) provides the equivalent currents (\mathbf{j}, \mathbf{m}) at the center of each voxel, expressed by the coefficients $(\mathbf{w}_e, \mathbf{w}_m)$. Once we have these, we can compute the electric fields using a discrete version of (2.3) and (2.4):

$$\begin{aligned}\mathbf{e} &= \mathbf{e}_{\text{inc}} + \frac{1}{c_e}(\mathbf{N} - \mathbf{I})\mathbf{w}_e - \mathbf{K}\mathbf{w}_m, \\ \mathbf{h} &= \mathbf{h}_{\text{inc}} + \mathbf{K}\mathbf{w}_e + \frac{1}{c_m}(\mathbf{N} - \mathbf{I})\mathbf{w}_m.\end{aligned}\tag{2.131}$$

Again, to accelerate the multiplication of vectors by the \mathbf{N} and \mathbf{K} operators, we exploit the FFT-based technique, described previously. Hence, the electric (or magnetic) field at the center of each voxel can be computed with $\mathcal{O}(N \log N)$ cost.

2.9 Summary of the Numerical Method

Now we would like to briefly recall all the stages of the described VIE method to help the reader to grasp it in a logically connected form. The key steps of the proposed approach are the following:

1. The input parameters, consisting of the geometry and material properties of the isotropic object (2.1)-(2.2) and the excitation electric and magnetic fields are defined.
2. The system of 2nd kind integral equations, connecting the equivalent currents with the incident fields, is formulated (2.4) (or (2.13)).
3. This system is discretized using the Galerkin method of moments with the piece-wise constant basis functions on a voxelized grid (2.18) (or (2.28)). The incident fields and the material properties are approximated by piece-wise constant functions as well.
4. The obtained discrete linear system is solved iteratively.
5. The electromagnetic fields are calculated from the obtained equivalent currents using (2.131).

Next, we would like to explicate the part related to matrix assembly, preconditioning, and iterative solution. Algorithm 1 presents pseudocode for this implementation, and the steps required are summarized next.

Algorithm 1 Integral Equation Solver

Input: $\omega, \mathbf{E}_{inc}(\mathbf{r}), \mathbf{H}_{inc}(\mathbf{r}), \epsilon_r(\mathbf{r}), \mu_r(\mathbf{r})$

Define resolution. Discretize domain.

Construct right-hand side ▷ Eq. (2.22)

Construct \mathbf{N} and \mathbf{K} operators. ▷ Algorithm 1

Construct block-circulant operators from \mathbf{N} and \mathbf{K} . ▷ See [29] for details

Construct preconditioner. Invert preconditioner. ▷ See [129] for details

Solve (2.23) for $\mathbf{w}_e, \mathbf{w}_m$

Compute $\mathbf{E}_{tot}, \mathbf{H}_{tot}$ ▷ Eq. (2.131)

Output: $\mathbf{E}_{tot}, \mathbf{H}_{tot}$

1. *"offline" stage*

A. Assembling the discrete \mathbf{N} and \mathbf{K} operators for a given discretization and frequency.

- The operators are constructed by simply fixing the basis function (e.g. for the first voxel $j = 1$) and sweeping the testing function over all voxels of the solution domain, as described in Algorithm 2. Note that we only need to assemble and store the unique elements of the complete matrix.
- The volume-volume integrals in Galerkin inner products are reduced to the series of surface-surface integrals over the faces of voxels.
- The non-singular surface-surface integrals are evaluated using 2D Gaussian quadratures, and the singular ones are evaluated using the novel DIRECTFN-quad method proposed herein.

B. Constructing and inverting the circulant preconditioner.

- Circulant matrices are diagonalized by the FFT, hence cheaply inverted.
- The MVP cost of the preconditioner is close to the MVP cost of the unpreconditioned system matrix.

2. *"online" stage*

Solving the linear system with the iterative solver.

- The GMRES solver is used
- The FFT-accelerated MVP is performed with $\mathcal{O}(N \log N)$ cost.
- Using the preconditioner, the iteration count is independent of the waveguide length.

3. *post-processing*

Calculating the fields from the solution of the system.

- The electric and magnetic fields are computed from the equivalent currents with $\mathcal{O}(N \log N)$ cost (2.131).

Algorithm 2 Pseudocode for generating the \mathbf{N} operator.

```

j = 1                                     ▷ Fix the basis function
for i = 1 : N do                         ▷ N = Nx × Ny × Nz is the number of voxels
    Compute Nijkl                             ▷ Eq. (2.37)
    Compute Nijαβ                             ▷ Eq. (2.36)
    Construct Ni-j                             ▷ Eq. (2.35)
end for

```

2.10 Numerical Results and Error Analysis

Mie theory [131, 132, 133, 134] provides an analytical solution for the scattered and interior fields by a lossy dielectric Mie sphere that is illuminated by an incident x-polarized z-propagating plane wave, as depicted in Fig. 2-12. In this section, the electromagnetic field inside the Mie sphere is computed by solving the discretized version of the J-VIE formulation (2.28) and the numerical results are compared to analytical solutions. The spherical shape is represented using the staircase approximation, as shown in Fig. 2-12(b). The radius of the sphere is $1\lambda_i$, where λ_i is the wavelength in the sphere medium. The center of the sphere is at the origin. The relative permittivities of the sphere and exterior medium are $\epsilon_r = 5.7861 - j\epsilon_r''$ and 1, respectively. The relative permeability of both the media is 1. The sphere is illuminated by a plane wave with a free-space wavelength $\lambda_i = 1073 \text{ nm}$, which corresponds to the interior wavelength $\lambda_i \approx 446 \text{ nm}$. First, we have considered the scattering by the spheres

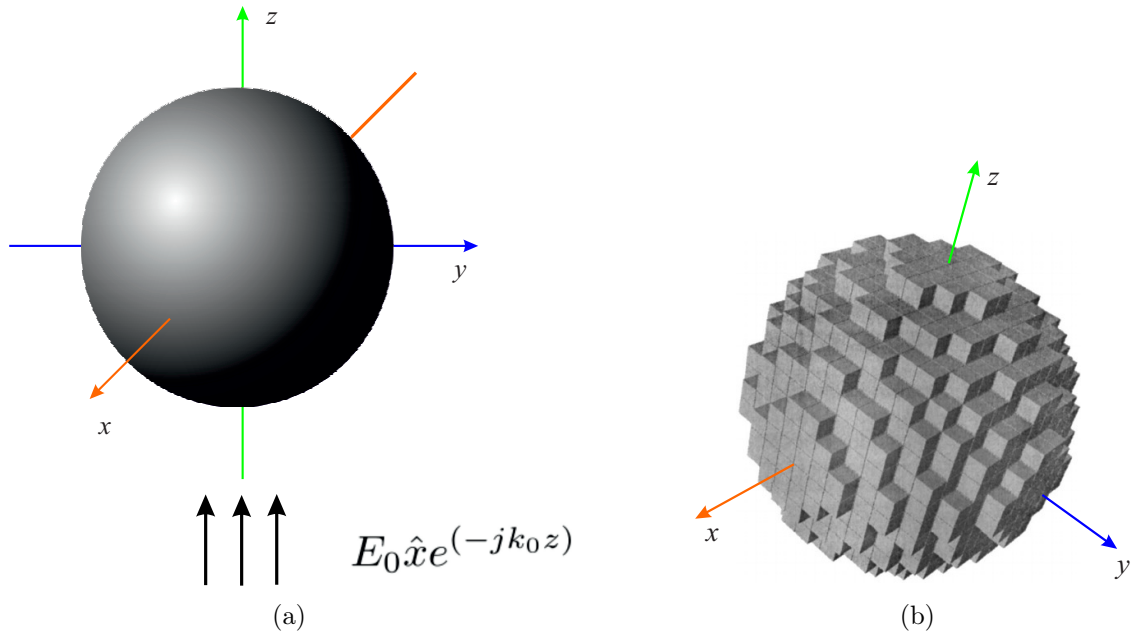


Figure 2-12: (a) A Mie sphere illuminated by a plane wave; (b) a discretized Mie sphere.

with three different electric conductivities: $\sigma_E = 0 \text{ S/m}$, 100 S/m and 1000 S/m , corresponding to the imaginary part of relative permittivity of the sphere material $\epsilon_r'' = 0, 0.006$ and 0.064 .

Figs. 2-13–2-15 show different components of interior electric field along the x , y and z axes. We can observe that refining the mesh the solution goes closer to the analytical one. It should be noted that deviation from the analytical solution is caused not only by the error of the numerical method but also by inaccurate staircase approximation of the geometry.

Next, the convergence rate of the interior fields calculated for the spheres of conductivities 0 S/m , 100 S/m and 1000 S/m is examined in Fig. 2-16 by showing numerical error versus the side length of the voxels h . The maximum relative error

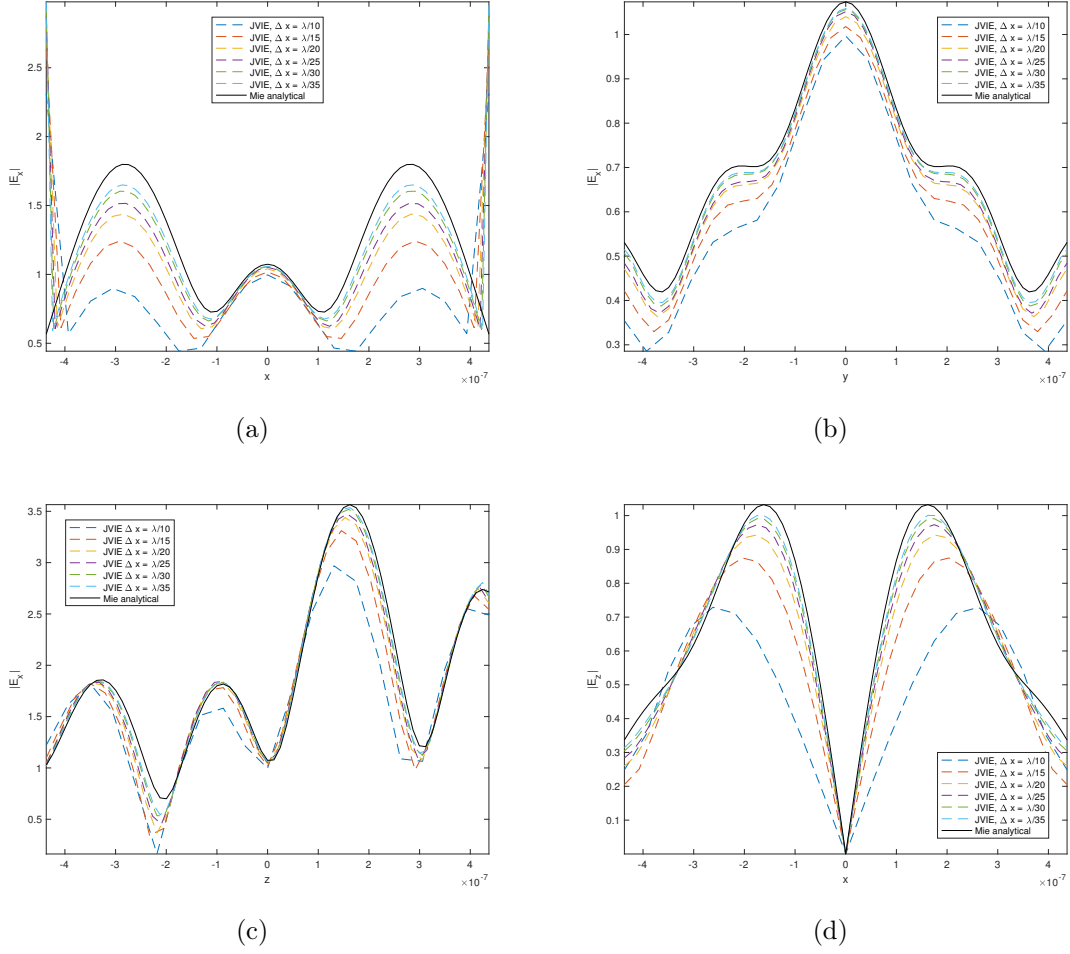


Figure 2-13: The components of interior electric field inside the Mie sphere, $\sigma_E = 0$ S/m.

of the interior electric fields, defined as

$$\text{err}_{\max} = \max \left(\frac{\|\mathbf{E} - \mathbf{E}_{\text{Mie}}\|_2}{\|\mathbf{E}_{\text{Mie}}\|_2} \right) \quad (2.132)$$

is measured. The field is observed along the x-axis and the Mie analytical solution is used as a reference. The convergence rate appears to be $\mathcal{O}(h)$ due to numerical inac-

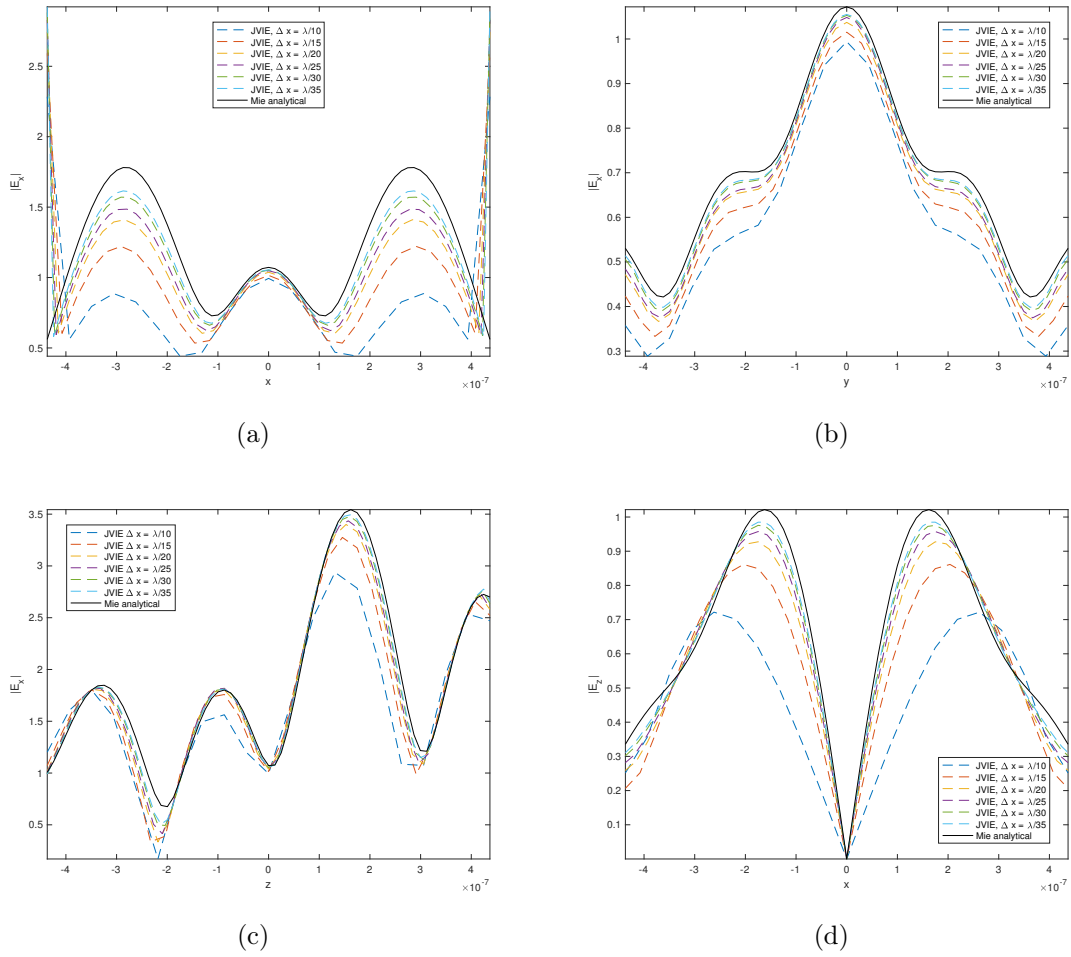


Figure 2-14: The components of interior electric field inside the Mie sphere, $\sigma_E = 100 \text{ S/m}$.

curacies originating from the staircase approximation of a sphere, when discretized with voxels [135].

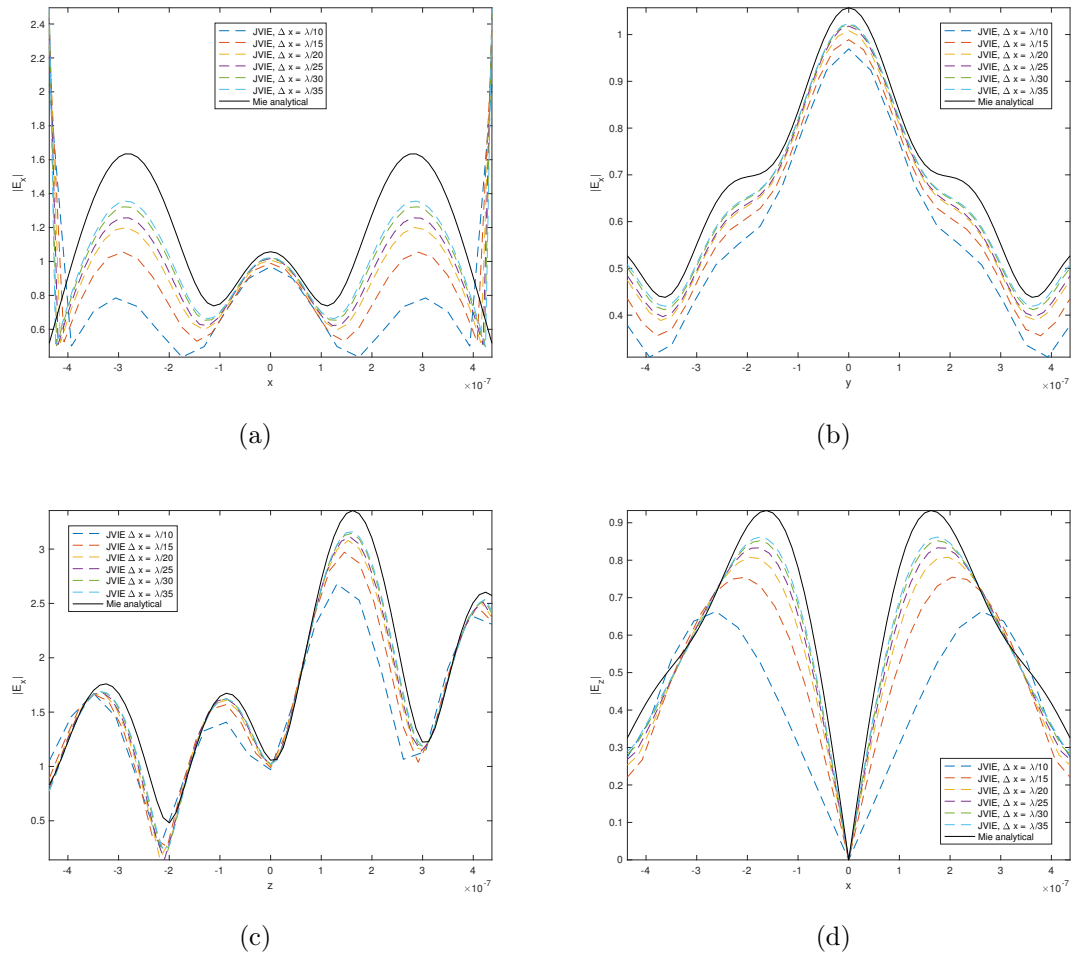


Figure 2-15: The components of interior electric field inside the Mie sphere, $\sigma_E = 1000 \text{ S/m}$.

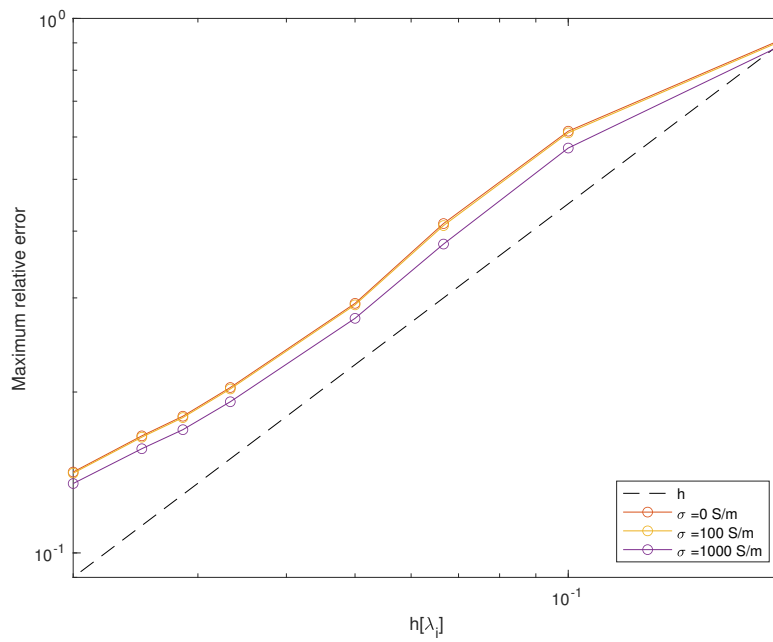


Figure 2-16: Relative error of interior electric fields observed along the x-axis with respect to resolution.

Chapter 3

Absorbers and Reflections

In this chapter, we describe an *adiabatic absorber* technique for terminating optical waveguides with the volume integral equation method, which otherwise has difficulties with waveguides extending to infinity. In order to attenuate waves reflected from truncated waveguides, we append conductive regions to the terminations. The transition between the non-absorbing and absorbing regions will generate reflections that can be minimized by making the transition as smooth as possible. We provide an estimation of the two types of reflections generated by the absorber, namely, the round-trip and transition reflection. We derive the asymptotic power-law behavior of transition reflections as a function of the length of the absorber and demonstrate that the power law is determined by the smoothness of the transition. In addition, we evaluate the effect of the group velocity on the transition reflection.

In the following, we define the conductivity profile as

$$\sigma(x) = \begin{cases} 0, & x < 0, \\ \sigma_0 s(x/L), & 0 \leq x \leq L, \end{cases} \quad (3.1)$$

where $x = 0$ is the beginning of the absorber of length L . Observe that we have introduced a scaled coordinate $u = x/L \in [0, 1]$ for ease of presentation later on. Note further that σ can represent either of the electric or magnetic conductivities, σ_E, σ_M . In this thesis, we consider the first four monomials as our candidate absorption profiles:

$$s(u) = \begin{cases} 0, & u < 0, \\ u^d, & 0 \leq u \leq 1, \end{cases} \quad (3.2)$$

for $d = 0, 1, 2, 3$.

3.1 Adiabatic absorbers in the EM setting

Here we discuss the two types of adiabatic absorbers. First, we consider the absorber with only *electric* conductivity. Next, we allow the magnetic currents to present in the absorber's material, that is, we include both electric and magnetic conductivities. As we will see, the latter allows for impedance matching and hence superior absorbers, but at the cost of solving for twice as many unknowns.

Consider the simple waveguide setup depicted in Fig. 3-1. Suppose that the waveguide begins at the origin and extends to $x = X$ before the absorbing region begins, and this region terminates at $x = X + L$. Assume that the absorber has the *electric* conductivity $\sigma_E(x)$, then the relative permittivity for $0 \leq x \leq X + L$ has the form:

$$\epsilon_r(x) = \begin{cases} \epsilon'_r, & 0 \leq x \leq X, \\ \epsilon'_r - j \frac{\sigma_E(x)}{\omega \epsilon_0} = \epsilon'_r - j \epsilon''_r, & X < x \leq X + L. \end{cases}, \quad (3.3)$$

where ω is the working frequency and ϵ_0 is the electric constant. That is, the relative permittivity is real inside the waveguide and complex inside the absorber. Consider

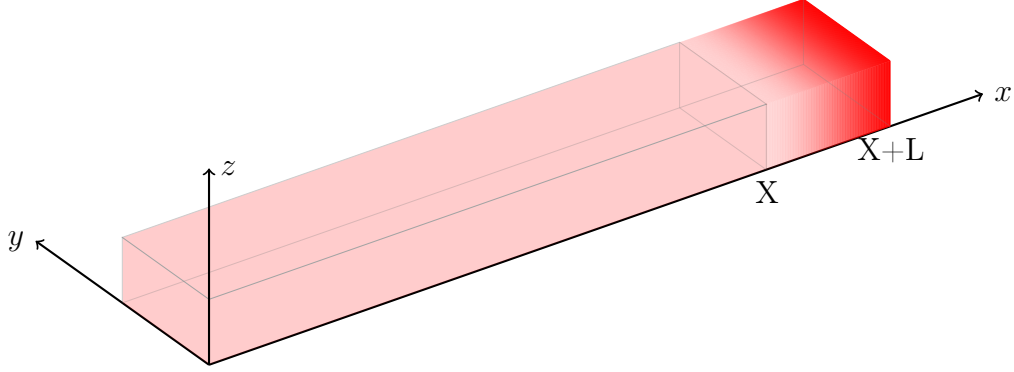


Figure 3-1: The waveguide with the absorber attached. The waveguide begins at the origin and extends to $x = X$ before the absorbing region begins, and this region terminates at $x = X + L$.

the normal-incident wave from the interior region to the absorber region in the yz plane, whose reflection is determined by the mismatch of the intrinsic impedance of the two regions. The intrinsic impedance of the interior region is $Z_i = \sqrt{\frac{\mu_i}{\epsilon_i}}$, where μ_i and ϵ_i are the permittivity and permeability of the interior material, respectively. In our case,

$$Z_i = \sqrt{\frac{\mu_0 \mu'_r}{\epsilon_0 \epsilon'_r}}, \quad (3.4)$$

where μ_0 is the magnetic constant and μ'_r is the relative permeability of the waveguide ($\mu'_r = 1$). The impedance of the conductive region is

$$Z_{abs} = \sqrt{\frac{\mu_0 \mu'_r}{\epsilon_0 \epsilon'_r - j \frac{\sigma_E}{\omega}}}. \quad (3.5)$$

When σ_E increases from zero, the impedances of the two regions start to mismatch, making some of the incident waves reflected back to the interior region without being dissipated in the conductivity region. Moreover, in the case of the absorber with non-constant electric conductivity $\sigma_E = \sigma_E(x)$, the impedance mismatches between

different slices of the absorber produce more reflections. Therefore, with the electric conductivity only, it is difficult to match the impedances between different regions. If we include the *magnetic* conductivity, having that the relative magnetic permeability is

$$\mu_r(x) = \begin{cases} \mu'_r, & 0 \leq x \leq X, \\ \mu'_r - j\mu''_r = \mu'_r - j\frac{\sigma_M(x)}{\omega\mu_0}, & X < x \leq X + L, \end{cases} \quad (3.6)$$

the condition for the impedances to match would be:

$$\sqrt{\frac{\mu_0\mu'_r}{\epsilon_0\epsilon'_r}} = \sqrt{\frac{\mu_0\mu'_r - j\frac{\sigma_M(x)}{\omega}}{\epsilon_0\epsilon'_r - j\frac{\sigma_E(x)}{\omega}}}, \quad (3.7)$$

or equally

$$\frac{\sigma_M(x)}{\sigma_E(x)} = \frac{\mu_0\mu'_r}{\epsilon_0\epsilon'_r}, \quad X < x \leq X + L. \quad (3.8)$$

However, *if we are not including magnetic conductivity*, we have that

$$\mu_r(x) = 1, \quad \text{for all } x. \quad (3.9)$$

In this case, we may simply set $\mathbf{m} = 0$ in (2.10), thereby halving the number of unknowns.

3.2 Round-trip reflection and transition reflection

We consider two types of reflection caused by the adiabatic absorber, namely the round-trip and transition reflections (See Fig. 3-2). The round-trip reflection, R_{rt} , is the reflection due to the wave propagating all the way to the end of the absorber, reflecting off the end, and returning back. Whereas the transition reflection, R_t , is

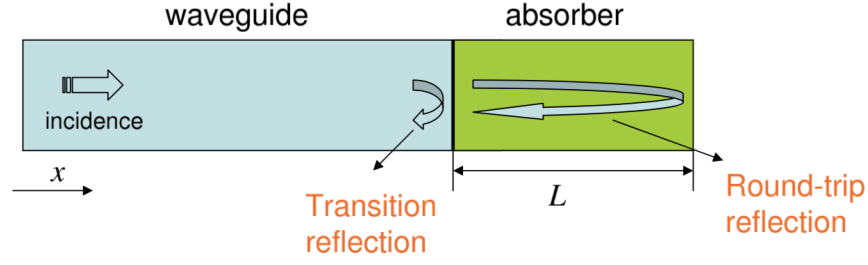


Figure 3-2: Types of the reflections produced by the absorber.

the reflection of the wave at the absorber's interface. We can derive approximate expressions for these two types of reflection. For the round-trip reflection, we can just consider the exponentially decaying wave as it propagates to the end of the absorber and back. For the transition reflection, we appeal to results from coupled-mode theory [136].

Round-trip reflection

In order to calculate the round-trip reflected power, we begin by considering the plane wave travelling in $+x$ -direction in a conductive medium, which can be written in the form:

$$e^{-jk_0 n x}, \quad (3.10)$$

where $k_0 = \omega\sqrt{\epsilon_0\mu_0}$ is the free-space wavenumber, and $n = \sqrt{\epsilon_r\mu_r}$ is the *complex* refractive index of the medium. Recalling that

$$\mu_r = \mu_r' - j\mu_r'' \quad \text{and} \quad \epsilon_r = \epsilon_r' - j\epsilon_r'', \quad (3.11)$$

where

$$\mu_r'' = \frac{\sigma_M}{\omega\mu_0}, \quad \epsilon_r'' = \frac{\sigma_E}{\omega\epsilon_0}, \quad (3.12)$$

the product $\mu_r \epsilon_r$ can then be expanded out as follows

$$\mu_r \epsilon_r = \mu'_r \epsilon'_r - \mu''_r \epsilon''_r - j(\mu''_r \epsilon'_r + \mu'_r \epsilon''_r) \quad (3.13)$$

In the case where we match the impedances by setting $\mu''_r \epsilon'_r = \mu'_r \epsilon''_r$ (see Eq. (3.8)), we have that

$$\mu_r \epsilon_r = \frac{\mu'_r}{\epsilon'_r} (\epsilon'_r - j\epsilon''_r)^2. \quad (3.14)$$

Hence the original plane wave can be written as

$$\exp\left(-jk_0 \sqrt{\frac{\mu'_r}{\epsilon'_r}} (\epsilon'_r - j\epsilon''_r) x\right) = \exp(-jk_0 \sqrt{\mu'_r \epsilon'_r} x) \exp\left(-k_0 \sqrt{\frac{\mu'_r}{\epsilon'_r}} \epsilon''_r x\right), \quad (3.15)$$

so we see that the wave decays as

$$\exp\left(-k_0 \sqrt{\frac{\mu'_r}{\epsilon'_r}} \epsilon''_r x\right) = \exp\left(-\sqrt{\frac{\mu_0}{\epsilon_0}} \frac{\sigma_E}{\sqrt{\epsilon'_r}} x\right), \quad (3.16)$$

where we have also made use of the identity $k_0 = \omega \sqrt{\mu_0 \epsilon_0}$. The round-trip reflection R_{rt} is proportional to the intensity of the wave which is returned back to the waveguide and can be shown to take the form

$$R_{\text{rt}} \sim \exp\left(-D \eta_x \sqrt{\frac{\mu_0}{\epsilon_0}} \frac{1}{\sqrt{\epsilon'_r}} \int_0^L \sigma_E(x) dx\right), \quad (3.17)$$

where $0 \leq \eta_x \leq 1$. For a plane wave propagating purely in the $+x$ -direction, $\eta_x = 1$. When the impedance is matched, we have that $D = 4$; this comes from the fact that the wave travels a distance $2L$, then this is squared to obtain the reflected power. When the impedance is not matched, it can be shown that $D = 2$. The factor of two difference can be attributed to the presence of two attenuating mechanisms in the

matched impedance case, namely the decay due to both the magnetic and electric conductivities, whereas there is only the electric conductivity in the unmatched case. Using $\sigma_E(x) = \sigma_0 s(x/L)$ and making the change of variables $u = x/L$ leads to the following form of (3.17):

$$R_{\text{rt}} \sim \exp \left(-D\eta_x \sqrt{\frac{\mu_0}{\epsilon_0 \epsilon'_r}} L \sigma_0 \int_0^1 s(u) du \right). \quad (3.18)$$

For the monomial absorption profiles (3.2) under consideration in this thesis, this simplifies to

$$R_{\text{rt}} \sim \exp \left(-\frac{DL\eta_x \sqrt{\frac{\mu_0}{\epsilon_0 \epsilon'_r}} \sigma_0}{d+1} \right), \quad (3.19)$$

where d is the index of power of the monomial profile. Now we can choose σ_0 such that we obtain a desired round-trip reflection R_{rt} via the following formula

$$\sigma_0 = -\frac{(d+1) \ln(R_{\text{rt}})}{DL\eta_x} \sqrt{\frac{\epsilon_0 \epsilon'_r}{\mu_0}}. \quad (3.20)$$

For a propagating mode, we expect $\eta_x < 1$ to be the ratio of the propagation constant to the interior wavenumber, but we do not in general know η_x a priori. We further obtain the approximate value of η_x in our setup via calculating numerically the field decay rate inside the absorber of constant electric conductivity, and fitting the decay dependence from σ_E .

Transition reflection

An effective way to analyze the propagation of waves along a waveguide with slowly varying properties (in this case, the conductivity) is via *coupled-mode theory* (CMT). Here we quote the appropriate results from [136] where the details can be found in

full. For a concise summary of the pertinent details of CMT and the results of [136], the reader is referred to [64]. It is shown in [136] that in the limit of slow variation in conductivity (equivalently, the large L limit), the amplitude c_r of a reflected mode has the asymptotic form

$$c_r(L) = s^{(d)}(0^+) \frac{M(0^+)}{\Delta\beta(0^+)} [-jL\Delta\beta(0^+)]^{-d} + \mathcal{O}(L^{-(d+1)}), \quad (3.21)$$

where $s^{(d)}(0^+)$ is the first non-zero derivative of the absorption profile $s(u)$ evaluated at $u = \frac{x-X}{L} = 0^+$, $\Delta\beta = \beta_i - \beta_r \neq 0$ is the difference between the propagation constants of the incident and reflected modes, and M is a coupling coefficient between the incident and reflected modes, which depends on the field spatial pattern, but is a smooth function of u [136, 64]. From Eq. (3.21) it follows that for uniform structures, the transition reflection $R_t(L) \sim |c_r|^2$ scales as $|M|^2/L^{2d} = L^{-2(d+1)}$. That is,

$$R_t = \mathcal{O}(L^{-2(d+1)}), \quad \text{as } L \rightarrow \infty. \quad (3.22)$$

This is confirmed by the numerical results given in the next chapter.

The situation is more complicated in the case of periodic structures where the phenomenon of slow light occurs near and in a band gap. In such scenarios, while approaching a flat band edge, we have that $\Delta\beta = \beta_i - \beta_r = 2(\beta - \frac{\pi}{\Lambda}) \sim v_g$ [136, 64], where Λ is the period of the structure and v_g is the group velocity. Also, the coupling coefficient M is proportional to $1/v_g$ [136, 64], therefore we have that the transition reflection scales as

$$R_t \sim |c_r|^2 = \mathcal{O}(v_g^{-2(d+2)}), \quad \text{for small } v_g, \quad (3.23)$$

for periodic structures. ‘‘Slow light’’ corresponds to small v_g , hence we anticipate

the need for much longer absorbers in order for the $\mathcal{O}(L^{-2(d+1)})$ decay of (3.22) to overcome this unfavorable scaling when operating close to a band edge. Such a periodic structure is the Bragg grating considered in Section 4.2. There we observe in practice this predicted worsening in the performance of adiabatic absorbers.

Chapter 4

Numerical Results of Absorbers

In this chapter, we demonstrate the performance of the proposed algorithms via numerical experiments on different photonic devices. We show that the asymptotic results for adiabatic absorbers discussed in the previous chapter are achieved in our VIE setting. Three different nanophotonics structures are examined: a dielectric strip waveguide (see Fig. 4-1), a Bragg grating waveguide similar to that in [137] (see Fig. 4-16), and a Y-branch splitter. All structures considered consist of a silicon (Si) core surrounded by silicon dioxide (SiO₂). The relative permittivity of Si is wavelength dependent and we assume it obeys the Lorentz model [26, 138], and the relative permittivity of SiO₂ is taken to be 1.444² [26]. Note that in Chapter 2, where the VIE method is described, we assume the exterior medium has unit relative permittivity. In order to make this equivalent to our physical problem, we must scale the relative permittivity of Si and the wavelength of the incident field accordingly (dividing by 1.444² and 1.444, respectively).

Throughout this chapter, we describe the absorber lengths both in terms of the interior wavelength, λ_i , and the exterior wavelength, λ_e . We recall that, contrary to

the DE setting where the absorbing regions must surround the exterior region, in the IE setting we are only required to place the absorbing regions within the dielectric (as illustrated in Fig. 1-1). This means that absorber lengths are described in terms of λ_e in DE methods whereas it seems more natural to describe the lengths in terms of λ_i in the IE setting. We utilize both in this thesis since, although λ_i is more natural, using λ_e enables easy comparison with the more abundant results in the DE setting. Note that the relative refractive index for interchanging between λ_i and λ_e is approximately 2.41 for silicon in silicon dioxide.

In the first set of numerical experiments we consider the simple scenario of the straight uniform waveguide of Fig. 4-1 with an absorber of length L appended to the right end. First of all, to make sure of the convergence of our numerical solution, we calculate the electric field distribution inside the waveguide, terminated by the absorber of the length $L = 4500$ nm, which equals approximately $10\lambda_i(4.15\lambda_e)$, having a quadratic conductivity profile. Using 5 different mesh resolutions, we demonstrate that refining the mesh the solution converges to a certain field distribution. Next, we examine the dependence of field decay rate from the electric conductivity by considering the absorbers with constant conductivities. We show that the numerically calculated decay rate is aligned with the estimation from the previous chapter. We further compare the reflections produced by the absorbers with different conductivity profiles. While keeping the round-trip reflection fixed, we examine the transition reflection dependency on the absorber length. Values of L from 450 nm to 9450 nm in increments of 450 nm are considered; this equates approximately to $1\lambda_i$ ($0.4\lambda_e$) to $20\lambda_i$ ($8.3\lambda_e$). The absorption profiles are the monomials (3.2). For this example, we observe the asymptotic behavior (3.22) of the transition reflection. From these experiments, the absorbers with quadratic conductivity profile appear to be optimal in most scenarios. We proceed by considering the absorber

having both electric and magnetic conductivities. We observe that matching the impedances improves the absorber, however only by a constant factor. Finally, we compare the electric field components, observed in a cross-section of a waveguide with the length $L = 22 \mu\text{m} \approx 50\lambda_i$, terminated with a quadratic absorber of the length $L = 4.4 \mu\text{m} \approx 10\lambda_i$, with the first TE-mode profile, obtained by solving the eigenvalue problem with the finite element solver employed in COMSOL Multiphysics[®] software [139].

Next, we examine the behavior of adiabatic absorbers while terminating an infinitely long periodic channel, which is, in our case, the Bragg grating. First, to demonstrate a typical simulation of the Bragg grating, we obtain the transmission spectrum for the finite grating of $N = 100$ periods. Next, we terminate the grating of $N = 50$ periods by an absorber of the same shape and with length ranging from 1Λ ($0.7\lambda_i/0.3\lambda_e$) to 800Λ ($585\lambda_i/243\lambda_e$), where $\Lambda = 320 \text{ nm}$ is the grating's period. The simulations performed using an absorber of length 900Λ are used to generate the reference solutions. We show that adiabatic absorbers can perform well, when the periodic channel is excited away from a band gap, however near a band gap, where the group velocity goes close to zero, the effectiveness of adiabatic absorbers deteriorates. We note that this is a problem inherent to such absorbers (and other taper transitions [137]), as well as PMLs, and is predicted by theory.

Finally, we examine the performance of absorbers of fixed length and profile to truncate a Y-branch splitter which is an oft-simulated nanophotonics structure [26].

In addition, we introduce the signal-to-noise ratio as an alternative measure of absorber performance and study its dependence on the absorption rate when the absorber length is fixed.

For all simulations performed, we use an iterative GMRES solver with tolerance 10^{-8} to solve the arising discrete system (2.125)-(2.126).

4.1 Dielectric strip waveguide

In this section, we examine the reflections from an adiabatic absorber used to truncate a silicon strip waveguide, as shown in Fig. 4-1. We begin by describing the geometrical setup for these simulations. The waveguide we consider occupies the space

$$0 \leq x \leq 13500 \text{ nm}, \quad 0 \leq y \leq 500 \text{ nm}, \quad 0 \leq z \leq 200 \text{ nm}. \quad (4.1)$$

This size, or similar, for the (y, z) cross-section is a popular choice owing to its support of one dominant TE guided mode in the free-space wavelength range of 1500 nm to 1600 nm. The free-space wavelength of light considered is 1550 nm which equates approximately to a wavelength of $\lambda_i = 446$ nm within the silicon core. Therefore, the length of the waveguide is roughly $30\lambda_i$ ($13\lambda_e$).

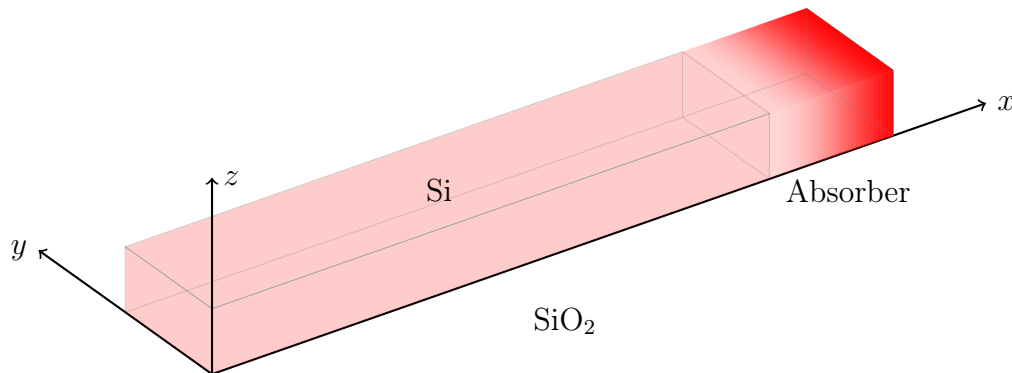


Figure 4-1: Problem setup for a Gaussian beam source within a silicon strip waveguide with one absorber attached. Only one absorber is necessary for this problem since the source has directionality and we anticipate no reflections propagating in the $-x$ -direction. The cladding medium is silicon dioxide.

The waveguide is excited using a Gaussian beam produced by a dipole located in complex space [140]. The real part of the dipole position is inside the waveguide on the center-line, $\lambda_i/4$ from the left end. It can be shown that if the imaginary part of

the x -position of the dipole equals $-bj$, with $b > 0$, it produces a beam propagating in the $+x$ -direction, which is equivalent to that produced by a source distribution on the circular disc of radius b in real-space [141]. In our simulations, we use $b = \lambda_i$, which was found to give a good compromise between directionality and localization. In order for the quasi-TE mode to be established by this excitation, we found that a straight portion of a waveguide of approximately $5\lambda_i/2.1\lambda_e$ is required. In this strip waveguide scenario, we expect all the waves to propagate in the $+x$ -direction, hence we append only one absorber, on the right-hand end of the waveguide. First of all,

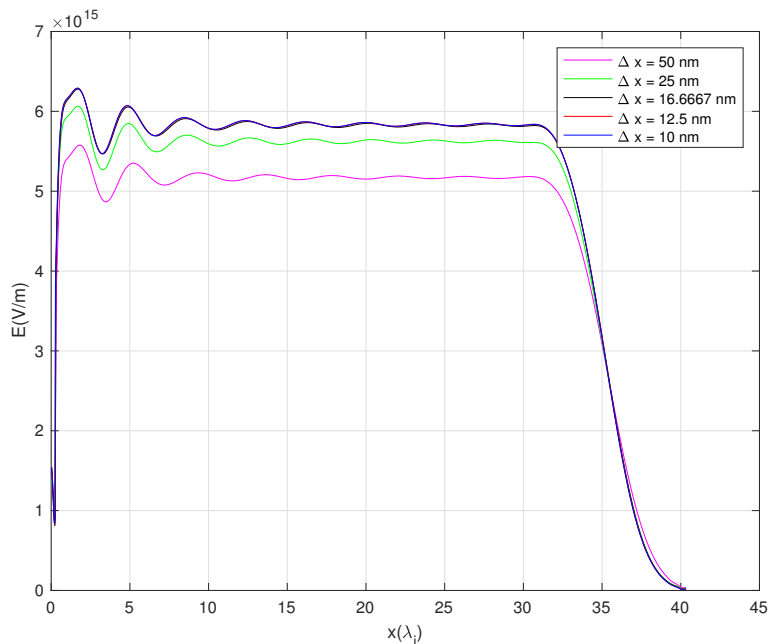


Figure 4-2: The absolute value of y-component of the electric field along the \hat{x} - axis.

to make sure that our numerical solution converges, we compare the fields calculated using different mesh resolution, i.e., we consider the electric field distribution along the three axes: on the center-line of the waveguide along the \hat{x} -axis, and along the \hat{y} - and \hat{z} - axes in the cross-section at the half-length of the waveguide. We use a

quadratic function for electrical conductivity $\sigma_E(x) = \sigma_0(x - x_0)^2/L^2$, where the absorber length L equals 4500 nm, which is approximately $10\lambda_i(4.15\lambda_e)$, and the constant σ_0 was calculated from (3.20) in order to obtain the round-trip reflection $R_{rt} = 10^{-10}$. The results were obtained using the voxels of sizes 50 nm, 25 nm, 50/3 nm, 50/4 nm, and 10 nm. From Figs. 4-2–4-4 one can clearly observe the convergence of the solution to a certain field distribution. In the successive experiments with strip

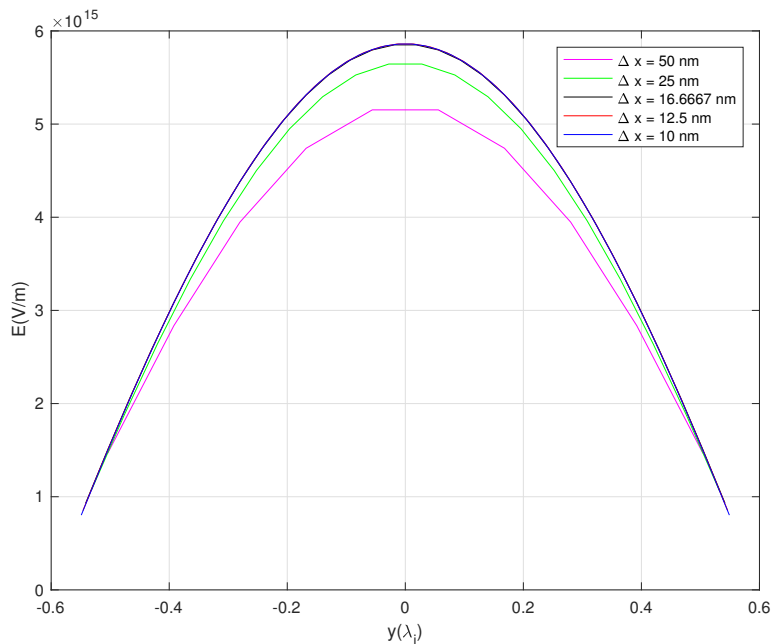


Figure 4-3: The absolute value of y-component of the electric field along the \hat{y} - axis.

waveguides, we use voxels of size 50/3nm since this perfectly divides the dimensions of the structure. Further, this represents approximately 27 voxels per λ_i which is a high enough resolution to ensure accurate simulations [142].

Next, we investigate the effect of using absorbers with different conductivity profiles. In Fig. 4-5 we show the complex magnitudes of the electric field on the center-line of the waveguide along the \hat{x} - axis calculated for the waveguides with

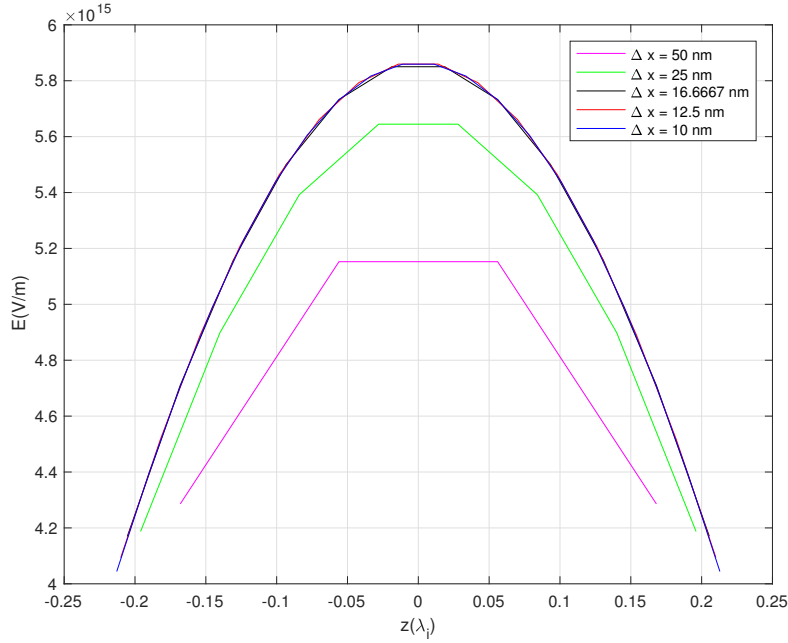
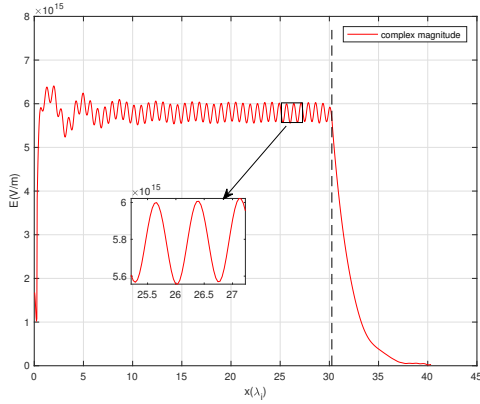


Figure 4-4: The absolute value of y-component of the electric field along the \hat{z} - axis.

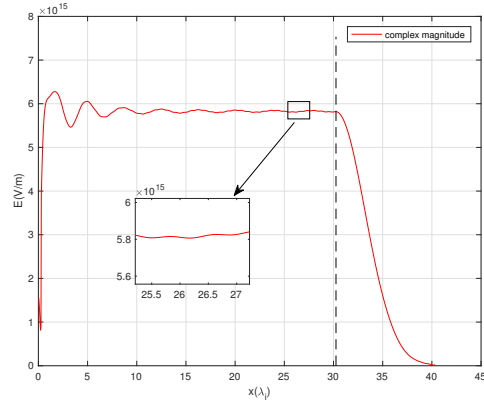
several different absorbers. The absorber is in the region where $x_0 < x < x_0 + L$ in which x_0 is the position of the interface and L is the absorber length. The electric conductivity in this region is given by $\sigma_E(x) = \sigma_0(x - x_0)^d/L^d$, where $d = 0, 1, 2$ for constant, linear and quadratic profiles. As is easily seen in Fig. 4-5, there are substantial reflections when using a constant conductivity, smaller reflections when using a linearly increasing conductivity, and almost no reflections for a quadratically increasing conductivity. We quantify the reflection by use of the standing wave ratio (SWR), the ratio of the maximum field magnitude to the minimum field magnitude in the standing-wave region, evaluated on the waveguide axis. From the SWR, a reflection coefficient is then readily obtained as in a conventional transmission line. The magnitudes of the field reflection coefficients R are listed in Table 4.1.

Conductivity profile	constant	linear	quadratic
SWR	1.0844	1.0070	1.0057
Reflection (dB)	-27.8520	-49.1963	-50.9086

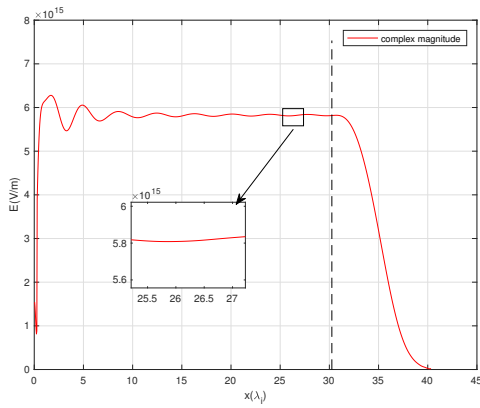
Table 4.1: The standing wave ratio (SWR) and field reflection versus the conductivity distribution of the absorber, whose length is $\sim 10\lambda_i$.



(a) constant conductivity



(b) linear conductivity along x direction



(c) quadratic conductivity along x direction

Figure 4-5: The complex magnitude of the electric field inside a waveguide and absorber. The dashed line indicates the position of the waveguide-absorber interface.

4.1.1 Field Decay Rate

In this section, we examine the exponential decay rate of waves propagating through the absorber region. We demonstrate the relation between the decay rate and the conductivity using an example of an absorber with uniformly distributed electric conductivity. Figure 4-6 shows the complex magnitude of electric field along the

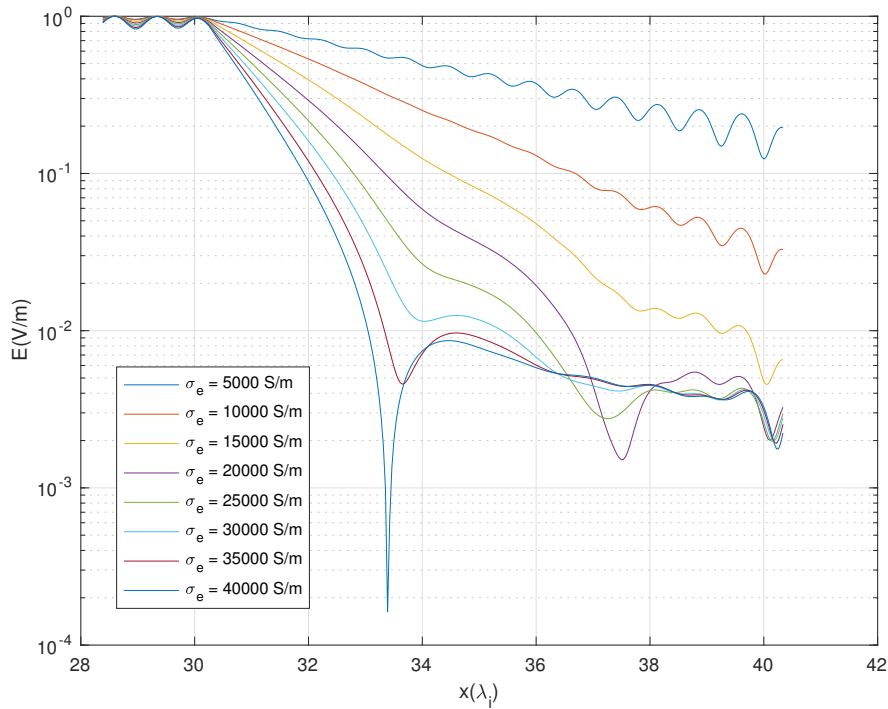


Figure 4-6: The complex magnitude of the electric field along the \hat{x} -axis inside the absorber with uniform conductivity.

\hat{x} -axis inside absorbers with different constant electric conductivities. As expected from (3.16), the field decays exponentially with the distance with a conductivity-dependent rate. It can also be seen that the wave reflects back from the right end, and conceivably these reflections decay as they travel to the left. An approximation

to the rate of exponential decay can be determined by fitting the field plots. The fitted decay rates α for a range of σ_E are shown in Fig. 4-7. One can see for this range of σ_E the decay constant depends linearly from the electric conductivity, which is in agreement with the estimation we obtain earlier: recalling the equations (3.16)

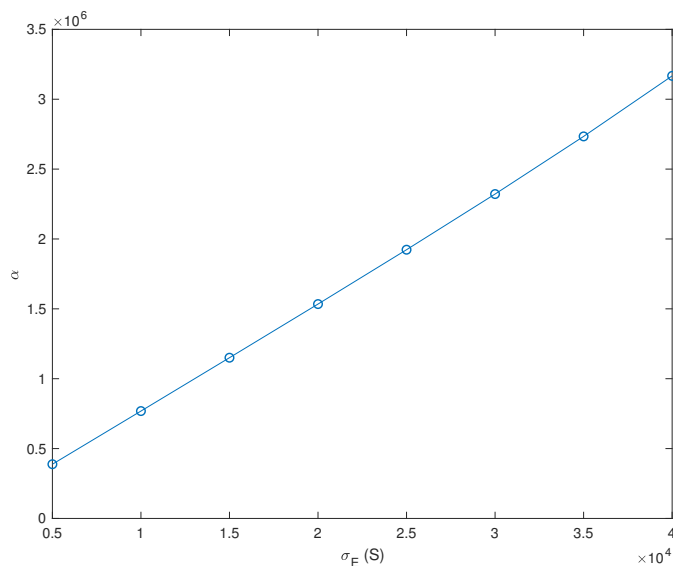


Figure 4-7: The rate of field exponential decay along the propagation direction versus electric conductivity.

and (3.17), the decay constant α is

$$\alpha(\sigma_E) = \eta_x \sqrt{\frac{\mu_0}{\epsilon_0}} \frac{1}{\sqrt{\epsilon_r'}} \sigma_E. \quad (4.2)$$

Fitting the dependency in Fig. 4-7, we obtain $\eta_x \approx 0.5$.

Further analyzing the field decay, one can admit, that for the conductivities higher than $2 \cdot 10^4$ S/m the field decays exponentially near the start of absorber, as expected from however, but after some distance the exponential decay breaks. This can be explained by the presense of coupled radiation. The radiation is generated

by inevitable mismatch between the excitation source and the waveguide modes. The situation is similar to a source radiating in a lossy half-space, in which the dominant field contribution is due to a lateral wave that decays algebraically [143].

4.1.2 Transition reflection length dependency

To measure the transition reflection dependency on the absorber length, we first extract the field along the central axis of the waveguide: $0 \leq x \leq 13500\text{nm}$, $y = 250\text{nm}$, $z = 100\text{nm}$. The field on this axis obtained using the longest absorber ($L = 9450\text{nm}$) is taken as the “exact” solution and denoted \mathbf{E}^∞ . Then the reflection coefficient, which is identified with the transition reflection up to some constant, is calculated as follows

$$\mathbf{R} := \frac{\|\mathbf{E}^\infty - \mathbf{E}^{(L)}\|^2}{\|\mathbf{E}^\infty\|^2}. \quad (4.3)$$

Recall we are considering the reflected power, hence the powers of 2. The norm is the L^2 norm, that is we have that

$$\|\mathbf{E}^\infty - \mathbf{E}^{(L)}\|^2 := \int_0^X |\mathbf{E}^\infty(x) - \mathbf{E}^{(L)}(x)|^2 dx. \quad (4.4)$$

We considered the values of absorbers’ length L from 450 nm to 9450 nm in increments of 450 nm; this equates approximately to $1\lambda_i$ ($0.4\lambda_e$) to $20\lambda_i$ ($8.3\lambda_e$). To focus on the transition reflection, we fix the round-trip reflection to $R_{rt} = 10^{-25}$ by choosing the constant σ_0 appropriately using (3.19). Initially we solve for the electric currents (related to \mathbf{e} via (2.9)) alone, that is, we do not match the impedances of the absorber and the waveguide. The reflection coefficients \mathbf{R} for the first three absorption profiles as functions of L are shown as the lines labeled \mathbf{e} (for electric) in Fig. 4-8. The figure shows that the observed transition reflection agrees with the asymptotic result (3.22)

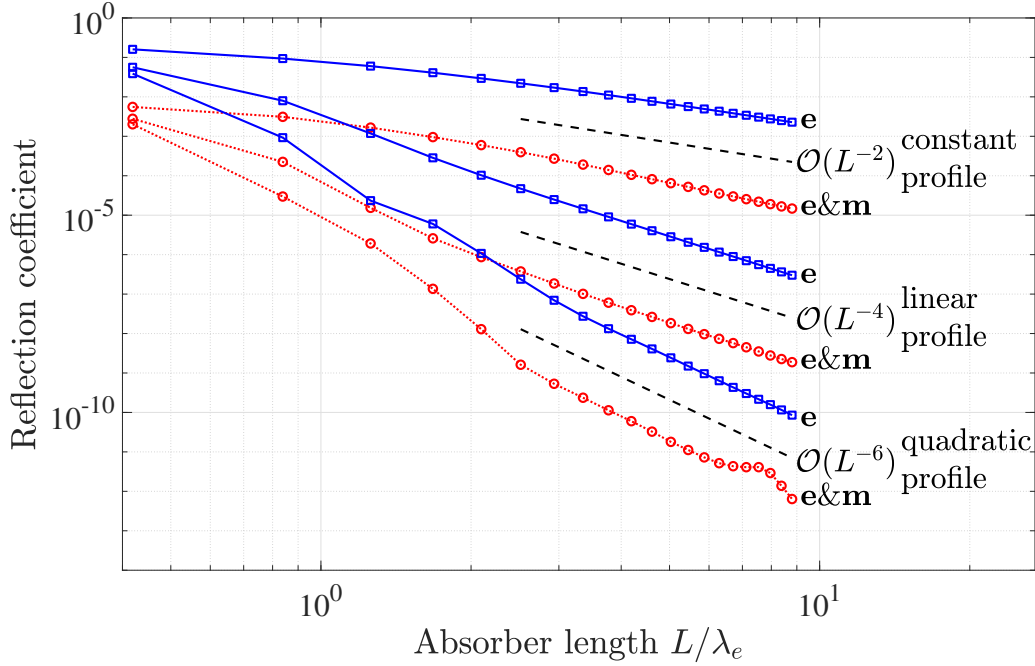


Figure 4-8: Reflection coefficient versus absorber length L for first three monomial absorption profiles when $R_{\text{rt}} = 10^{-25}$. The lines labeled **e** correspond to the case where only the electric field is solved for. The lines labeled **e&m** correspond to the case where both the electric and magnetic fields are solved for, with the impedance matched. Note that this impedance matching reduces the reflection coefficient by approximately a factor of 100. We observe that each of the first three monomials achieves the asymptotic convergence rate of $\mathcal{O}(L^{-2(d+1)})$.

for the first three monomials. The reflection for the cubic profile, as shown in Fig. 4-9, appears not to have reached the asymptotic regime before stagnating at a value of $R \approx 10^{-11}$. In this regime, the quadratic profile produces the smallest transition reflections for absorbers of length less than $3.3\lambda_e$ ($8\lambda_i$). For absorbers of length $3.3\lambda_e$ or more, the cubic profile is superior. In general, we remark that, although increasing the polynomial degree (and hence the smoothness of the transition from waveguide to absorber) improves the asymptotic rate at which the transition reflection diminishes, it also requires ever longer absorbers in order to reach this asymptotic phase.

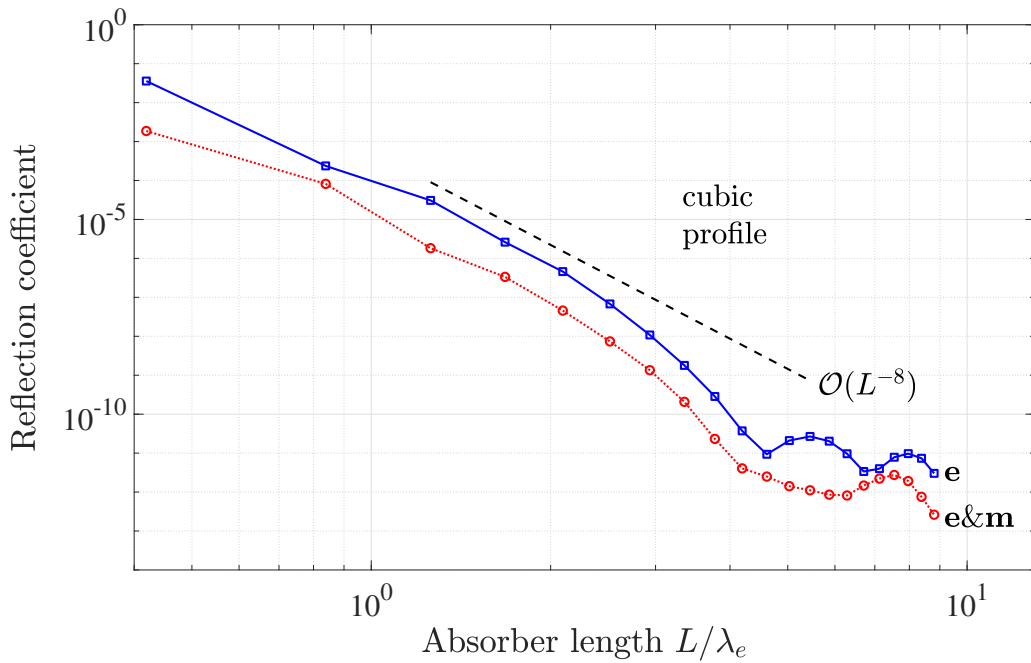


Figure 4-9: Reflection coefficient versus absorber length L for cubic absorption profiles when $R_{rt} = 10^{-25}$. The blue squares correspond to the case where only the electric field is solved for. The red circles correspond to the case where both the electric and magnetic fields are solved for, with the impedance matched. Observe that the convergence is faster than the predicted asymptotic rate, implying the asymptotic range is not achieved for these absorber lengths. In fact, for cubic and higher order profiles, the asymptotic range is not achieved for any of the practical examples considered in this thesis.

4.1.3 Electric and magnetic conductivities

Up to now, we have investigated the adiabatic absorbers with *electric* surface conductivity. Next, it is interesting to observe the improvement in the absorbing layer when magnetic currents are introduced, thus allowing the impedance to be matched (albeit at the cost of doubling the number of unknowns). The lines labeled with **e&m** (for electric and magnetic currents) in Fig. 4-8 are the matched impedance counterparts of the lines labeled **e**. The reflection coefficient is reduced by a factor of

approximately 100, which is good, but not overwhelmingly so, and does not justify the increase in computational cost of solving for the additional magnetic currents.

This reduction factor, however, is not the piece of information we are really interested in. We would like to know by how much we can reduce the absorber length to maintain the same reflection. Suppose we desire $R = 10^{-8}$, which is sufficiently small for practical purposes. The required absorber lengths to achieve this are shown in Table 4.2. Considering $R_{\text{rt}} = 10^{-25}$, we see that, the reduction in required absorber length when going from unmatched impedances to matched impedances diminishes as the monomial degree increases. For $d = 0$, the decrease is thousands of wavelengths, whereas when $d = 3$, the decrease is less than $0.5\lambda_e$ ($1.2\lambda_i$). Curiously, we observe that, depending on which technique is used, either $d = 2$ or $d = 3$ provide the superior absorber. In any case, the small saving in the simulation domain for $d = 2, 3$ does not justify doubling the degrees of freedom.

Monomial degree, d	Absorber length (L/λ_e)			
	$R_{\text{rt}} = 10^{-25}$		$R_{\text{rt}} = 10^{-10}$	
	e	e&m	e	e&m
0	5,400	150	1,900	96
1	20.4	5.8	13	3.7
2	3.9	2.1	3.0	2.0
3	3.0	2.5	2.6	2.5

Table 4.2: Absorber length (in units of number of exterior wavelengths) required to obtain $R = 10^{-8}$. We choose such a value for R since it is sufficiently small for practical purposes. Some of the values for $d = 0, 1$ have been extrapolated from Fig. 4-8 and Fig. 4-10.

A more practical way to reduce the transition reflection, and hence the required size of the absorber, is to reduce the imposed round-trip reflection R_{rt} . Previously, we have fixed the round-trip reflection to a very small value $\sim 10^{-25}$ in order to isolate the effect of the transition reflection. However, in a real application, one is

unlikely to require such low reflections, thus it is reasonable to fix R_{rt} to a larger value, corresponding to a lower σ_0 . Consider $R_{rt} = 10^{-10}$: the corresponding results are shown in Fig. 4-10 and Table 4.2. To obtain $R = 10^{-8}$ with a quadratic profile, say, we require an absorber of length $3\lambda_e$ ($7.1\lambda_i$) for $R_{rt} = 10^{-10}(\mathbf{e})$, compared to $3.9\lambda_e$ ($9.5\lambda_i$) for $R_{rt} = 10^{-25}(\mathbf{e})$, and $2.1\lambda_e$ ($5.1\lambda_i$) for $R_{rt} = 10^{-25}(\mathbf{e\&m})$. The reduction is not quite as large as observed when introducing magnetic currents (about a wavelength less for the quadratic absorber), but it is significant and we do not have to double the number of unknowns.

It is also worth noting that in all our convergence graphs, the reflection coefficient stagnates at some small value. This is due to the difference between the phases of the round-trip reflections contained in $\mathbf{E}^{(L)}$ and \mathbf{E}^∞ , for each L . Therefore, we would anticipate that this small stagnation value should be close to the enforced round-trip reflection. Indeed, this is the case when $R_{rt} = 10^{-10}$ in Fig. 4-10. However, this is not the case when $R_{rt} = 10^{-25}$ in Fig. 4-8. In the latter scenario, this is because the numerical discretization error and iterative solver tolerance are greater than the enforced round-trip reflection.

The next step to optimize the adiabatic absorber is to balance the round-trip and transition reflections for a given length L . This entails enforcing the round-trip reflection to also follow the power law (3.22). This leads to larger values of R_{rt} for smaller L , hence a smaller $\sigma_0 \propto -\ln(R_{rt})$, and thus a smaller transition reflection. Fig. 4-11 shows the result of balancing R_{rt} and R_t for a constant absorption profile. We observe that the reduction in the transition reflection is substantial for small L . For larger L the reduction is less dramatic; this is due to an additional factor of $\ln R_{rt} \sim \ln L$ that now appears in the asymptotic convergence rate. Note further that the line is jagged rather than straight. This is due to the interference of the now similar size round-trip and transition reflections. In Fig. 4-11 are shown the

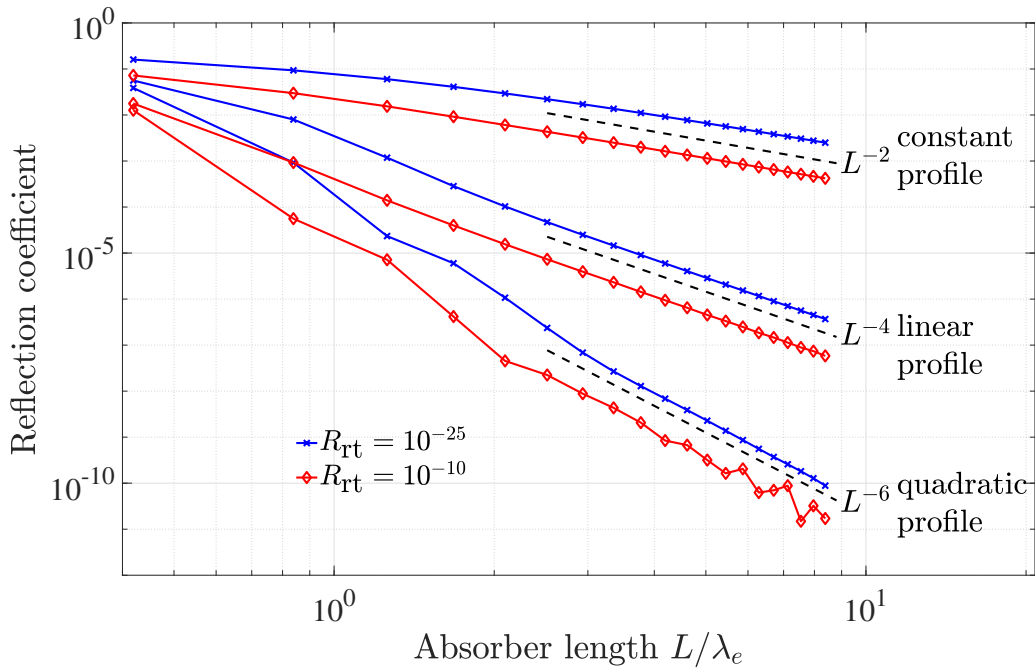


Figure 4-10: Reflection coefficient versus absorber length L for first three monomial absorption profiles for two different round-trip reflections: $R_{\text{rt}} = 10^{-25}$ (blue crosses) and $R_{\text{rt}} = 10^{-10}$ (red diamonds). An order of magnitude reduction in the reflection coefficient is achieved by decreasing the imposed round-trip reflection in this way.

reflection coefficients for the first three monomial profiles. The improvement gained by balancing R_{rt} and R_t appears to reduce as the polynomial degree of the absorption profile is increased. Finally, we note that, although balancing these two reflections gives a reduction in transition reflection, it requires some trial and error in order to choose the optimal constant C_{opt} in the imposed power law for the round-trip reflection $R_t = C_{\text{opt}}L^{-2(d+1)}$. For practical purposes, one would wish to perform such an optimization over all problem parameters such as wavelength and refractive index. This is a non-trivial task and, as can be seen, in this simple scenario yields little gain. However, such optimization may be useful in more complicated cases, such as terminating channels with periodic corrugations.

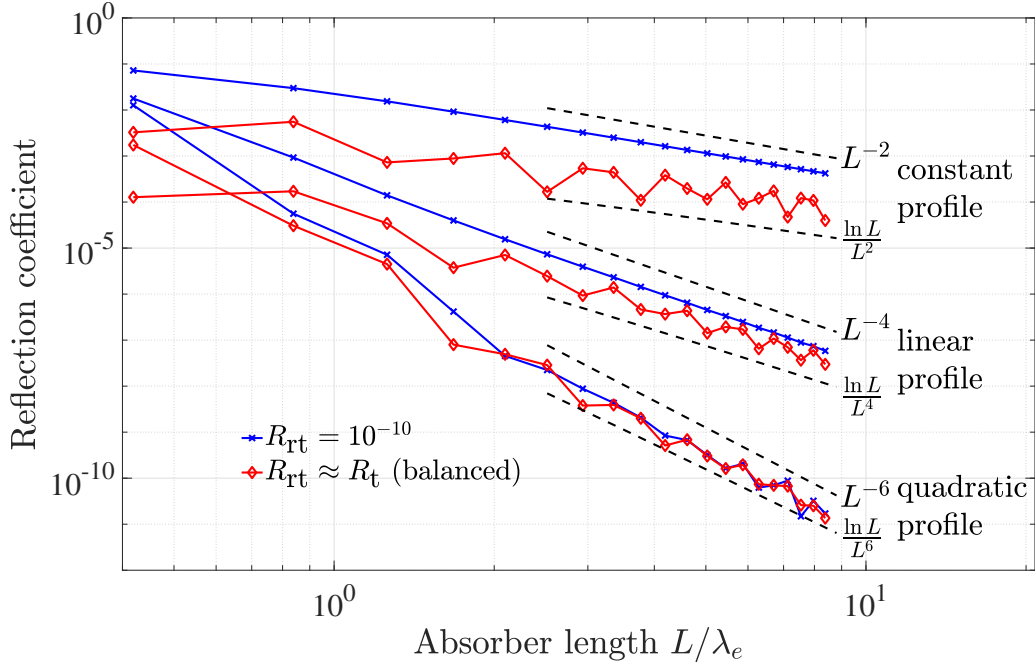


Figure 4-11: Reflection coefficient versus absorber length L for first three monomial profiles for two different round-trip reflections: $R_{\text{rt}} = 10^{-10}$ (blue crosses) and $R_{\text{rt}} = C_{\text{opt}}L^{-2(d+1)}$ (red diamonds). The second case is equivalent to balancing the round-trip reflection with the transition reflection. Observe the improvement achieved; this gain diminishes as the polynomial degree increases.

4.1.4 Comparison with COMSOL Multiphysics[®]

In order to compare our numerical solver with other methods, we have calculated the guided modes for the rectangular silicon waveguide with $500 \text{ nm} \times 220 \text{ nm}$ cross-section in a dioxide cladding, using the COMSOL Multiphysics[®] package [139] to solve the eigenvalue problem. To obtain the propagating modes, COMSOL exploits a finite element method on a triangulated mesh. Fig.4-12 shows the components of the electric field of the lower order mode, scaled by its maximum absolute value, obtained using the mesh with 184861 triangles, at a wavelength 1500 nm. This solution corresponds to the first quasi-TE mode and is in agreement with the example given on

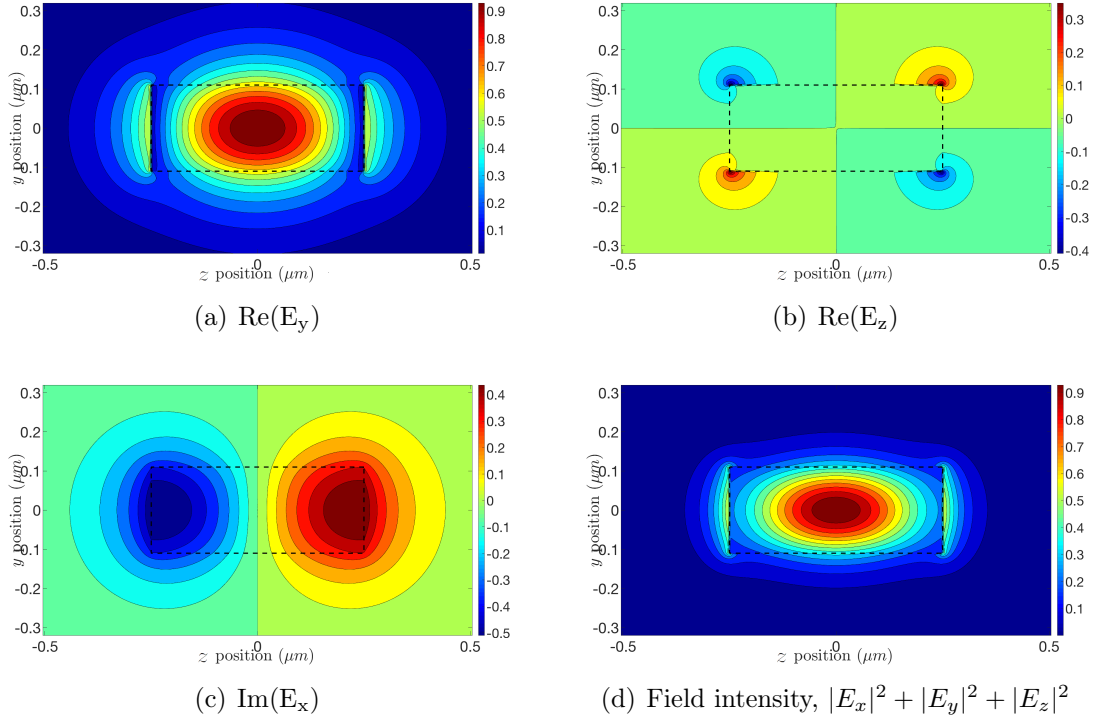


Figure 4-12: TE (first) mode profile of a $500 \text{ nm} \times 220 \text{ nm}$ strip waveguide at 1550 nm wavelength obtained with COMSOL. The three field components in the x, y, z directions are shown.

pp.51-52 of [26]. Next, we perform the JVIE simulation of $500 \text{ nm} \times 220 \text{ nm} \times 22 \mu\text{m}$ waveguide at the same wavelength. The waveguide constitutes approximately $50\lambda_i$, where λ_i is the wavelength inside the silicon core. We terminated the waveguide with a quadratic absorber of length $4.4\mu\text{m}$, which is approximately $10\lambda_i$. The components of the electric field in the yz-plane, scaled by its maximum absolute value, are presented in Fig. 4-13. The field is observed at $x = 15.84 \mu\text{m}$, which is 0.72 of the waveguide length. To compare the two solutions, we first interpolate the COMSOL data onto the uniform grid, using the Matlab in-built `griddata` function, and then calculate the absolute and relative differences between electric field components. The

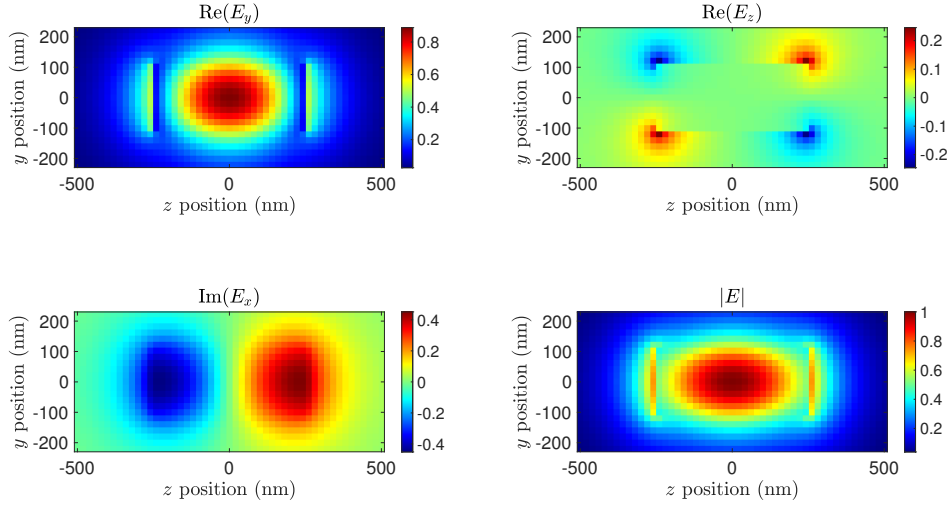


Figure 4-13: JVIE solution, obtained for $500 \text{ nm} \times 220 \text{ nm} \times 22 \mu\text{m}$ waveguide with quadratic absorber of length $4.4 \mu\text{m}$ at 1500 nm wavelength. The components of electric field in yz -plane, obtained at $x = 15.84 \mu\text{m}$ (0.72 of waveguide length) from the left end of the waveguide, are shown. Observe the qualitative agreement with the TE-mode obtained with COMSOL.

corresponding relative difference of field components is shown in Fig. 4-14. It can be seen that for the y -components of the electric field $|E_y|$ and the complex magnitudes $|E|$ the relative difference is less than 2% inside the waveguide and about $5 - 6\%$ outside. For the z - and x -components E_z and E_x it doesn't exceed 10% , except the central line along y -axis for E_y and the lines along y and z axes for E_x . However, this greater discrepancy has a simple explanation: if we look at the field components along the central lines, e.g., E_x along the z -axis, we can observe that the absolute difference ΔE_x falls to $\sim 10^{-9}$ at $z = 0$ (see Fig 4-15(a)), whereas the fields themselves at this point are of the same order of magnitude (see Fig. 4-15(b)). Hence, to achieve the relative difference near 10% , the fields should be calculated with less

than 10^{-10} error, which is hindered by the lower accuracy of the numerical solver.

Overall, we can conclude that the solutions obtained using the JVIE method proposed herein and COMSOL Multiphysics[®] software are in a good agreement.

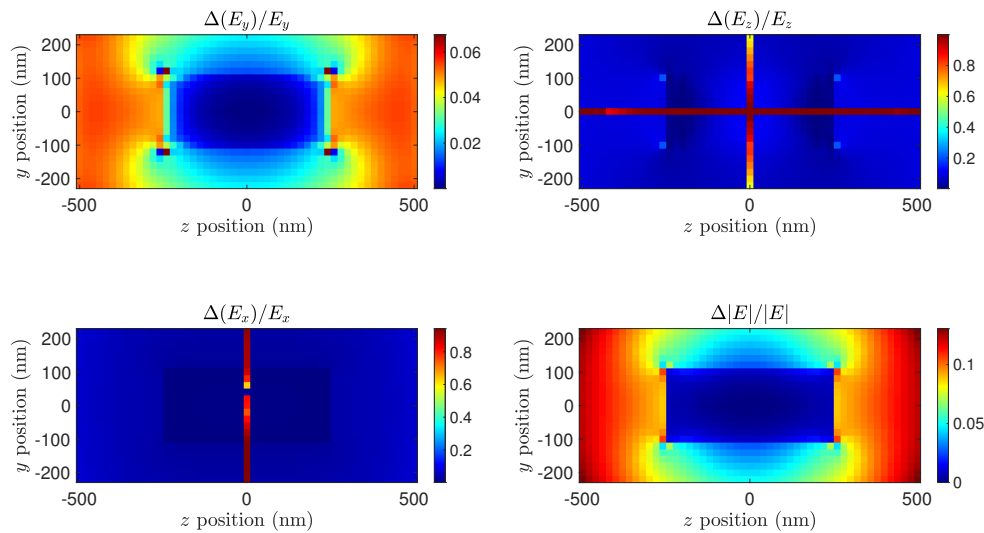


Figure 4-14: The relative difference between interpolated COMSOL and JVIE solutions. The fields are scaled by their maximum values.

4.2 Bragg grating

Previously, we have examined the adiabatic absorbers performance when terminating the uniform cross-section waveguides. Unlike uniform channels, the periodic channels can be excited at a band-gap edge, where the group velocity is close to zero, resulting in a large transition reflection at the waveguide-absorber interface. In this section, we consider the example of such periodic structure - the Bragg grating, which generates the phenomenon of *slow-light* for certain wavelengths. A typical Bragg grating is

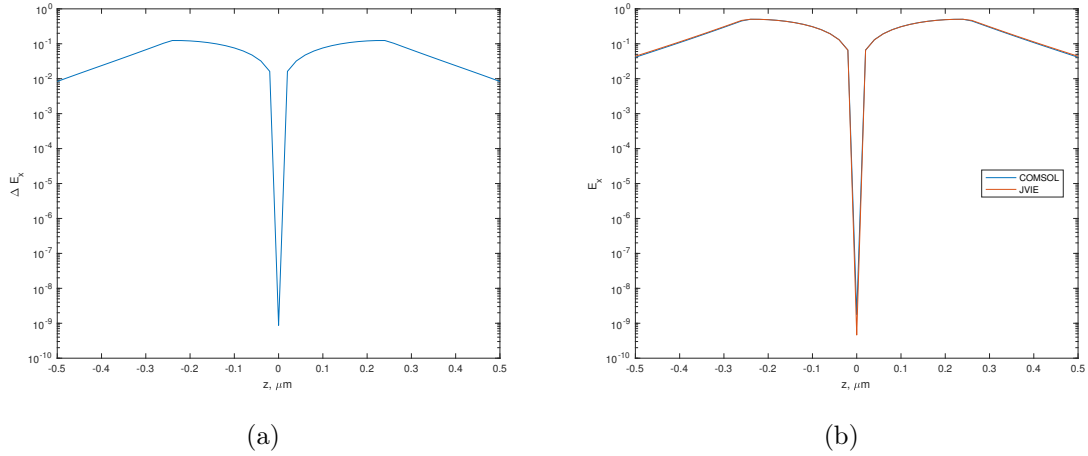


Figure 4-15: x-component of the electric field along the z-axis: (a) absolute difference between COMSOL and JVIE solutions; (b) COMSOL and JVIE solutions.

depicted in Fig. 4-16. Here we shall use the following values for the geometrical parameters in the figure:

$$D = 220 \text{ nm}, \quad W = 500 \text{ nm}, \quad \Delta W = 40 \text{ nm},$$

$$\Lambda = 320, \text{ nm}, \quad N = 100.$$

The periodic part of the structure is preceded by a uniform region of length 10Λ ($7\lambda_i/2.9\lambda_e$), which is excited using the dipole located in the same position as in the previous setup for the strip waveguide. The characteristic modulation in the waveguide leads to reflections and hence waves propagate in both directions. Therefore, we require adiabatic absorbers on both ends to truncate this structure.

To discretize this geometry, and the Y-branch splitter to follow, we use voxels of size 20 nm. This size of voxel is chosen since it can perfectly represent the cross section of the waveguides. Furthermore, at approximately 22 voxels per λ_i , this

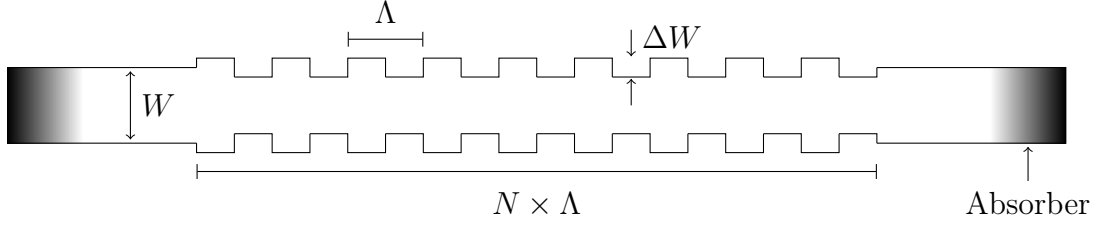


Figure 4-16: Top view of the layout for Bragg grating with period Λ , width W , corrugation depth ΔW , and length $N \times \Lambda$, where N is an integer. Since the waves propagate in both directions due to reflections from the corrugations, absorbers are required on both ends for simulations. To generate the 3D structure, this layout is extruded a distance D in the z -direction (out of the page).

resolution is fine enough to ensure accurate simulations.

Before analyzing the reflections from adiabatic absorbers in the infinite version of this structure, we first present a simulation to obtain the broadband transmission through a Bragg grating of finite length. In order to do so, we perform simulations on the setup in Fig. 4-16 over the free-space wavelength range [1520,1570]nm at a sampling resolution of 0.5 nm. A quadratic absorber of length $2.2 \mu\text{m}$ ($5\lambda_i/2.1\lambda_e$) is used on either end. For each wavelength, the transmission T through the Bragg grating is defined as the integrated square of the electric field over a voxel-wide (y, z) -slice of the structure:

$$T = \iint |\mathbf{E}|^2 dydz. \quad (4.5)$$

This chosen slice must be located after the Bragg grating terminates and before the absorber begins. The normalized transmission is plotted in Fig. 4-17. The band gap where the transmission drops is clearly visible around a Bragg wavelength of 1545nm.

If one were to analyze the group velocity, v_g , it would be seen to be positive away from the band gap, approach zero at the band gap edge, then be negative within

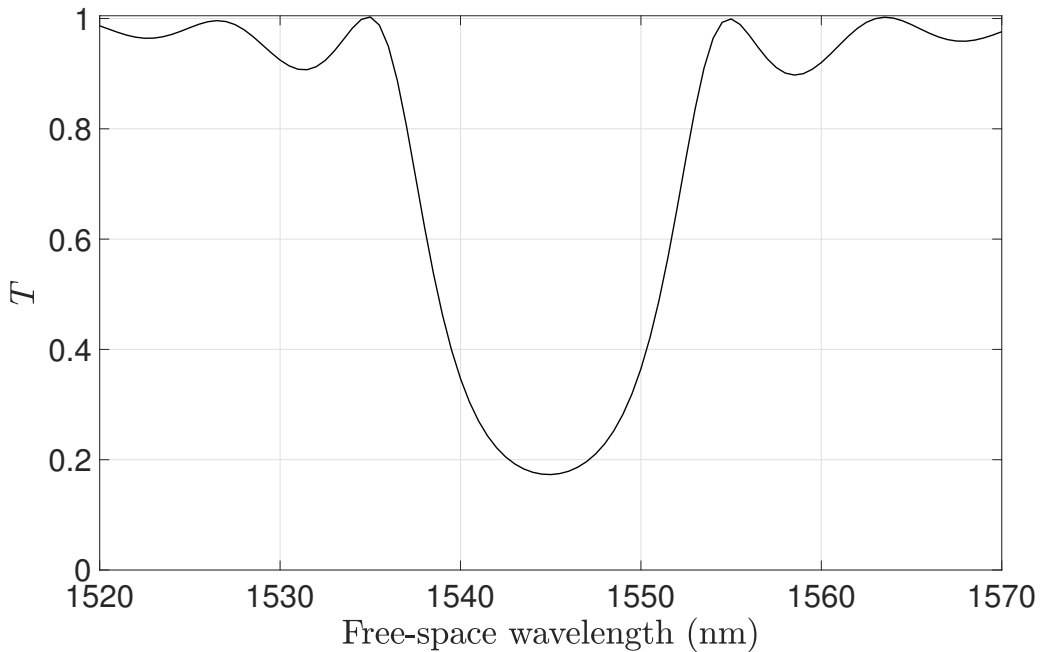


Figure 4-17: Transmission through the Bragg grating of length 100 periods. The Bragg wavelength is 1545 nm and the band gap is approximately 20 nm wide.

the band gap (see [16] for in-depth details on band gaps in periodic structures). Now suppose we were to introduce an adiabatic absorber within the periodically modulated region of the Bragg grating, as depicted in the inset in Fig. 4-18. As discussed at the end of the Chapter 3, the transition reflection from this absorber would be dominated by the $\mathcal{O}(v_g^{-2(d+2)})$ term as we go past a band gap edge. Thus we would require extremely long absorbers before returning to our asymptotic (in L) convergence rate of $\mathcal{O}(L^{-2(d+1)})$.

From a purely physical point of view, we should expect such a deterioration in performance of absorbing layers in this scenario. The aim of employing an absorbing layer is to allow the truncation of the domain *without incurring reflections*. However, the slow light phenomenon described above occurs precisely *due to the reflections* from all the way along the Bragg grating. By terminating the structure with an

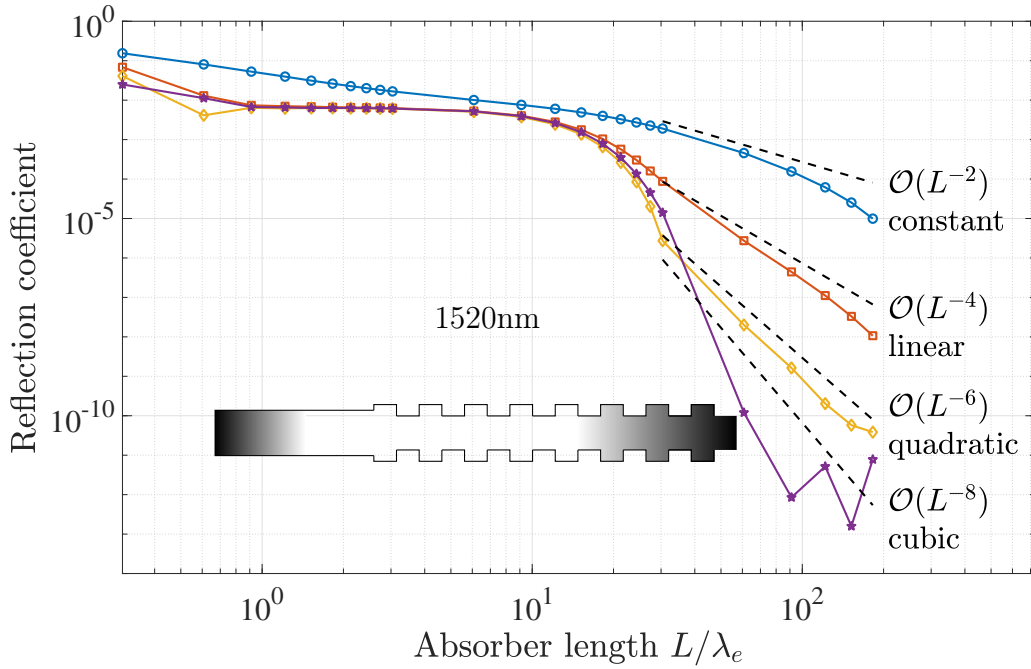


Figure 4-18: Reflection coefficient versus absorber length L for monomial profiles with the round-trip reflection set to $R_{rt} = 10^{-10}$. The Bragg grating is excited at 1520 nm free-space wavelength. The asymptotic convergence rates are eventually achieved for the first three monomials.

absorber, we lose these important reflections and, more importantly, we lose periodicity which is essential for the propagation of Bloch waves. Therefore, we anticipate that extremely long absorbers will be required to retain a sufficient number of these reflections in order to mimic the field within the infinite periodic structure.

We proceed by performing such a set of simulations in order to model the infinite Bragg grating and thereby observe the aforementioned behavior of the absorber. That is, we terminate the periodically varying region with an absorber of the same shape, as shown in Fig. 4-18. The absorption profiles are again the monomials (3.2).

First, we excite the system at a free-space wavelength of 1520 nm, away from

the band gap edge, and thus the group velocity is relatively large and positive. The round-trip reflection is fixed at $R_{rt} = 10^{-10}$. The absorber length is ranging from 1Λ ($0.7\lambda_i/0.3\lambda_e$) to 800Λ ($585\lambda_i/243\lambda_e$), where $\Lambda = 320$ nm is the grating's period. To generate the reference solution, we use an absorber of length 900Λ . The reflection coefficient R for the four monomial profiles is shown in Fig. 4-18. Immediately apparent is a clear stagnation in the transition reflection for absorbers up to approximately $40\lambda_i$ ($16.6\lambda_e$). Beyond this point, the transition reflections converge towards zero and we achieve close to the asymptotic convergence rate $\mathcal{O}(L^{-2(d+1)})$ for constant, linear, and quadratic profiles.

Next, we excite the grating close to the band gap edge, at a free-space wavelength 1538 nm, corresponding to a lower group velocity. Comparing Fig. 4-19 with Fig. 4-18, we can clearly see that reflections worsen dramatically when the system is excited near the band gap edge. Moreover, for all the profiles, the asymptotic regime is not reached for the examined range of absorber lengths, and the higher-order profiles become superior only for very long absorbers with length greater than approximately $80\lambda_e$ ($200\lambda_i$). In fact, note that the quadratic absorber is superior to the cubic absorber even for the longest absorber considered. By extrapolation from the results at this wavelength, a quadratic absorber of length approximately $375\lambda_e$ – $415\lambda_e$ ($900\lambda_i$ – $1000\lambda_i$) would be required to provide adequately small transition reflections, and hence well-approximate the infinite Bragg grating.

We conclude this section on the Bragg grating by exploring the dependency of this growth in reflection coefficient as a function of wavelength. We fix the absorber length at 50 periods ($36\lambda_i/15\lambda_e$) and consider a quadratic conductivity profile, and calculate the reflection coefficient at each free-space wavelength in the range [1520,1570]nm, with the reference solutions being calculated with quadratic absorbers of length 650 periods. The results are shown in Fig. 4-20. We observe that the reflection has two

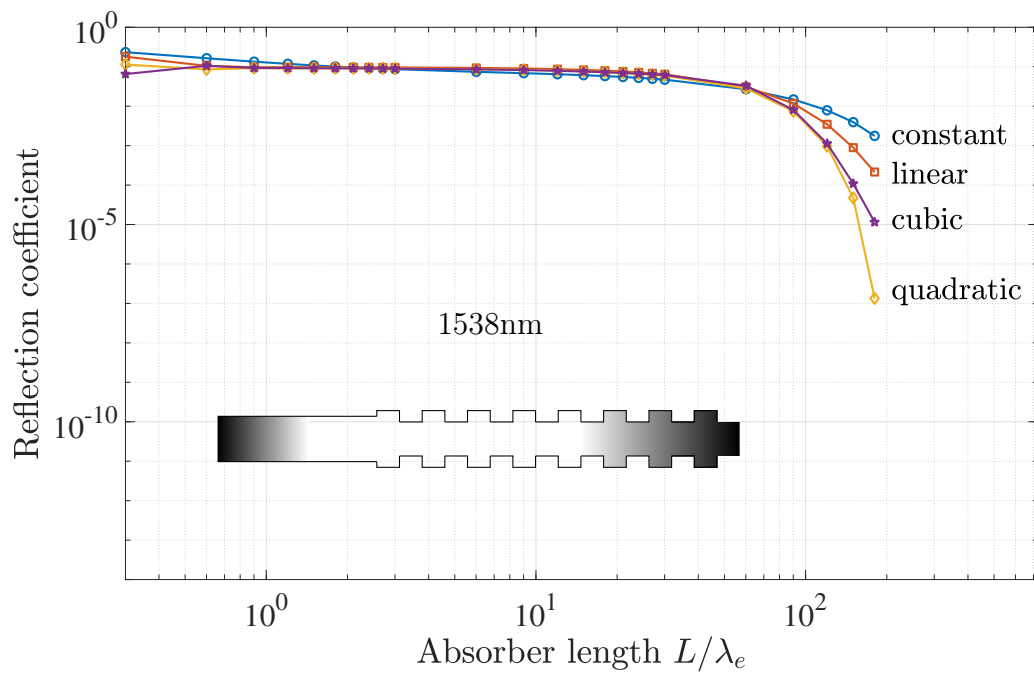


Figure 4-19: Reflection coefficient versus absorber length L for monomial profiles with the round-trip reflection set to $R_{rt} = 10^{-10}$. The Bragg grating is excited at 1538 nm free-space wavelength.

maxima, at 1540 nm and 1550 nm which correspond to the band gap edges which can be observed in Fig. 4-17. These are the points where the group velocity v_g passes through zero as it changes sign. Recall that the CMT predicts that this curve has the shape $\mathcal{O}(v_g^{-8})$ (from substituting $d = 2$ into $\mathcal{O}(v_g^{-2(d+2)})$). In light of these large reflections near or across the band gap, we anticipate that a large improvement can be achieved by balancing the predicted reflections of size $\mathcal{O}(v_g^{-2(d+2)})$ with the round-trip reflections (in a similar way to the balancing of R_t and R_{rt} for the strip waveguide in Section 4.1). We expect that such a balancing could lead to a significant reduction in the transition reflection, however the optimized absorbers would still have to be much longer than those for wavelengths away from the band gap due to the fact that reflections from far down the Bragg grating are important in approximating the infinite Bragg when we are near the band gap.

For Bragg grating applications, typically the entire finite grating is simulated, as was done at the beginning of this section. Therefore, this difficult behavior of absorbing layers in periodic media can be avoided. However, there are scenarios, such as photonic crystals [16], where simulating the propagation of light through infinite periodic structures is of interest. For analyzing infinite periodic structures, it is naturally more efficient to resort to an eigenvalue formulation of the problem (see, e.g., [16]) or exploit the periodic Green function in IE formulation [144]. Nevertheless, a case can be made for simulations with adiabatic absorbers when periodic structures with defects or aperiodic features are to be considered. For such cases, it is interesting to further understand the behavior of these absorbers in the slow-light regime in order to optimize their performance. Such a study and optimization shall be presented separately since it is not directly pertinent to the majority of nanophotonics applications.

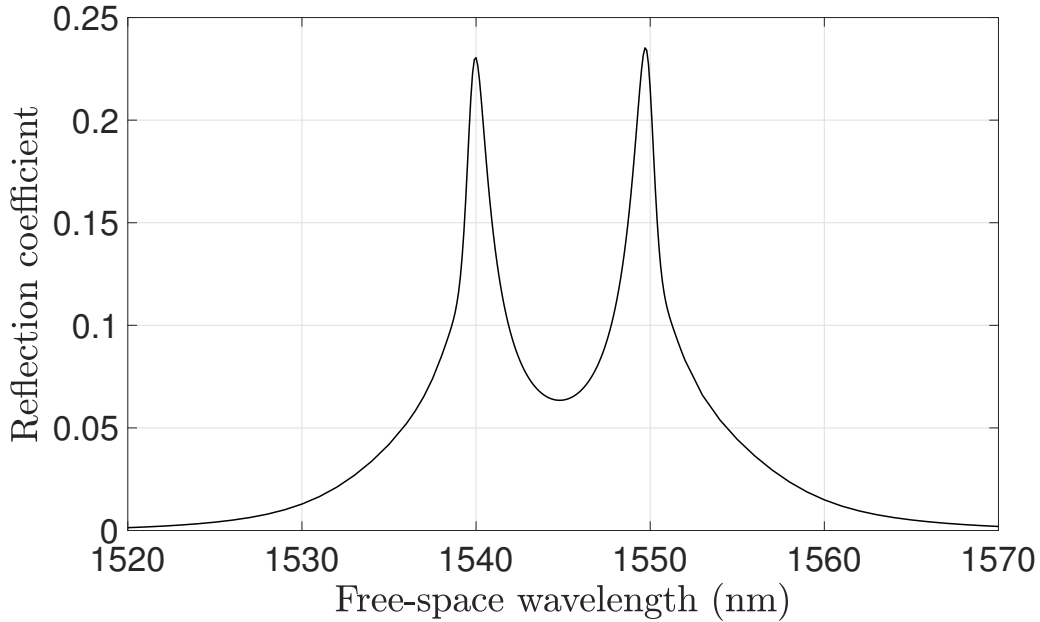


Figure 4-20: The reflection coefficient versus free-space wavelength for an absorber inside the “infinite” Bragg grating. The adiabatic absorber has a quadratic profile and length 50 periods ($36\lambda_i/15\lambda_e$). Comparing to Fig. 4-17, observe that the reflection from the absorber is large in and close to the band gap, with the peaks corresponding to the band gap edges where the group velocity changes sign.

4.3 Y-branch splitter

As the final example, we consider a practical nanophotonics simulation: the propagation of a guided mode through a Y-branch splitter, depicted in Fig. 4-21. Simulations are useful tools for optimizing the design of such structures. Indeed, the particular geometry used here is taken from [145] where numerical simulations are used to create this low-loss design.

The individual waveguide branches each have (x, y) -cross section dimensions (W, D) :

$$W = 500 \text{ nm}, \quad D = 220 \text{ nm}, \quad (4.6)$$

and the geometry of the junction is described in detail in [145]. The structure is

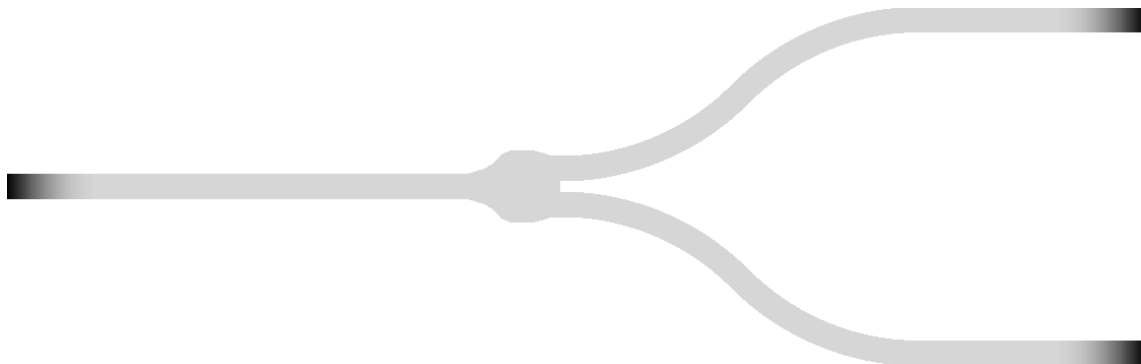


Figure 4-21: Top view of the layout of a Y-branch splitter with adiabatic absorbers appended to the waveguide-branch ends. This structure is excited by a Gaussian beam injected just to the right of the left absorber. A right-propagating mode is established, is split in half at the junction, and each half propagates along its respective curved branch.

excited at the left end by a Gaussian beam, establishing a quasi-TE guided mode in the straight waveguide which is then split at the Y-branch junction. To perform this simulation, each of the three branches is truncated with an adiabatic absorber. We choose these absorbers to have quadratic profiles and to be of length $2.2 \mu\text{m}$ ($5\lambda_i/2.1\lambda_e$). We saw for the strip waveguide that this absorber with $R_{rt} = 10^{-10}$ yielded a reflection coefficient of approximately 5×10^{-8} (see Fig. 4-10). The square of the field's magnitude is shown in Fig. 4-22. Here one can see that small reflections from the junction are propagating back down the left waveguide. This suggests that there is still some room for improvement when it comes to optimizing this Y-branch geometry. Ideally, precisely half of the energy of the incident mode would propagate down each of the two curved branches, thus requiring no reflection or scattering from the junction.

It is interesting to look at how effective the adiabatic absorbers are in this simu-

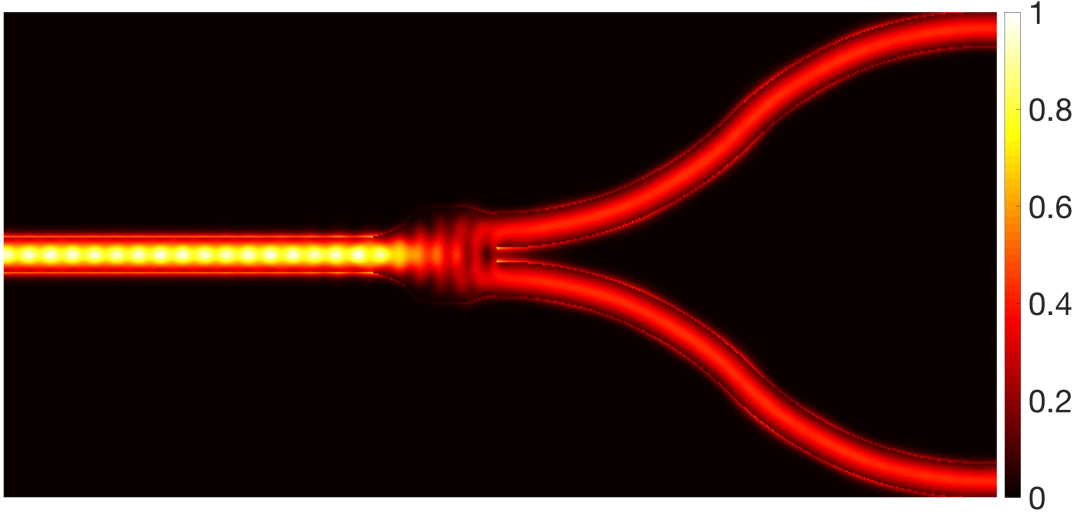


Figure 4-22: $|\mathbf{E}|^2$ for a silicon Y-branch splitter with SiO_2 cladding at 1550 nm.

lation. We do this by running the same simulation but now with absorbers of length $8.8\mu\text{m}$ ($\approx 20\lambda_i$). The field produced by this simulation, $\mathbf{E}_{20\lambda_i}$, is used as the reference solution to which we compare the field from the $2.2\mu\text{m}$ absorber simulation, $\mathbf{E}_{5\lambda_i}$. The relative difference

$$\frac{|\mathbf{E}_{20\lambda_i} - \mathbf{E}_{5\lambda_i}|^2}{\max(|\mathbf{E}_{20\lambda_i}|)^2} \quad (4.7)$$

is shown in Fig.4-23. This difference is similar to that analyzed previously and can be attributed to the reflection from the $2.2\mu\text{m}$ absorbers. We observe that the error is largest at the right ends of the curved branches and reaches a maximum of 5×10^{-6} which is substantially larger than the 5×10^{-8} observed for the strip waveguide of Section 4.1. This increase is due to the oblique propagation of the guided waves after having traveled through the bends. In the straight waveguide of Section 4.1, the waves within the structure are propagating almost perfectly parallel to the waveguide walls and hence they enter the absorber at a perpendicular angle. Such perpendicular incidence leads to the smallest possible reflections at an

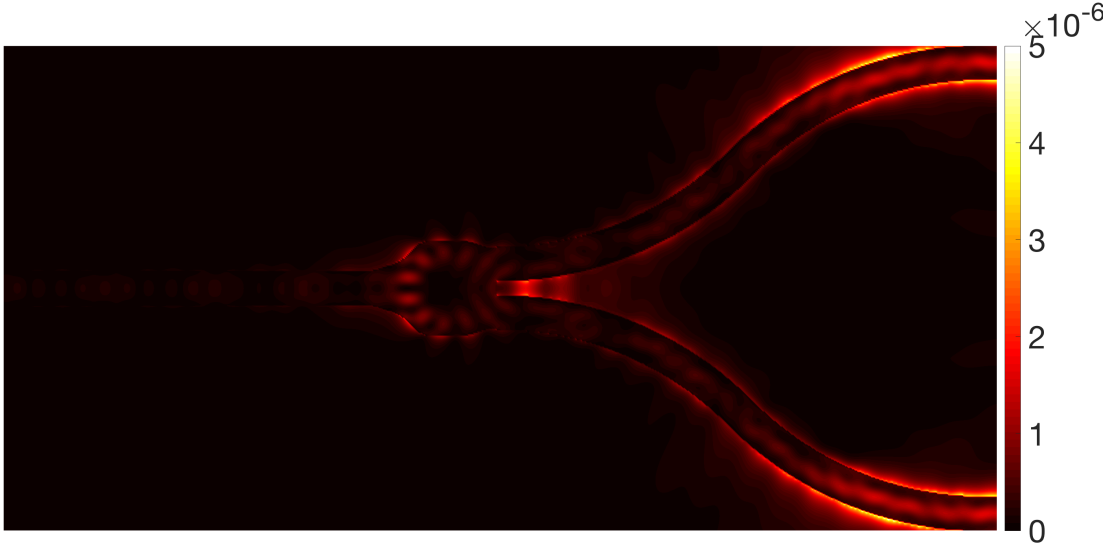


Figure 4-23: Relative difference in solution ($|\mathbf{E}|^2$) obtained using absorbers of length 5λ and 20λ . This difference can be attributed to the reflection from the 5λ -length absorbers.

interface (as can be seen from the classical Fresnel equations, see, e.g., [146]). In the Y-branch, after the waves pass through the junction and travel round the bends, it is to be expected that the waves will now have a traverse propagation component in addition to dominant longitudinal component. This means that the waves entering the absorbers appended to the right of the structure are doing so at a slightly oblique angle, leading to larger reflections. Therefore, when choosing appropriate length absorbers for bent waveguide structures, one must be cognisant of this effect. However, in the nanophotonics examples of interest here, where light is channeled by waveguides, the propagation direction is never too far from perfectly longitudinal, hence this effect will not lead to catastrophically large reflections from absorbers.

4.4 Signal-to-Noise ratio

As we observe in the previous section, with different incident angles, the absorber has different reflection coefficients. Moreover, two beams with equal incidence angle, but with different beam profiles would be reflected differently, since, e.g., the coupling coefficient M between the incident and reflected modes depends on the field spatial pattern and affects the transition reflection R_t (3.21). Furthermore, the reflection coefficient depends on the frequency of the incident light. As a result, when the reflection coefficients are mentioned, the incidence angle, frequency of the wave and the beam profile should also be noted. Hence, a practically more convenient and comprehensive measure of the effectiveness of the absorber is the signal-to-noise ratio (SNR), which differentiates the computational wave field from the standard field in an unbounded channel as a whole. We define the SNR as

$$\text{SNR} = -10 \log_{10} \left(\frac{\sum_n (\mathbf{E} - \mathbf{E}_{\text{ref}})^2}{\sum_n (\mathbf{E}_{\text{ref}})^2} \right) \quad (4.8)$$

where n is the voxel index which goes through all the voxels inside the waveguide, and \mathbf{E}_{ref} is the reference solution, obtained using the longest absorber. For a given absorber length and the monomial electric conductivity profile $\sigma_E(x) = \sigma_0(x - x_0)^d/L^d$, where $d = 0, 1, 2, 3$, the round-trip reflection R_{rt} is defined by σ_0 (3.19). Thus, it would be interesting to study the SNR dependence on σ_0 , for a given profile and fixed absorber length. Fig. 4-24 contains the results of evaluating the SNR for the range of σ_0 from 10^4 to 10^5 S and absorbers with quadratic profile and lengths from $5\lambda_i$ to $20\lambda_i$. The system is excited with 1550 nm free-space wavelengths. To obtain the reference solution, the absorber of length $L = 100\lambda_i$ and quadratic profile was used. As we can see, the SNR dependence on σ_0 is not monotonical. Indeed, for

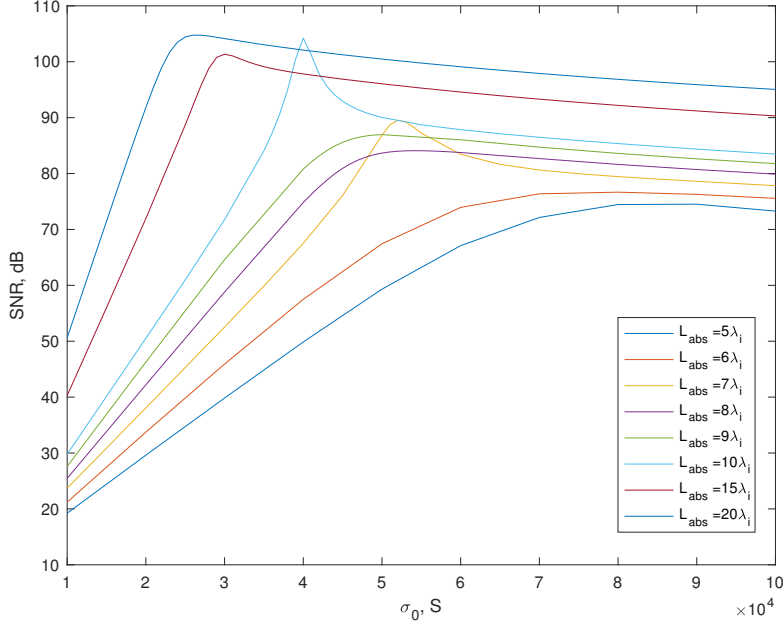


Figure 4-24: SNR dependence on σ_0 for a given profile and fixed absorber length.

the low values of σ_0 the transition between the waveguide and the absorber is very smooth so the transition reflection is low and the round trip-reflection dominates, resulting in a decrease of total reflection and increase of the SNR with increasing integrated absorber loss. Further increasing the σ_0 the transition reflection grows higher and become to prevail, therefore the SNR reaches its maximum and then starts to decrease. The second observation is that using a longer absorber leads to better average performance over the range of σ_0 . However, for the certain lengths of absorber, e.g., for $L_{abs} = 7\lambda_i$ and $L_{abs} = 10\lambda_i$, the peak SNR is greater that of the longer absorbers with the same sigma σ_0 . This sharper peaks may occur due to destructive interference of the round-trip and the transition reflection, which we have already encountered when trying to balancing between these two reflections. In addition, we have investigated the effect of discretization. Fig 4-25 present the SNR

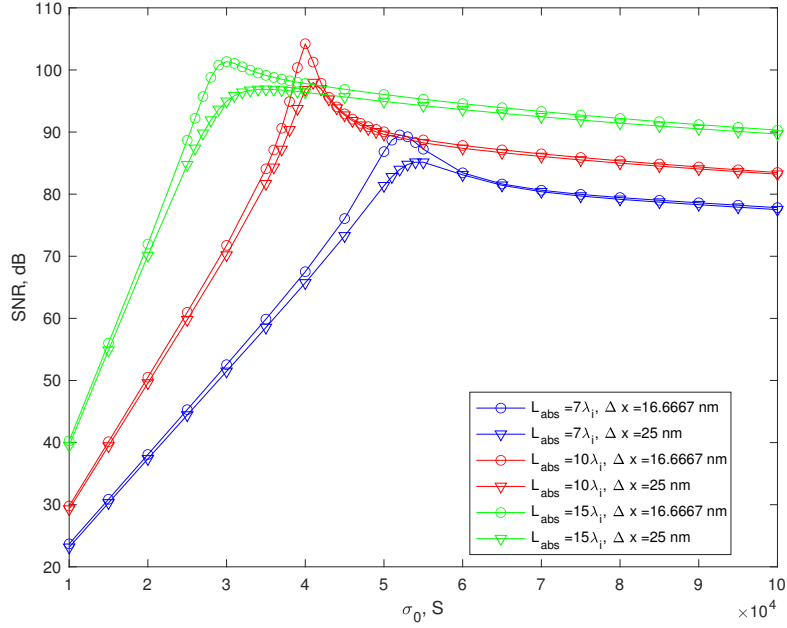


Figure 4-25: SNR dependence on resolution.

obtained with the absorbers of equal parameters, discretized with 50/3nm and 25nm voxels. We can observe that the curves for the different resolutions are very close except the vicinity of the peaks.

Although it is obvious that for each length of the absorber there is a certain maximum SNR, and discretization, apparently, shifts the maxima only a little, it is necessary to solve the problem of multi-parameter optimization in order to achieve maximum performance. Performing such optimization is an interesting task which we preserve for future work.

Chapter 5

Discussion

In this chapter, we will discuss the advantages and disadvantages of the proposed method when applied to the modeling of nanophotonic structures. Moreover, we will propose the possible alternatives and improvements that could help in diminishing the drawbacks and can be considered as the directions of future research.

First of all, the staircase error introduced by the uniform grid to achieve the Toeplitz system matrix and enable the FFT acceleration can be a major limitation for objects with curved surfaces and thin coatings. Evidently, a discretization with tetrahedra could be more efficient in a sense that with the same average size of the element it is able to approximate the structures with non-planar surfaces or complex geometries more accurately. Moreover, there are several FFT-based methods with $\mathcal{O}(N \log N)$ complexity, which are able to speed-up the VIE discretized on irregular meshes. We would like to note that right-angled photonics structures such as waveguide channels or gratings, which are considered this thesis, can be fairly represented by voxels with much less number of discretization elements than it would be with tetrahedra. Nonetheless, the concept of the adiabatic absorber is not restricted to

regular meshes. Furthermore, one of the key features of the proposed VIE method is the reduction from 6D volume-volume to 4D surface-surface integrals. This reduction technique is also not restricted to a specific discretization scheme, namely, the support of the basis/testing functions could vary from voxels to general polyhedra. We can conclude that the proposed algorithms can be extended to irregular geometries without the loss of their fast nature.

Next, it is worth mentioning again, that nanophotonic devices are typically composed of piecewise homogeneous regions. Indeed, in all the examples considered in this thesis, the only inhomogeneous regions are the absorbers, which in most cases occupy a relatively small part of the computational domain, and the other regions, e.g. the core of the waveguide, are homogeneous. Therefore, the memory requirements and computational complexity can be reduced significantly by utilizing the surface integral equation formulation for large homogeneous regions, and use VIE formulation for the absorbers regions only. Such hybrid volume-surface integral equation formulation is typically used for the numerical studies of electromagnetic scattering from the composite conducting-dielectric objects, where the volume integral equation is applied to the inhomogeneous lossy or lossless dielectric region, and the surface integral equation is applied on the surfaces of perfectly conductive objects (or to the open or closed perfectly conductive surfaces) [77, 78, 79]. Nonetheless, it can be easily reformulated for our case of the combination of homogeneous dielectric regions and inhomogeneous ones. Moreover, this approach together with domain decomposition [147] could be very useful in the modeling of combinations of several different nanophotonic devices, e.g., ring resonator and waveguides. With this approach, for each subdomain, the individual IE formulation (VIE, SIE or VSIE for composite domains) and discretization can be chosen according to its shape, material properties and the fraction of homogeneity. This would make the method computa-

tionally efficient for the modeling of large complex systems and give more flexibility in the representation of the geometry of the devices.

Finally, we have mentioned that in some cases optimization of the absorber's parameters could further reduce the reflections, and there are several possible directions of improvement, such as balancing the round-trip and transition reflection, finding less-reflective conductivity profile function than monomial, etc. As we have mentioned in Section 4.4, for practical purposes, an optimization of the absorber for all problem parameters such as wavelength, refractive index, period and corrugation width of the grating, should be performed. At this stage, the turn of machine learning techniques [148, 149], which are capable to obtain a compact representation of multi-parameter design space revealing the relationship between different design parameters, naturally comes. Exploiting the machine learning techniques would enable a fast optimization of the absorber's parameters, allow making informed decisions based on the relative priorities of different performance metrics (e.g., reflection level and computational time, both depending on the length of the absorber), and furthermore, could provide new insights about the absorber's behavior in a challenging slow-light regime when the periodic structure is excited near the band edge.

Chapter 6

Conclusions

Integral equation methods are traditionally used to simulate the scattering of waves from finite obstacles. However, when the obstacle is infinite in extent, such as nanophotonic waveguide structures, something must be done to truncate the domain in order to make the simulation feasible and minimize spurious reflections. In this thesis, we presented and analyzed one such truncation approach, namely the introduction of adiabatic absorbing regions. The novelty of this thesis lies in the application of adiabatic absorbers within the VIE method. In particular, we employ a VIE formulation that allows these absorbers to be introduced in a simple and straightforward manner which importantly does not affect the “fast” nature of the solver, thereby enabling rapid nanophotonics simulations. Moreover, we have developed the new fully numerical method for evaluation of the singular integrals over quadrilateral elements, arising in the calculation of Galerkin inner products, associated with the integral operators. We demonstrate via various numerical experiments the performance of the proposed algorithms in terms of accuracy and computational efficiency. The presented method, dubbed DIRECTFN-quad, is applicable to evalu-

ation the weakly and strongly singular integrals over arbitrary planar, bilinear and curvilinear quadrilaterals without modification of algorithms.

We have outlined the application of the VIE method and the appropriate implementation of monomial adiabatic absorbers within the VIE setting, and derived the asymptotic relations for the reflection coefficients. We have examined the performance of adiabatic absorbers in three examples: a straight dielectric strip waveguide, a Bragg grating, and a Y-branch splitter. We have shown that the behavior of the reflections from adiabatic absorbers is in keeping with the asymptotic results from the coupled-mode theory. In particular, the transition reflections decay as $\mathcal{O}(L^{-2(d+1)})$, where L is the length of the absorber and d the degree of the monomial absorption profile.

Next, we have compared the results of our simulation of light propagation inside the silicon strip waveguide, which is a very common structure in practical applications, with the first TE mode profile, obtained using COMSOL Multiphysics[®] software, and demonstrated that the results are in a good agreement.

In Section 4.2, we performed simulations for a practical problem arising in photonics applications, namely the broadband simulation of the transmission through a Bragg grating. It was seen that, if the Bragg grating is simulated in its entirety and is truncated on the straight portions by adiabatic absorbers, accurate simulations result with short absorbers (approximately $5\lambda_i/2.1\lambda_e$ long).

We further analyzed how the effectiveness of adiabatic absorbers depends on the group velocity within a periodic structure. We truncated a Bragg grating in its region of periodic modulation and demonstrated that, in such cases, adiabatic absorbers can perform well when the system is excited away from the band-gap edge. However, near the band gap when the group velocity approaches zero, extremely long absorbers are required to reduce transition reflections. Again, this is in keeping with

asymptotic results from coupled-mode theory. In the nanophotonics applications of interest here, where devices are to be simulated in their entirety, one is unlikely to truncate a periodic structure with an absorber within the region of modulation. Moreover, a more natural approach of analyzing infinite periodic structures is to resolve an eigenvalue problem, or, within the context of IE methods, to exploit the periodic Green function). Nevertheless, a case can be made for simulations with adiabatic absorbers when periodic structures with defects or aperiodic features are to be considered. That being said, there is a great deal of room for the optimization of adiabatic absorbers in these slow-light scenarios. Such optimization requires a careful study of the slow-light behavior and is left for future work.

The final structure we simulated was the Y-branch splitter. We saw that, with quadratic absorbers of length $5\lambda_i/2.1\lambda_e$, the reflections from the absorbers were negligible when compared to the total field. This was even in spite of the slightly larger than anticipated reflections from the right-hand absorbers where the propagating waves had picked up a small transverse component due to traveling round the waveguide bends. When the waves enter the absorbers with off-perpendicular incidence, the reflections are increased. However, in nanophotonics structures, this transverse component will always be small, therefore, the increase in reflection will not be too large.

In addition, we have introduced the Signal-to-Noise ratio as an alternative measure of absorber performance and investigated its dependence on the absorption rate with the fixed length of the absorber.

Overall, we observe that the proposed adiabatic absorber performs extremely well in the VIE setting when terminating uniform unbounded structures, and show the difficulties arising when terminating periodic ones.

In addition, in Section 2.7 we presented some results pertaining to the iterative

solution of the VIE’s discrete system. For high-frequency problems (as encountered in photonics), the number of iterations required for an iterative solver to converge is large, regardless of the numerical method employed (e.g., finite difference, finite element, integral equation). Therefore, all numerical methods require effective preconditioners in order to make their application efficient. When the VIE (2.13) is discretized on a uniform grid, the resulting matrix in the discrete system has a three-level block-Toeplitz form. An effective preconditioner for this matrix can be obtained by making a circulant approximation on one or more levels of this Toeplitz matrix. The results showed that such a preconditioner is extremely effective and renders the number of iterations small and independent of the structure’s length. Although constructing and inverting the preconditioner takes time comparable to that of the iterative solution of the preconditioned system, the total time appears to be several times less, than the solution of the unpreconditioned one.

We can conclude that the presented VIE method together with appropriate preconditioning is an effective and fast simulation tool for the modeling of nanophotonic devices, although there is still great room for improvement. Nonetheless, the existing limitations of the presented method open the directions for future research.

As we have mentioned in the Discussion chapter, the concept of adiabatic absorber in IE formulation is not restricted to uniform discretization. Moreover, one of the key features of the proposed VIE solver is the reduction technique from 6D volume-volume to surface-surface integrals, which is also not restricted to specific support of the basis/testing functions. Finally, there are plenty of FFT-based acceleration methods with $\mathcal{O}(N \log N)$ complexity, which can work with irregular meshes [49, 50, 52, 53, 56, 57]. Taking into account all of the above, we come to the conclusion that the proposed method can be extended to irregular grids while maintaining its fast nature. It would be helpful in the cases when the adequate representation of the

geometry is not feasible using the voxelized grid.

Another promising direction of future work is the hybridization of the proposed VIE method with the SIE formulations. Within the VSIE formulations [77, 78, 79], for inhomogeneous regions such as absorbers, the VIE formulation is used, whereas homogeneous regions such as dielectric waveguides and/or metallic surfaces are handled using the SIE formulations. This leads to a substantial reduction in memory requirements and computational complexity. By further enhancement of this approach with the domain decomposition method [147], modeling of large complex systems consisting of many devices become computationally efficient.

Next, exploiting the machine learning techniques [148, 149] would enable a fast optimization of the absorber for all range of input parameters such as wavelength, refractive index, period and corrugation width. This would allow making informed decisions about the particular choice of the absorber parameters based on the relative priorities of different performance metrics (e.g., reflection level and computational time, both depending on the length of the absorber), and furthermore, could provide new insights of how to improve the absorber's performance in a challenging slow-light regime when the periodic structure is excited near the band edge.

Appendix A

Numerical Tests of DIRECTFN-quad

In this thesis, we have introduced the novel fully numerical method for evaluation of weakly and strongly singular integrals over quadrilateral elements, dubbed DIRECTFN-quad. As we have already mentioned, the proposed algorithm can be applied without modification to the cases with basis functions of any order, as well as for integration over non-squared and curvilinear elements. Here we demonstrate this via numerical examples. Firstly, we investigate the robustness of the proposed scheme to the quality factor of the elements. Next, we provide an example with first-order vector basis functions [126, 117]. Finally, we consider the case of curvilinear elements.

A.1 Sensitivity to the quality factor of the elements

Here we present some additional results in order to investigate the sensitivity of the proposed method to the mesh quality, i.e. various levels of skewness of elongated

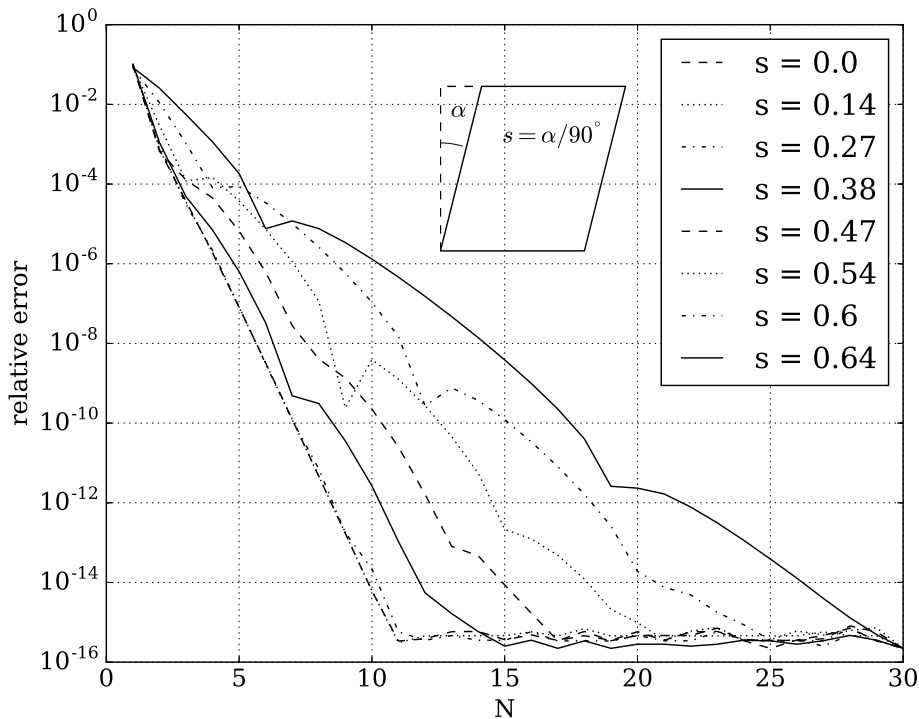


Figure A-1: Relative error in computing the weakly singular integrals (2.123) over coincident elongated quadrilaterals as a function of the order of the 1-D Gaussian quadrature.

quadrilaterals, where skewness is defined by

$$s = \max \left[\frac{\theta_{max} - \pi/2}{\pi/2}, \frac{\pi/2 - \theta_{min}}{\pi/2} \right]. \quad (\text{A.1})$$

As shown in Fig. A-1, the proposed method becomes less efficient and require more integration points for more elongated elements. Indeed, the natural drawback of the methods involving such coordinate transformation, e.g. the original DIRECTFN for triangles, is that they quickly become much less efficient as skewness increases

to very high values. However, the standard mesh generation tools used for real-life applications, are likely to exclude such poorly-shaped elements.

A.2 Weakly and strongly singular integrals with vector basis functions

In the next set of experiments, the following weakly and strongly singular integrals are computed:

$$I_{m,n}^{\text{WS}} = \int_{E_P} \mathbf{f}_m(\mathbf{r}) \cdot \int_{E_Q} G(\mathbf{r}, \mathbf{r}') \cdot \mathbf{f}'_n(\mathbf{r}') dS' dS, \quad (\text{A.2})$$

$$I_{m,n}^{\text{SS}} = \int_{E_P} \mathbf{f}_m(\mathbf{r}) \cdot \int_{E_Q} (\nabla G(\mathbf{r}, \mathbf{r}') \times \mathbf{f}'_n(\mathbf{r}')) dS' dS, \quad (\text{A.3})$$

where E_P and E_Q are observation and source quadrilateral elements, respectively. Here $\mathbf{f}_m(\mathbf{r})$ and $\mathbf{f}_n(\mathbf{r}')$, ($m, n = 1, 2, 3, 4$) are first-order vector basis functions [126, 117]. Again, we consider the three singular integrals with coincident, edge adjacent and vertex adjacent patches. All patches are squared with edge-length equal to $d = 0.1\lambda$. The choice of the order of the quadrature rule for the associated 1-D integrals used in the previous example is by no means optimal. Hence, this time we vary the order of the integration rule for each one of the 1-D integrals while keeping the other three fixed and equal to $N = 20$. The reference values are obtained by using a high number of integration points for all four one-dimensional integrations, i.e., $N_1 = N_2 = N_3 = N_4 = 20$. Finally, we evaluate the maximum relative error, defined as

$$\varepsilon_{\max} = \max_{m,n=1,2,3,4} \varepsilon_{m,n}, \quad (\text{A.4})$$

where

$$\varepsilon_{m,n} = \left\| \left\| \frac{\|I_{m,n} - I_{m,n}^{\text{ref}}\|_2}{\|I_{m,n}^{\text{ref}}\|_2} + \epsilon \right\|_2 \right\|. \quad (\text{A.5})$$

One can easily conclude by inspecting the results in Figs. A-2–A-4, that the 1-D integrals that can be in principle evaluated analytically (in the case of simple geometries), e.g., integration over Λ in all the cases, require fewer integration points for the specified accuracy.

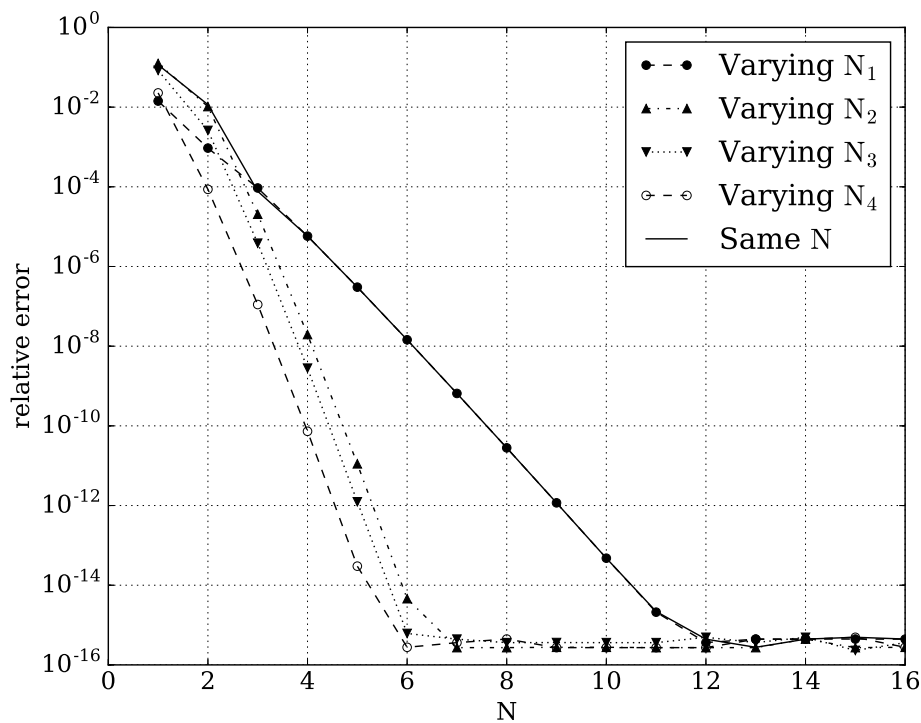


Figure A-2: Relative error in computing the weakly singular integrals (A.2) over coincident squares as a function of the order of the 1-D Gaussian quadrature.

Hence, the efficiency of DIRECTFN-quad can be significantly improved by a

judicious choice of integration orders for the different 1-D integrals. The optimal choice of the various integration orders is left for future work.

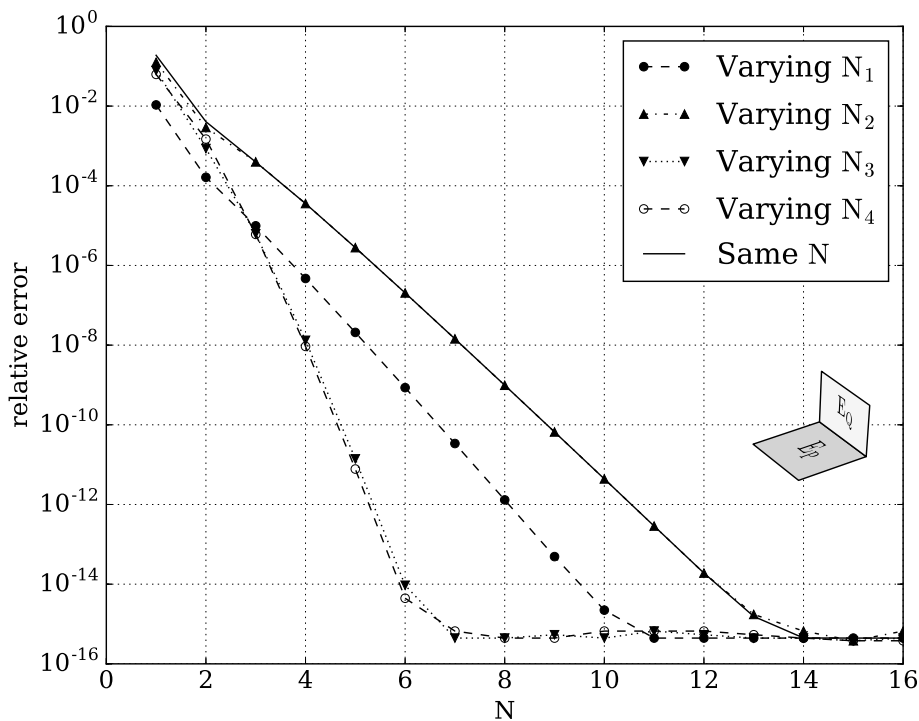


Figure A-3: Relative error in computing the strongly singular integrals (A.3) over edge-adjacent squares as a function of the order of the 1-D Gaussian quadrature.

A.3 Singular integrals over quadratic curvilinear quadrilaterals

In the last set of experiments the case of quadratic curvilinear elements, i.e. 9-node generalized quadrilaterals, is presented. The only difference from the algorithm for

planar elements is in the surface parametrization: equation (2.46) should be replaced by

$$\mathbf{r}(u, v) = \sum_{i=1}^3 \sum_{j=1}^3 L_i^2(u) L_j^2(v) \mathbf{r}_{ij}, \quad (\text{A.6})$$

where $L_i^2(u)$ and $L_j^2(v)$ are Lagrange interpolation polynomials of second order and \mathbf{r}_{ij} are position vectors of the interpolation nodes [114].

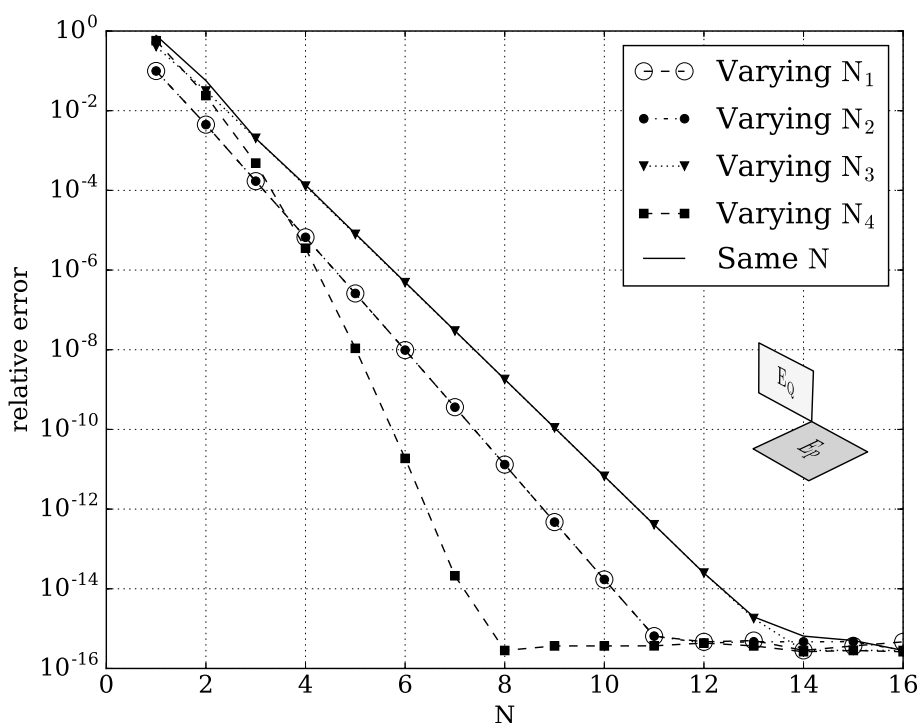


Figure A-4: Relative error in computing the strongly singular integrals (A.3) over vertex-adjacent squares as a function of the order of the 1-D Gaussian quadrature.

The weakly singular integrals (A.2) are computed for $E_P \equiv E_Q \equiv Q_1$, corresponding to ST case, and strongly singular integrals (A.3) are computed for $E_P \equiv Q_1$,

$E_Q \equiv Q_2, Q_3$, corresponding to EA and VA cases, respectively.

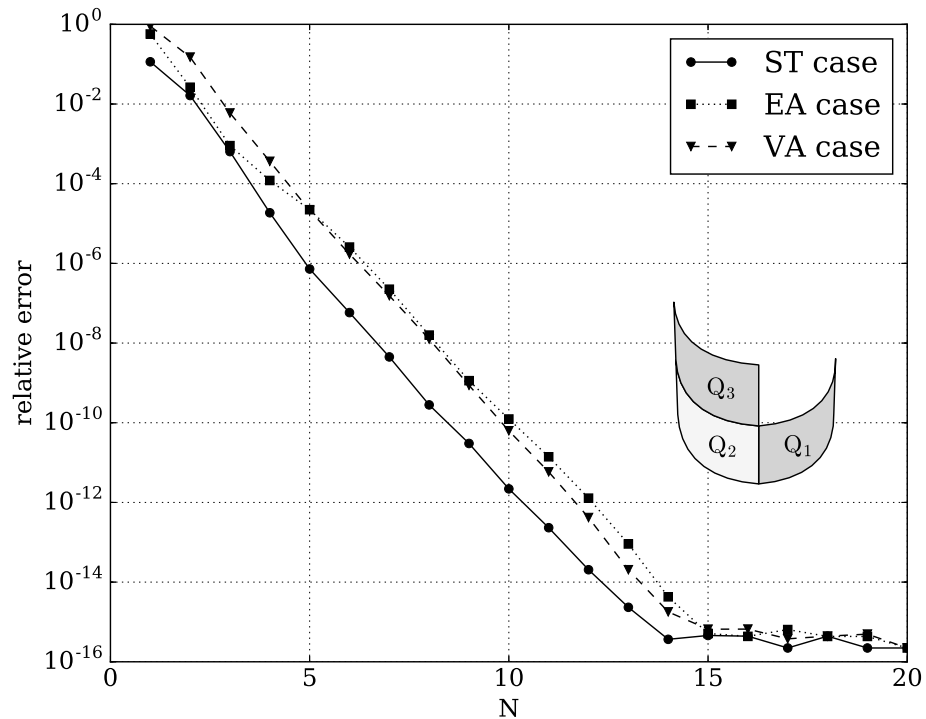


Figure A-5: Relative error in computing the weakly and strongly singular integrals over quadratic curvilinear elements as a function of the order of the 1-D Gaussian quadrature

The geometrical details of the curvilinear elements can be found in [125]. As illustrated in Fig. A-5, the fully numerical method presented herein can successfully handle the weakly and strongly singular integrals arising in Galerkin SIE formulations over curvilinear quadrilateral elements, without the need of modifying the main algorithms.

Bibliography

- [1] Richard Soref. The Past, Present, and Future of Silicon Photonics. *IEEE J. Sel. Top. Quantum Electron.*, 12(6):1678–1687, 2006.
- [2] Graham T. Reed, editor. *Silicon Photonics: The State of the Art*. Wiley, Chichester, UK, 2008.
- [3] Leonid Khriachtchev. *Silicon Nanophotonics: Basic Principles, Present Status, and Perspectives*. Jenny Stanford Publishing, 2nd edition, 2016.
- [4] A. Biberman, S. Manipatruni, N. Ophir, L. Chen, M. Lipson, and K. Bergman. First demonstration of long-haul transmission using silicon microring modulators. *Optics Express*, 18:15544, July 2010.
- [5] V. R. Almeida, C. A. Barrios, R. R. Panepucci, and M. Lipson. All-optical control of light on a silicon chip. *Nature*, 431:1081–1084, 2004.
- [6] J. K. Doylend and A. P. Knights. The evolution of silicon photonics as an enabling technology for optical interconnection. *Laser Photon. Rev.*, 6(4):504–525, 2012.
- [7] Po Dong, Young Kai Chen, Guang Hua Duan, and David T. Neilson. Silicon photonic devices and integrated circuits. *Nanophotonics*, 3(4-5):215–228, 2014.

- [8] Lukas Chrostowski, Samantha Grist, Jonas Flueckiger, Wei Shi, Xu Wang, Eric Ouellet, Han Yun, Mitch Webb, Ben Nie, Zhen Liang, Karen C. Cheung, Shon A. Schmidt, Daniel M. Ratner, and Nicolas A. F. Jaeger. Silicon photonic resonator sensors and devices. volume 8236, page 823620. International Society for Optics and Photonics, 2012.
- [9] N. A. Yebo, D. Taillaert, J. Roels, D. Lahem, M. Debliqy, Z. Hens, and R. Baets. Integrated Optical Gas Sensors on Silicon-on-Insulator Platform. In *Integr. Photonics Res. Silicon Nanophotonics Photonics Switch.*, page JTUB17, Washington, D.C., 2010. OSA.
- [10] M. Lipson. Guiding, Modulating, and Emitting Light on Silicon—Challenges and Opportunities. *Journal of Lightwave Technology*, 23:4222, 2005.
- [11] Sahba Talebi Fard, Samantha M. Grist, Valentina Donzella, Shon A. Schmidt, Jonas Flueckiger, Xu Wang, Wei Shi, Andrew Millspaugh, Mitchell Webb, Daniel M. Ratner, Karen C. Cheung, and Lukas Chrostowski. Label-free silicon photonic biosensors for use in clinical diagnostics. In Joel Kubby and Graham T. Reed, editors, *Silicon Photonics VIII*, volume 8629, page 862909. International Society for Optics and Photonics, 2013.
- [12] Valentina Donzella, Ahmed Sherwali, Jonas Flueckiger, Samantha M. Grist, Sahba Talebi Fard, and Lukas Chrostowski. Design and fabrication of SOI micro-ring resonators based on sub-wavelength grating waveguides. *Opt. Express*, 23(4):4791, 2015.
- [13] I-Wei Hsieh, Xiaogang Chen, Jerry I. Dadap, Nicolae C. Panoiu, Richard M. Osgood, Sharee J. McNab, and Yurii A. Vlasov. Ultrafast-pulse self-phase

- modulation and third-order dispersion in Si photonic wire-waveguides. *Opt. Express*, 14(25):12380, 2006.
- [14] Jidong Zhang, Qiang Lin, Giovanni Piredda, Robert W. Boyd, Govind P. Agrawal, and Philippe M. Fauchet. Optical solitons in a silicon waveguide. *Opt. Express*, 15(12):7682, 2007.
- [15] W. Ding, C. Benton, A. V. Gorbach, W. J. Wadsworth, J. C. Knight, D. V. Skryabin, M. Gnan, M. Sorrel, and R. M. De La Rue. Solitons and spectral broadening in long silicon-on-insulator photonic wires. *Opt. Express*, 16(5):3310, 2008.
- [16] John D. Joannopoulos, Steven G. Johnson, Joshua N. Winn, and Robert D. Meade. *Photonic Crystals: Molding the Flow of Light*. Princeton University Press, 2011.
- [17] Youg Xu, Reginald K. Lee, and Amnon Yariv. Propagation and second-harmonic generation of electromagnetic waves in a coupled-resonator optical waveguide. *J. Opt. Soc. Am. B*, 17(3):387, 2000.
- [18] Marin Soljačić, Steven G. Johnson, Shanhui Fan, Mihai Ibanescu, Erich Ippen, and J. D. Joannopoulos. Photonic-crystal slow-light enhancement of nonlinear phase sensitivity. *J. Opt. Soc. Am. B*, 19(9):2052, 2002.
- [19] Hatice Altug and Jelena Vučković. Experimental demonstration of the slow group velocity of light in two-dimensional coupled photonic crystal microcavity arrays. *Appl. Phys. Lett.*, 86(11):111102, 2005.
- [20] M. L. Povinelli, Steven G. Johnson, and J. D. Joannopoulos. *Opt. Express*.

- [21] R. Ramaswami, K.N. Sivarajan, and Galen H. Sasaki. *Optical Networks: A Practical Perspective*. Morgan Kaufmann, 3rd edition.
- [22] A. Yu. Petrov and M. Eich. Zero dispersion at small group velocities in photonic crystal waveguides. *Appl. Phys. Lett.*, 85(21):4866–4868, 2004.
- [23] Daisuke Mori and Toshihiko Baba. Wideband and low dispersion slow light by chirped photonic crystal coupled waveguide. *Opt. Express*, 13(23):9398, nov 2005.
- [24] Shousaku Kubo, Daisuke Mori, and Toshihiko Baba. Low-group-velocity and low-dispersion slow light in photonic crystal waveguides. *Opt. Lett.*, 32(20):2981, 2007.
- [25] Daisuke Mori, Shousaku Kubo, Hirokazu Sasaki, and Toshihiko Baba. Experimental demonstration of wideband dispersion-compensated slow light by a chirped photonic crystal directional coupler. *Opt. Express*, 15(9):5264, 2007.
- [26] Lukas Chrostowski and Michael Hochberg. *Silicon photonics design: from devices to systems*. Cambridge University Press, 2015.
- [27] Pieter Dumon, Gino Priem, Luis Romeu Nunes, Wim Bogaerts, Dries Van Thourhout, Peter Bienstman, Tak Keung Liang, Masahiro Tsuchiya, Patrick Jaenen, Stephan Beckx, Johan Wouters, and Roel Baets. Linear and nonlinear nanophotonic devices based on silicon-on-insulator wire waveguides. *Japanese Journal of Applied Physics*, 45(8B):6589–6602, August 2006.
- [28] Dong Ho Lee, Sung Joong Choo, Uiseok Jung, Kyung Woon Lee, Kwang Woong Kim, and Jung Ho Park. Low-loss silicon waveguides with sidewall roughness

- reduction using a SiO₂ hard mask and fluorine-based dry etching. *Journal of Micromechanics and Microengineering*, 25(1):015003, 2014.
- [29] A. G. Polimeridis, J. Fernández Villena, L. Daniel, and J. K. White. Stable FFT-JVIE solvers for fast analysis of highly inhomogeneous dielectric objects. *Journal of Computational Physics*, 269:280–296, 2014.
- [30] John Volakis. *Integral equation methods for electromagnetics*. The Institution of Engineering and Technology, 2012.
- [31] J Jin. *Finite Element Method in Electromagnetics*. Wiley, 2002.
- [32] A. Taflové and S. C. Hagness. *Computational Electrodynamics: The Finite-Difference Time-Domain Method*. Norwood, MA: Artech House, 2000.
- [33] Ming Fang, Zhi Xiang Huang, Wei E.I. Sha, Xiaoyan Y.Z. Xiong, and Xian Liang Wu. Full hydrodynamic model of nonlinear electromagnetic response in metallic metamaterials. *Prog. Electromagn. Res.*, 157:63–78, 2016.
- [34] Lumerical. <https://www.lumerical.com/>.
- [35] FullWAVETM. <https://www.synopsys.com/optical-solutions/rsoft/passive-device-fullwave.html>.
- [36] Jean-Pierre Berenger. A perfectly matched layer for the absorption of electromagnetic waves. *Journal of computational physics*, 114(2):185–200, 1994.
- [37] Weng Cho Chew, Mei Song Tong, and Bin Hu. Integral equation methods for electromagnetic and elastic waves. *Synthesis Lectures on Computational Electromagnetics*, 3(1):1–241, 2008.

- [38] R. F. Harrington. *Field computation by moment methods*. New York: Macmillan, FL, Krieger, 1983.
- [39] Jiming Song. Multilevel fast multipole algorithm for electromagnetic scattering by large complex objects. *IEEE Trans. Antennas Propag.*, 45(10):1488–1493, 1997.
- [40] X.Q. Sheng, J.-M. Jin, J. Song, W.C. Chew, and C.-C. Lu. Solution of combined-field integral equation using multilevel fast multipole algorithm for scattering by homogeneous bodies. *IEEE Trans. Antennas Propag.*, 46(11):1718–1726, 1998.
- [41] Kubilay Sertel and John L. Volakis. Multilevel fast multipole method solution of volume integral equations using parametric geometry modeling. *IEEE Transactions on Antennas and Propagation*, 52(7):1686–1692, 2004.
- [42] Cai Cheng Lu and Chun Yu. Simulation of radiation and scattering by large microstrip patch arrays on curved substrate by a fast algorithm. In *ICMMT 2002 - 2002 3rd Int. Conf. Microw. Millim. Wave Technol.*, pages 401–405. Institute of Electrical and Electronics Engineers Inc., 2002.
- [43] Özgür Ergül, Tahir Malas, and Levent Gürel. Analysis of dielectric photonic-crystal problems with MLFMA and Schur-complement preconditioners. *J. Light. Technol.*, 29(6):888–897, 2011.
- [44] Özgür Ergül. Solutions of large-scale electromagnetics problems involving dielectric objects with the parallel multilevel fast multipole algorithm. *J. Opt. Soc. Am. A*, 28(11):2261, nov 2011.

- [45] T. Sarkar, Ercument Arvas, and S. Rao. Application of FFT and the conjugate gradient method for the solution of electromagnetic radiation from electrically large and small conducting bodies. *IEEE Transactions on Antennas and Propagation*, 34(5):635–640, 1986.
- [46] M.F. Catedra, E. Gago, and L. Nuno. A numerical scheme to obtain the RCS of three-dimensional bodies of resonant size using the conjugate gradient method and the fast Fourier transform. *IEEE Trans. Antennas Propag.*, 37(5):528–537, 1989.
- [47] P. Zwamborn and P.M. van den Berg. The three dimensional weak form of the conjugate gradient FFT method for solving scattering problems. *IEEE Trans. Microw. Theory Tech.*, 40(9):1757–1766, 1992.
- [48] Seung M. Seo and Jin F. Lee. A fast IE-FFT algorithm for solving PEC scattering problems. In *IEEE Trans. Magn.*, volume 41, pages 1476–1479, may 2005.
- [49] Nilufer A. Ozdemir and Jin Fa Lee. IE-FFT algorithm for a nonconformal volume integral equation for electromagnetic scattering from dielectric objects. *IEEE Trans. Magn.*, 44(6):1398–1401, jun 2008.
- [50] Jiliang Yin, Jun Hu, Han Guo, and Zaiping Nie. Fast analysis of 3D inhomogeneous dielectric objects using IE-FFT. In *APMC 2009 - Asia Pacific Microw. Conf. 2009*, pages 84–87, 2009.
- [51] E. Bleszynski, M. Bleszynski, and T. Jaroszewicz. AIM: Adaptive integral method for solving large-scale electromagnetic scattering and radiation problems. *North*, 31(5):1225–1251, 1996.

- [52] Zhong Qing Zhang and Qing Huo Liu. A Volume Adaptive Integral Method (VAIM) for 3-D inhomogeneous objects. *IEEE Antennas Wirel. Propag. Lett.*, 1:102–105, 2002.
- [53] Jing-Li Guo, Jian-Ying Li, and Qi-Zhong Liu. Analysis of arbitrarily shaped dielectric radomes using adaptive integral method based on volume integral equation. *IEEE Trans. Antennas Propag.*, 54(7):1910–1916, jul 2006.
- [54] Joel R. Phillips and Jacob K. White. A Precorrected-FFT method for electrostatic analysis of complicated 3-d structures. *IEEE Trans. Comput. Des. Integr. Circuits Syst.*, 16(10):1059–1072, 1997.
- [55] L.-W Li, Y.-J Wang, and E.-P Li. MPI-BASED PARALLELIZED PRECORRECTED FFT ALGORITHM FOR ANALYZING SCATTERING BY ARBITRARILY SHAPED THREE-DIMENSIONAL OBJECTS. Technical report, 2003.
- [56] Xiao Chun Nie, Le Wei Li, Ning Yuan, Tat Soon Yeo, and Yeow Beng Gan. Precorrected-FFT solution of the volume integral equation for 3-D inhomogeneous dielectric objects. *IEEE Trans. Antennas Propag.*, 53(1 II):313–320, jan 2005.
- [57] Xiao Chun Nie, Ning Yuan, Le Wei Li, Yeow Beng Gan, and Tat Soon Yeo. A fast combined field volume integral equation solution to EM scattering by 3-D dielectric objects of arbitrary permittivity and permeability. *IEEE Trans. Antennas Propag.*, 54(3):961–969, mar 2006.

- [58] Jia Ye Xie, Hou Xing Zhou, Wei Hong, Wei Dong Li, and Guang Hua. A novel FG-FFT method for the EFIE. In *2012 Int. Conf. Comput. Probl. ICCP 2012*, pages 111–115, 2012.
- [59] Jia Ye Xie, Hou Xing Zhou, Wei Hong, Wei Dong Li, and Guang Hua. A highly accurate FGG-FG-FFT for the combined field integral equation. *IEEE Trans. Antennas Propag.*, 61(9):4641–4652, 2013.
- [60] Shu Wen Chen, Hou Xing Zhou, Wei Hong, and Jia Ye Xie. VIE-FG-FFT for analyzing em scattering from inhomogeneous nonmagnetic dielectric objects. *Int. J. Antennas Propag.*, 2014, 2014.
- [61] G. W. Hanson, A. I. Nosich, and E. M. Kartchevski. Green’s function expansions in dyadic root functions for shielded layered waveguides. *Progress In Electromagnetics Research*, 39:61–91, 2003.
- [62] Mohammad Kamandi, Reza Faraji-Dana, et al. Integral equation analysis of multilayered waveguide bends using complex images Green’s function technique. *Journal of Lightwave Technology*, 33(9):1774–1779, 2015.
- [63] Oscar P. Bruno, Emmanuel Garza, and Carlos Pérez-Arancibia. Windowed Green Function Method for Nonuniform Open-Waveguide Problems. *IEEE Transactions on Antennas and Propagation*, 65:4684–4692, 2017.
- [64] Ardavan F. Oskooi, Lei Zhang, Yehuda Avniel, and Steven G. Johnson. The failure of perfectly matched layers, and towards their redemption by adiabatic absorbers. *Optics Express*, 16(15):11376–11392, 2008.

- [65] J.-P. Bérenger. Evanescent waves in PML's: Origin of the numerical reflection in wave-structure interaction problems. *IEEE Transactions on Antennas and Propagation*, 47:1497 – 1503, 11 1999.
- [66] J.-P. Bérenger. An effective PML for the absorption of evanescent waves in waveguides. *IEEE Microwave and Guided Wave Letters*, 8:188 – 190, 06 1998.
- [67] J.-P. Bérenger. Application of the CFS PML to the absorption of evanescent waves in waveguides. *IEEE Microwave and Wireless Components Letters*, 12:218–220, 2002.
- [68] Erwin J. Alles and Koen W. A. van Dongen. Perfectly matched layers for frequency-domain integral equation acoustic scattering problems. *IEEE transactions on Ultrasonics, Ferroelectrics, and Frequency Control*, 58(5):1077–1086, 2011.
- [69] Lei Zhang, Jung Hoon Lee, Ardavan Oskooi, Amit Hochman, Jacob K White, and Steven G Johnson. A novel boundary element method using surface conductive absorbers for full-wave analysis of 3-d nanophotonics. *Journal of Lightwave Technology*, 29(7):949–959, 2011.
- [70] J. Aizpurua, P. Hanarp, D. S. Sutherland, M. Käll, Garnett W. Bryant, and F. J. García de Abajo. Optical Properties of Gold Nanorings. *Phys. Rev. Lett.*, 90(5):4, 2003.
- [71] F. J. García de Abajo and A. Howie. Retarded field calculation of electron energy loss in inhomogeneous dielectrics. *Phys. Rev. B - Condens. Matter Mater. Phys.*, 65(11):1154181–11541817, mar 2002.

- [72] Guy A E Vandenbosch, V. Volski, Francisco P G De Arquer, Niels Verellen, and Victor Moshchalkov. On the use of the method of moments in plasmonic applications. *Symp. Dig. - 20th URSI Int. Symp. Electromagn. Theory, EMTS 2010*, 46(November 2010):257–260, 2010.
- [73] Andreas M. Kern and Olivier J. F. Martin. Surface integral formulation for 3D simulations of plasmonic and high permittivity nanostructures. *J. Opt. Soc. Am. A*, 26(4):732, apr 2009.
- [74] M. G. Araújo, J. M. Taboada, D. M. Solís, J. Rivero, L. Landesa, and F. Obelleiro. Comparison of surface integral equation formulations for electromagnetic analysis of plasmonic nanoscatterers. *Opt. Express*, 20(8):9161, apr 2012.
- [75] M. Costabel, E. Darrigrand, and E. H. Kon. Volume and surface integral equations for electromagnetic scattering by a dielectric body. *J. Comput. Appl. Math.*, 234(6):1817–1825, 2010.
- [76] J. Markkanen, P. Yla-Oijala, and Seppo Jarvenpaa. Volume integral equation methods in computational electromagnetics. *Proc. 2013 Int. Conf. Electromagn. Adv. Appl. ICEAA 2013*, I:880–883, 2013.
- [77] Tapan K. Sarkar and Ercument Arvas. An Integral Equation Approach to the Analysis of Finite Microstrip Antennas: Volume/Surface Formulation. *IEEE Trans. Antennas Propag.*, 38(3):305–312, 1990.
- [78] C. C. Lu and W. C. Chew. A coupled surface-volume integral equation approach for the calculation of electromagnetic scattering from composite metallic and material targets. *IEEE Trans. Antennas Propag.*, 48(12):1866–1868, 2000.

- [79] Xiao-Chun Nie, Ning Yuan, L.-W. Li, Y.-B. Gan, and Tat Soon Yeo. A fast volume-surface integral equation solver for scattering from composite conducting-dielectric objects. *IEEE Trans. Antennas Propag.*, 53(2):818–824, feb 2005.
- [80] D. Schaubert, D. Wilton, and A. Glisson. A tetrahedral modeling method for electromagnetic scattering by arbitrarily shaped inhomogeneous dielectric bodies. *IEEE Trans. Antennas Propag.*, 32(1):77–85, 1984.
- [81] Peter Zwamborn and Peter M. van den Berg. The Three-Dimensional Weak Form of the Conjugate Gradient FFT Method for Solving Scattering Problems. *IEEE Trans. Microw. Theory Tech.*, 40:1757–1766, apr 1992.
- [82] Peter Zwamborn and Peter M. van den Berg. Computation of electromagnetic fields inside strongly inhomogeneous objects by the weak-conjugate-gradient fast-Fourier-transform method. *J. Opt. Soc. Am. A*, 11:1414–1421, apr 1994.
- [83] M. C. van Beurden and S. J. L. van Eijndhoven. Gaps in present discretization schemes for domain integral equations. In *2007 Int. Conf. Electromagn. Adv. Appl.*, pages 673–675. IEEE, sep 2007.
- [84] M. C. van Beurden and S. J. L. van Eijndhoven. Well-posedness of domain integral equations for a dielectric object in homogeneous background. *Journal of Engineering Mathematics*, 62(3):289–302, 2008.
- [85] Johannes Markkanen, Pasi Yla-Oijala, and Ari Sihvola. Discretization of volume integral equation formulations for extremely anisotropic materials. *IEEE Transactions on Antennas and Propagation*, 60(11):5195–5202, 2012.

- [86] P. De Doncker. A potential integral equations method for electromagnetic scattering by penetrable bodies. *IEEE Trans. Antennas Propag.*, 49(7):1037–1042, jul 2001.
- [87] Ruinan Chang and Vitaliy Lomakin. Potential-based volume integral equations. In *IEEE Antennas Propag. Soc. AP-S Int. Symp.*, pages 2712–2715, 2011.
- [88] Johannes Markkanen and Pasi Ylä-Oijala. Numerical comparison of spectral properties of volume-integral-equation formulations. *J. Quant. Spectrosc. Radiat. Transf.*, 178:269–275, 2016.
- [89] Johannes Markkanen. Volume potential-integral-equation formulation for electromagnetic scattering by dielectric objects. *2016 URSI Int. Symp. Electromagn. Theory, EMTS 2016*, (7):468–471, 2016.
- [90] Johannes Markkanen. Numerical Analysis of the Potential Formulation of the Volume Integral Equation for Electromagnetic Scattering. *Radio Sci.*, 52(10):1301–1311, oct 2017.
- [91] D.T. Borup and O.P. Gandhi. Fast-Fourier-Transform Method for Calculation of SAR Distributions in Finely Discretized Inhomogeneous Models of Biological Bodies. *IEEE Trans. Microw. Theory Tech.*, 32(4):355–360, apr 1984.
- [92] C.Y. Shen, K.J. Glover, M.I. Sancer, and A.D. Varvatsis. The discrete Fourier transform method of solving differential-integral equations in scattering theory. *IEEE Trans. Antennas Propag.*, 37(8):1032–1041, 1989.

- [93] H. Gan and W.C. Chew. A discrete bcg-fft algorithm for solving 3d inhomogeneous scatterer problems. *Journal of Electromagnetic Waves and Applications*, 9(10):1339–1357, 1995.
- [94] A. G. Polimeridis, J. F. Villena, L. Daniel, and J. K. White. Robust J-EFVIE solvers based on purely surface integrals. *2013 International Conference on Electromagnetics in Advanced Applications, ICEAA '13*, pages 379–381, 2013.
- [95] D. R. Wilton, S. M. Rao, A. W. Glisson, D. H. Schaubert, O. M. Al-Bundak, and C. M. Butler. Potential integrals for uniform and linear source distributions on polygonal and polyhedral domains. 32(3):276–281, March 1984.
- [96] P. Ylä-Oijala and M. Taskinen. Calculation of CFIE impedance matrix elements with RWG and $\hat{n} \times$ RWG functions. 51(8):1837–1846, August 2003.
- [97] S. Järvenpää and M. Taskinen and P. Ylä-Oijala. Singularity subtraction technique for high-order polynomial vector basis functions on planar triangles. 54(1):42–49, January 2006.
- [98] I. Hänninen and M. Taskinen and J. Sarvas. Singularity subtraction integral formulae for surface integral equations with RWG, rooftop and hybrid basis functions. *Prog. Electromagn. Res. PIER*, 63:243–278, 2006.
- [99] B. M. Notaroš. Higher order frequency-domain computational electromagnetics. 56(8):2251–2276, August 2008.
- [100] M. G. Duffy. Quadrature over a pyramid or cube of integrands with a singularity at a vertex. *SIAM. J. Numer. Anal.*, 19(6):1260–1262, 1982.
- [101] J. S. Asvestas, S. P. Yankovich, and O. E. Allen. Calculation of the impedance matrix inner integral to prescribed accuracy. 58(2):479–487, February 2010.

- [102] M.-D. Zhu, X.-L. Zhou, and W.-Y. Yin. Radial integration scheme for handling weakly singular and near singular potential integrals. 10:792–795, 2011.
- [103] F. Vipiana and D. R. Wilton. Numerical evaluation via singularity cancellation schemes of near-singular integrals involving the gradient of Helmholtz-type potentials. 61(3):1255–1265, March 2013.
- [104] M. M. Botha. A family of augmented Duffy transformations for near-singularity cancellation quadrature. 61(6):3123–3134, June 2013.
- [105] D. J. Taylor. Accurate and efficient numerical integration of weakly singular integrals in Galerkin EFIE solutions. 51(7):1630–1637, July 2003.
- [106] A. G. Polimeridis and T. V. Yioultis. On the direct evaluation of weakly singular integrals in Galerkin mixed potential integral equation formulations. 56(9):3011–3019, September 2008.
- [107] A. G. Polimeridis and J. R. Mosig. Complete semi-analytical treatment of weakly singular integrals on planar triangles via the direct evaluation method. *Int. J. Numerical Methods Eng.*, 83:1625–1650, 2010.
- [108] A. G. Polimeridis, J. M. Tamayo, J. M. Rius, and J. R. Mosig. Fast and accurate computation of hyper-singular integrals in Galerkin surface integral equation formulations via the direct evaluation. 59(6):2329–2340, June 2011.
- [109] A. G. Polimeridis and J. R. Mosig. On the direct evaluation of surface integral equation impedance matrix elements involving point singularities. 10:599–602, 2011.
- [110] DEMCEM package, 2011.

- [111] M. T. H. Reid, J. K. White, and S. G. Johnson. Generalized Taylor-Duffy method for efficient evaluation of Galerkin integrals in boundary- element method computations. 63(1):195–209, January 2015.
- [112] D. R. Wilton, F. Vipiana, and W. A. Johnson. Evaluation of 4-D Reaction Integrals in the Method of Moments: Coplanar Element Case. *IEEE Transactions on Antennas and Propagation*, 2017.
- [113] S. M. Rao, D. R. Wilton, and A. W. Glisson. Electromagnetic scattering by surfaces of arbitrary shape. 30(3):409–418, May 1982.
- [114] B. M. Kolundzija and A. R. Djordjevic. *Electromagnetic modeling of composite metallic and dielectric structures*. Boston, MA: Artech House, 2002.
- [115] B. M. Kolundzija and A. R. Djordjevic. Analysis of dipole antenna with corner reflector. In *Proc. 7th Colloquium on Microwave Communication*, pages 319–322, Budapest, Hungary, 1982.
- [116] M. D. Deshpande. Electromagnetic scattering from a polygonal thin metallic plate using quadrilateral meshing. *NASA/TM-2003-212165*.
- [117] M. Djordjević and B. M. Notaroš. Double higher order method of moments for surface integral equation modeling of metallic and dielectric antennas and scatterers. 52(8):2118–2129, August 2004.
- [118] B. M. Kolundzija and A. R. Djordjevic. *WIPL-D: Electromagnetic Modeling of Composite Metallic and Dielectric Structures. Software and User’s Manual*. Boston, MA: Artech House, 2000.

- [119] E. Jørgensen, J. L. Volakis, P. Meincke, and O. Breinbjerg. Higher order hierarchical Legendre basis functions for electromagnetic modeling. 52(11):2985–2995, November 2004.
- [120] W. Ding and G. Wang. Treatment of singular integrals on generalized curvilinear parametric quadrilaterals in higher order method of moments. 8:1310–1313, 2009.
- [121] H. Yuan, N. Wang, and C. Liang. Combining the higher order method of moments with geometric modeling by NURBS surfaces. 57(11):3558–3563, November 2009.
- [122] A. Manić, M. Djordjević, and B. M. Notaroš. Duffy method for evaluation of weakly singular SIE potential integrals over curved quadrilaterals with higher order basis functions. 62(6):3338–3343, 2014.
- [123] A. G. Polimeridis, F. Vipiana, J. R. Mosig, and D. R. Wilton. DIRECTFN: Fully numerical algorithms for high precision computation of singular integrals in Galerkin SIE methods. 61(6):3112–3122, June 2013.
- [124] L. Knockaert. On the analytic calculation of multiple integrals in electromagnetics. *2011 International Conference on Electromagnetics in Advanced Applications, ICEAA '11*, pages 595–598, 2011.
- [125] DIRECTFN package. <https://github.com/thanospol/DIRECTFN>, 2017.
- [126] Jianming Jin. *The Finite Element Method in Electromagnetics*. Wiley-IEEE Press, 3rd edition, 2014.
- [127] Gene H. Golub and Charles F. Van Loan. *Matrix Computations (3rd Ed.)*. Johns Hopkins University Press, Baltimore, MD, USA, 1996.

- [128] Matteo Frigo and Steven G. Johnson. The design and implementation of FFTW3. *Proceedings of the IEEE*, 93(2):216–231, 2005.
- [129] Samuel P. Groth, Athanasios G. Polimeridis, Alexandra Tambova, and Jacob K. White. Circulant preconditioning in the volume integral equation method for silicon photonics. *J. Opt. Soc. Am. A*, 36(6):1079, jun 2019.
- [130] Tony F. Chan and Julia A. Olkin. Circulant preconditioners for Toeplitz-block matrices. *Numerical Algorithms*, 6(1):89–101, 1994.
- [131] H. C. van de (Hendrik Christoffel) Hulst. *Light scattering by small particles*. Dover Publications, 1981.
- [132] M. Kerker. *The Scattering of Light and Other Electromagnetic Radiation*. Elsevier, 1969.
- [133] Craig F. Bohren and Donald R. Huffman. *Absorption and Scattering of Light by Small Particles*. Wiley, apr 1998.
- [134] Roger F. Harrington. *Time-harmonic electromagnetic fields*. IEEE Press, 2001.
- [135] A. Farjadpour, David Roundy, Alejandro Rodriguez, M. Ibanescu, Peter Bermel, J. D. Joannopoulos, Steven G. Johnson, and G. W. Burr. Improving accuracy by subpixel smoothing in the finite-difference time domain. Technical Report 20, 2006.
- [136] Steven G. Johnson, Peter Bienstman, M. A. Skorobogatiy, Mihai Ibanescu, Eleftherios Lidorikis, and J. D. Joannopoulos. Adiabatic theorem and continuous coupled-mode theory for efficient taper transitions in photonic crystals. *Physical Review E*, 66(6):066608, 2002.

- [137] M. L. Povinelli, Steven G. Johnson, and J. D. Joannopoulos. Slow-light, band-edge waveguides for tunable time delays. *Optical Society of America*, 13(18):7145–7159, 2005.
- [138] Kurt E. Oughstun and Natalie A. Cartwright. On the Lorentz-Lorenz formula and the Lorentz model of dielectric dispersion. *Optics Express*, 11(13):1541–1546, 2003.
- [139] COMSOL Multiphysics[®] . <https://www.comsol.com>.
- [140] E. Erez and Y. Leviatan. Electromagnetic scattering analysis using a model of dipoles located in complex space. *IEEE Transactions on Antennas and Propagation*, 42(12):1620–1624, 1994.
- [141] Lei Zhang. *A boundary element method with surface conductive absorbers for 3-D Analysis of nanophotonics*. Ph. d dissertation, Massachusetts Institute of Technology, 2010.
- [142] Benjamin Gallinet, Jérémy Butet, and Olivier J.F. F. Martin. Numerical methods for nanophotonics: standard problems and future challenges. *Laser Photon. Rev.*, 9(6):577–603, nov 2015.
- [143] W. C. Chew. *Waves and Fields in Inhomogeneous Media*. New York: Van Nostrand, 1990.
- [144] Nguyen Dinh-Liem. A volume integral equation method for periodic scattering problems for anisotropic Maxwell’s equations. *Appl. Numer. Math.*, 98:59–78, 2015.

- [145] Yi Zhang, Shuyu Yang, Andy Eu-Jin Lim, Guo-Qiang Lo, Christophe Galland, Tom Baehr-Jones, and Michael Hochberg. A compact and low loss Y-junction for submicron silicon waveguide. *Optics Express*, 21(1):1310–1316, 2013.
- [146] J. David Jackson. *Electrodynamics*. Wiley Online Library, 1975.
- [147] Xianjin Li, Lin Lei, Yongpin Chen, Ming Jiang, and Jun Hu. A Domain Decomposition Method Based on Volume-Surface Integral Equation for complex Dielectric/Metallic Composite Objects. *2018 12th Int. Symp. Antennas, Propag. EM Theory, ISAPE 2018 - Proc.*, c:1–3, 2019.
- [148] Darko Zibar. Machine learning in photonics: From components to system optimization. In *Opt. InfoBase Conf. Pap.* OSA - The Optical Society, jul 2014.
- [149] Daniele Melati, Mohsen Kamandar Dezfouli, Yuri Grinberg, Siegfried Janz, Jens H. Schmid, Pavel Cheben, and Dan-Xia Xu. Machine learning design of subwavelength integrated photonic devices. pages 135–136. Institute of Electrical and Electronics Engineers (IEEE), aug 2019.